Digital Microfluidic Systems for Self-cleaning Surfaces and Lab-on-Chip Devices Using Anisotropic Ratchet Conveyors

Di Sun

A dissertation

submitted in partial fulfillment of the

requirements for the degree of

Doctor of Philosophy

University of Washington

2020

Reading Committee:

Karl F. Böhringer, Chair

Lih Y. Lin

Alexander V. Mamishev

Program Authorized to Offer Degree:

Electrical and Computer Engineering

University of Washington

Abstract

Digital Microfluidic Systems for Self-cleaning Surfaces and Lab-on-Chip Devices Using Anisotropic Ratchet Conveyors

Di Sun

Chair of the Supervisory Committee:
Karl F. Böhringer
Department of Electrical and Computer Engineering

This work focuses on creating active self-cleaning surface systems and lab-on-chip devices using anisotropic ratchet conveyors (ARCs). ARCs create micro-sized hydrophilic patterns on a hydrophobic background. Two different ARC systems were designed and fabricated with self-assembled monolayers (SAMs) and hydrophobic Cytop thin films. A Parylene C stencil mask process was developed to create patterns on the Cytop thin films without degrading the Cytop original hydrophobicity. Optical transmission measurements showed Cytop could improve glass substrate optical transmittance by 2.5~3.5% over the entire visible wavelength range. We first developed an active self-cleaning surface system using orthogonal vibration to drive the water droplet transport along the solar module surface with the assistance of ARC. Real-time demonstrations of droplet transport and surface cleaning were performed, in which the solar

modules achieved a 23 percentage-point gain after cleaning. We then developed a platform using electrowetting-on-dielectric (EWOD) and liquid dielectrophoresis (L-DEP) with the assistance of ARCs. Droplet transport on an inclined surface to remove the surface contaminants and fog were demonstrated. In the end, we combined ARCs with surface an acoustic wave nebulization (SAWN) platform to create an integrated lab-on-chip device. The SAWN-ARC device integrated droplet delivery, merging, mixing, and nebulization functionalities. Mass spectrometry (MS) measurements with the SAWN chip were performed under different input frequencies. The SAWN transducer provided a controllable nebulization rate by varying the input nebulization frequency while maintaining a reasonable signal to noise ratio for MS detection.

TABLE OF CONTENTS

LIST OF FIGURES

LIST OF TABLES

ACKNOWLEDGEMENTS

My deep gratitude goes first to my committee chair, Professor Karl F. Böhringer, for his guidance throughout my six-year graduate education. It was an enjoyable journey to work with him and share the excitement of the discovery of both life and science. My future career will benefit from his unwavering support and encouragement. I would like to express my heartful thanks to my Ph.D. thesis committee members, Professor Lih Y. Lin, Professor Alexander V. Mamishev, and Professor J. Devin MacKenzie, for their encouragement, insightful questions, and suggestions on my research. I express my sincere thanks to all the current and former staff at Washington Nanofabrication Facility (WNF) for the training of my experimental skills in the cleanroom, including Dr. Darick Baker, Dr. Andy Lingley, Duane Irish, Dr. Mark Morgan, Dr. Fred Newman, Mark Brunson, David Nguyen, Shane Patrick, and Sarice Jones. I acknowledge the training and technical support from Dr. Felippe J Pavinatto and Philip Cox at the Clean Energy Institute Testbeds. I acknowledge the financial support given by the Department of Electrical and Computer Engineering, CoMotion, Clean Energy Institute (CEI) at the University of Washington, Amazon Catalyst Fund, and I-Corps Fund from the National Science Foundation (NSF).

I thank all my lab mates, Hal Holmes, Zheyi Han, Nerea Alayo, Ana Gomez, Gerardo Gomez, Xiange Wang, Yifei Song, and Yuchen Shi for their support and discussions. I thank my collaborators Matthew Sorensen, Erik Nilsson from Deurion, LLC, and Professor David Goodlett from the University of Maryland. I would like to thank all my friends, Yanglin Lin, Yu Jin, Maolong Tang, Shifeng Zhu, Jenni Wan, Chen Zou, Jingda Wu, Peifeng Jin, Ethan Keeler, Bowen

Xue, Vince Wu, Bin Yu, Qian Wang, Jun Yao, Pan Li, Zheng Li, Relong Zheng, and Jiayang He. My warm thanks to my girlfriend Xinying Zeng for her companionship, encouragement, and support during the process.

DEDICATION

I am dedicating this thesis to my parents Weiguo Sun and Yunyan Liu for their support.

Chapter 1. INTRODUCTION

1.1 MOTIVATION

A self-cleaning surface is defined as a surface that prevents or reduces surface contamination such as dust, water condensation, stains, or organic matter [1, 2]. Self-cleaning surfaces have been under development at least since the late 20th century. Related research involves multi-disciplinary backgrounds and aims at a broad range of applications including skyscraper windows, car windshields, solar panel cover glass, surveillance camera lenses, and water drag reduction on ship hulls [3]. Scientists have been inspired by nature to modify the microscopic structural and chemical properties of surfaces based on discoveries from plants, insects, and reptiles [4-7]. The approach is termed "biomimetics" as it mimics the micro/nano structures on plant leaves, insect wings, and animal skins.

Self-cleaning surfaces in nature rely often on water droplets (rain or condensation) and gravity to wash away surface contaminants. Such surfaces require to be positioned at a tilted angle, and the path that the droplet follows during cleaning is not precisely defined. Considering these drawbacks, more systematic designs have been proposed employing micro-electro-mechanical systems (MEMS) and microfluidics approaches, in combination with surface modifications for better cleaning effects. Many innovative designs have been implemented aiming at reducing labor and the overall maintenance cost for clean surfaces.

In this thesis, we first exploit the working principles of different self-cleaning surfaces and systems, including both passive surface structure design and active microsystems. The design strategies and fabrication processes are introduced, as well as application examples. To research the possibility of creating self-cleaning surfaces using single water droplets, we develop a

micropatterned heterogeneous surface which can directionally transport the droplet under orthogonal vibrations. The micropatterns are fabricated by creating hydrophilic curved rungs on a hydrophobic background, termed as anisotropic ratchet conveyors (ARCs). An active self-cleaning surface system is developed using an ARC to systematically guide the droplet movement and the footprint of the droplet can cover the whole surface area to pick up all the surface contaminants under mechanical vibrations. Furthermore, we combine the ARC with an electrowetting-on-dielectric (EWOD) system, liquid dielectrophoresis (L-DEP) and an surface acoustic wave (SAW) system for fog removal and lab-on-chip applications.

1.2 PASSIVE SELF-CLEANING SURFACES STRATEGY

Passive self-cleaning surfaces rely on surface modifications, combining both physical and chemical changes of their surface properties. The surface energy will be altered accordingly to reduce the adhesion of a water droplet to the surface. The droplet can slide off or roll off the surface under gravity when tilted to clean the contaminants along its path. No other external physical fields are involved in dislodging the contaminants [8]. In this section, we will discuss the fundamental surface wettability theory and different surface modification approaches, including superhydrophobic surfaces, superomniphobic surfaces, superhydrophilic surfaces, and liquid infused porous surfaces.

1.2.1 *Surface Wettability Theory Review*

Molecules inside a bulk liquid have interactions with each other. When a liquid is placed in contact with other subjects like immersible liquid, gas or solid, at the boundaries or interfaces between the fluid and other subjects, the fluid molecules experience localized molecular interaction dissymmetry. Surface tension has been introduced to describe such an energy imbalance at the

interface, with a unit of N/m or J/m^2. As the liquid is placed on the solid surface, the liquid will spread if the system total energy is lowered by the presence of the liquid. The liquid will form a "droplet" on the surface. To describe the wettability properties of a surface, the static and dynamic contact angles of a sessile droplet are commonly characterized. As depicted in Fig. 1.1 (a), the static contact angle (CA), θ, is determined by the tangent angle between the smooth solid surface and the liquid meniscus outline [9]. The basic law for surface wettability was first derived by Thomas Young in 1805, known as Young's equation [10]:

$$\cos\theta = \frac{\gamma_{SG} - \gamma_{SL}}{\gamma_{LG}} \tag{1-1}$$

where γ_{SG}, $\gamma_{SL,}$ and γ_{LG} are, respectively, the interfacial surface tension at the solid/gas, solid/liquid, and liquid/gas interfaces. The model is based on the thermodynamic equilibrium approach between the three phases. Surface wettability is described as hydrophobic (CA > 90°) when the solid surface free energy in air is lower than in liquid, and hydrophilic (CA < 90°) when the solid surface free energy in air is higher than with liquid on top [9, 11, 12]. The suffix of "-philic" or "-phobic" describes whether the liquid has an affinity or lacks an affinity to the solid. A variety of contact angle measurement methods have been proposed, including direct measurement by goniometer [13], captive bubble method [14], Wilhelmy method [15], capillary tube [16], and capillary bridge [17-19], among others. These approaches rely on Young's equation and the interfacial surface tension remains unchanged during the measurement. The goniometer is the most widely used tool to measure a static contact angle. The profile of a sessile droplet silhouette is captured, and the droplet contact angle is determined by aligning the tangent of the droplet profile at the liquid/solid contact point. To analyze the droplet contact angle, we cannot cover all the methods but briefly introduce axisymmetric drop shape analysis (ADSA) [20-24], theoretical image fitting analysis (TIFA) [25], and high-precision droplet shape analysis (HPDSA) [26, 27]. ADSA was first

developed by Y. Rotenberg, *et al*. to minimize the squares of normal distances between the droplet side view profile and theoretical capillary curve based on the Laplacian equation [20]. The surface tension is an adjustable parameter and droplet profile coordinates are determined by edge detection techniques. Instead of knowing the coordinates along with the droplet profile, F. K. Skinner, *et al*. modified the ADSA by measuring the droplet diameter from the top view [24]. The modified approach can measure low contact angles (CA<30°). ADSA uses a one-dimensional profile curve and requires edge detection. The TIFA method determines the droplet surface tension by 2-dimensional fitting between the pendant droplet image and the theoretically calculated profile without the need for edge detection. M. Schmitt and F. Heib developed the HPDSA method to analyze droplets on inclined surfaces [26, 27], using localized ellipse fitting to determine the contact angles separately for non-axisymmetric drop shapes. Sequential images of dynamic droplet contact angle change can be extracted by this method.

As the droplet dynamically wets or dewets the surface, the liquid-air-solid three phase contact line (TPL) starts to advance or recede. More than one state can exist. The interfacial energies at the TPL will have multiple energy equilibrium states [28] caused by surface imperfections such as local defects or roughness. Macroscopically, we can monitor a minimum CA value, called receding angle, θ_{rec}, as the TPL recedes and a maximum CA value, called advancing angle, θ_{adv}, as the TPL advances. The difference between the advancing and receding angle is called contact angle hysteresis (CAH, $\theta_{CAH} = \theta_{adv} - \theta_{rec}$), shown in Fig. 1.1 (b) and (c). Due to contact angle hysteresis, a droplet can be pinned on inclined surfaces, as shown in Fig. 1.1 (d). Sliding angle (SA), α, is defined as the angle between the tilted substrate and the horizontal plane when a sessile droplet starts to move down the surface due to gravity [29]. The relationship describing the sliding angle on a smooth surface with contact angle hysteresis can be described as [30]:

$$mg \sin \alpha / d = \gamma_{LG} (\cos \theta_{rec} - \cos \theta_{adv}) \quad (1\text{-}2)$$

where *m* is the droplet mass, *g* is the gravity constant, and *d* is the droplet diameter in contact with the surface.

Large contact angle hysteresis implies strong pinning or stiction of the liquid to the surface [31]. Consequently, K.Y. Law proposed a definition of surface hydrophobicity based on the receding CA θ_{rec} instead of the static CA θ [11]. A more distinct difference between the measured wetting force and θ_{rec} could be observed when $\theta_{rec} > 90°$ or $\theta_{rec} < 90°$. Based on the surface affinity measurements, the author proposed that the surface was hydrophilic when $\theta_{rec} < 90°$ and the surface was hydrophobic when $\theta_{rec} > 90°$.

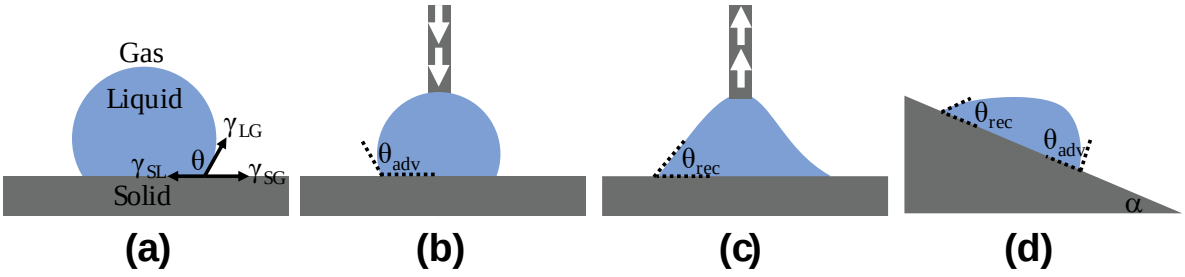

Figure 1.1. Schematics of contact angle types. The grey region represents the solid surface and the blue color represents the liquid on top. (a) Static contact angle θ and interfacial surface tension γ according to Young's equation. (b) and (c) represent a method to measure the advancing and receding contact angle. The arrow represents the direction of external pressure to dispense water onto or retrieve water from the solid surface through a dispensing needle. (d) Inclination angle α, advancing angle θ_{adv}, and receding angle θ_{rec}.

1.2.2 *Capillary Length*

The liquid surface meniscus caused by the internal liquid molecular interactions leads to pressure imbalance between the internal of the fluid and the external environment. The pressure induced by surface tension is referred as Laplace pressure. The liquid droplets also experience gravity force

as the body forces. When the droplet becomes large enough, the droplet will lose the spherical shape due to the influence of gravity forces. The critical length-scale, when the surface tension force and body gravity have an equal influence on the droplet, is called capillary length (L). As shown in Fig. 1.2, the pressure difference between the inside and outside of the droplet can be expressed as [32]:

$$\Delta P = P_{in} - P_{out} = 2\frac{\gamma}{R} \tag{1-3}$$

where ΔP is the Laplace pressure, P_{in} is the pressure inside the droplet, P_{out} is the pressure outside the droplet, γ is the surface tension, and r is the radius of the spherical droplet.

With equation (3), we can derive the pressure difference at point A (topmost point) and point B (bottommost point) as:

$$\Delta P_{BA} = P_{in,B} - P_{in,A} = 2\frac{\gamma}{R_B} - 2\frac{\gamma}{R_A} \tag{1-4}$$

The pressure difference ΔP_{BA} can also be calculated with the hydrostatic equation:

$$\Delta P_{BA} = \rho g h \tag{1-5}$$

where h is the length of the droplet. Combining equation (1-4) and equation (1-5), we have:

$$\frac{1}{R_B} - \frac{1}{R_A} = \left(\frac{\frac{h}{2}}{\frac{\gamma}{\rho g}}\right) = \left(\frac{\frac{h}{2}}{L^2}\right) \tag{1-6}$$

The expression of the capillary length is $L = \sqrt{\frac{\gamma}{\rho g}}$. When the droplet is small, $\frac{1}{R_B} - \frac{1}{R_A} \approx 0$, meaning the droplet is close to spherical shape with $R_A \approx R_B$. When the droplet is large, then $\frac{1}{R_B} - \frac{1}{R_A} > 0$, meaning the droplet is like a "puddle" shape with a flat cap with $R_A > R_B$.

For the water at room temperature, $\gamma = 72.8$ Nm^{-1} and density $\rho = 998$ kgm^{-3}. We can estimate the capillary length L at 2.71 mm.

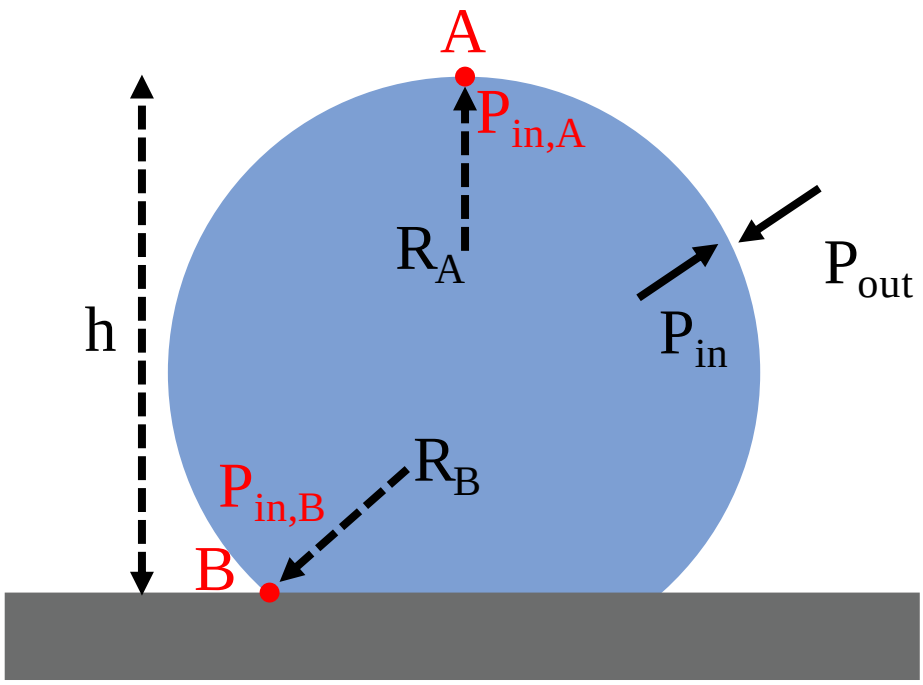

Figure 1.2. Schematics of capillary length derivation.

1.2.3 *Influence of Surface Roughness*

Young's equation does not consider the influence of surface roughness. Wenzel (1936) [33] and Cassie-Baxter (1944) [34] proposed models to study the water droplet apparent CA on a rough surface. For homogeneous wetting conditions, the CA can be estimated using the Wenzel model as in (Fig. 1.3 (a)):

$$\cos \theta^* = r \cos \theta \tag{1-7}$$

where θ^* is the apparent CA on a rough surface, r is the surface roughness defined as the ratio of total rough surface area over the projected flat region (always ≥ 1), and θ is the Young (intrinsic) CA as defined on a flat surface. The Wenzel equation shows that surface roughness amplifies the wetting on originally flat surfaces [35]. On hydrophilic rough surfaces, the apparent CA θ^* becomes smaller than the intrinsic CA θ, while on hydrophobic rough surfaces, the apparent CA θ^* becomes larger as compared to the intrinsic CA on flat surfaces.

However, on rough hydrophobic surfaces, the surface energy of a dry solid surface is lower compared to a wet liquid/solid interface. Instead of wetting all solid surface asperities, the water droplet often forms composite interfaces with air pockets and solid surfaces underneath [35, 36]. A model that captures this more complex heterogeneous scenario was proposed by Cassie and Baxter to predict water droplet contact angle on composite surfaces (in particular, solid and air, see Fig. 1.3 (b)):

$$\cos\theta^* = \phi_{air}\cos\theta_{air} + \phi_{solid}\cos\theta_{solid} \tag{1-8}$$

where ϕ_{air} and ϕ_{solid} are area fractions of the air and solid surface and $\phi_{air} + \phi_{solid} = 1$. θ_{air} and θ_{solid} are water CAs when in contact with air or a solid surface. From Young's equation it follows that the contact angle of water with air is 180°, thus $\cos\theta_{air} = -1$, and we can derive the relationship between the apparent CA θ^* and the Young CA $\theta = \theta_{solid}$ on the composite surface as:

$$\cos\theta^* = -1 + \phi_{solid}(1 + \cos\theta) \tag{1-9}$$

In this case, the solid surface region fraction ϕ_{solid} represents the portion of the heterogeneous surface in contact with liquid, as opposed to the surface roughness *r*, which is the key parameter to determine the contact angle on homogeneously wetted rough surfaces.

By studying CAs or CAHs on chemically heterogeneous surfaces, the Wenzel and Cassie-Baxter model is accurate only along the contact TPL instead of the whole contact region between droplet and surface. Experiments on chemically heterogeneous surfaces were performed by C.W. Extrand [37] and L. Gao and T. MacCathy [38]. In Gao and MacCathy's experiments, a circular spot with a different surface finish was patterned on the substrate, *e.g.* a hydrophilic spot on a hydrophobic field, or a flat hydrophobic spot on a rough field. By continuously expanding or retrieving the droplet, the advancing CA, receding CA, and the CAH were all determined by the surface condition on the homogeneous periphery at the TPL instead of the average surface

conditions beneath the droplet away from the TPL.

On a flat surface with the known lowest surface energy coatings based on the hexagonal close alignment of $-CF_3$ groups, the highest contact angle of a sessile water droplet can only be approximately 120° [12]. With surface roughness, according to the Cassie-Baxter model, when ϕ_{solid} is close to zero, the apparent contact angle θ^* approaches 180°. However, as shown in Fig. 1.3 (c), the water can impregnate into the surface roughness structures. Studied by Miwa, *et al.* [39], the Cassie-Baxter equation may be modified as:

$$\cos \theta^* = -1 + \phi_{solid} (1 + r \cos \theta) \qquad (1\text{-}10)$$

where r is the analogous surface roughness term as in Wenzel's equation and $r\,\phi_{solid}$ represents the ratio of the substrate-water contact area to the projected surface area. The interaction energy between the liquid and solid is $r\,\phi_{solid}$ times higher when compared to a flat surface. A low SA (~ 1°) is achieved only with a high trapped air ratio and reduced r, meaning the droplet needs to rest at the tip of the roughness structures with small impregnation regions into the roughness, close to perfect Cassie-Baxter state. The water impregnation level was further studied with atomic force microscopy (AFM) on hierarchical structures together with Miwa's model by N. Okulova, *et al.* [40]. Because of the water impregnation, a strong liquid-solid surface adhesion can coexist with a high contact angle of the droplet on the surface, named "rose petal effect" [41]. The surface roughness, in this case, will increase the CA hysteresis [28]. The water droplet keeps a high CA (153°) but meanwhile exhibits a high CA hysteresis by pinning to the substrate even when the substrate is placed vertically or upside down.

Water droplets on top of surfaces with a high CA (>150°), low SA (<10°), and low CAH (<10°) are most favorable for self-cleaning. This property is termed superhydrophobicity [42, 43]. On superhydrophobic surfaces, a water droplet can roll off the surface by gravity easily when the

surface is slightly titled and pick up dust particles along its path. The adhesion force of dust to the superhydrophobic substrate is several times lower than on hydrophilic or even hydrophobic surfaces [44]. We term such a cleaning strategy as passive [45] and the cleaning process will happen only when the water droplet is dispensed on tilted surfaces.

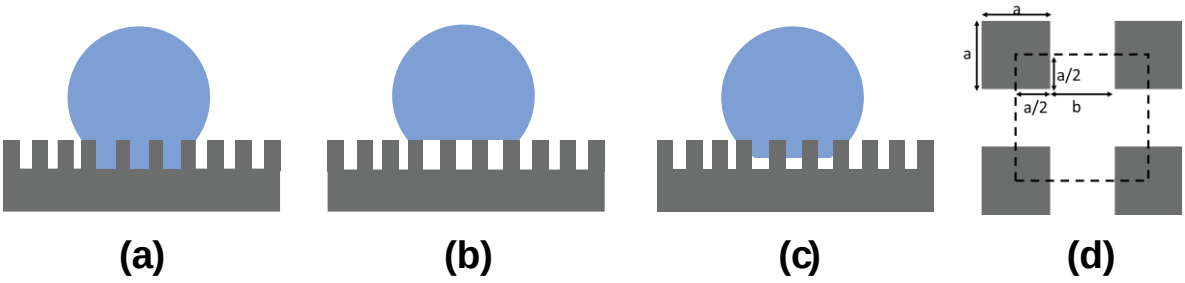

Figure 1.3. Schematics of different wetting states. (a) Wenzel state. (b) Cassie-Baxter state. (c) The transitional state between the Wenzel and Cassie-Baxter state, including the "petal effect" with simultaneously high CA and high SA. (d) Top view of a typical artificial superhydrophobic surface design by creating surface roughness with pillars. The pillar height is *h*, the pillar breadth and width are *a* and the distance between adjacent pillar edges is *b*. The dotted square shows a periodic structure for calculation with a quarter of pillar surface counted at each corner.

1.2.4 *Superhydrophobic Surfaces*

Two botanists, Barthlott and Neihuis [46], studied the microrelief of plant surfaces and discovered the papillose epidermal surface roughness and epicuticle wax coatings were the two key factors for self-cleaning mechanisms. Water droplets on top of the lotus leave kept high contact angles (~160°) and low sliding angles (<5°), promoting the motion of the water droplets under gravity when the surface was tilted. Due to the surface roughness, dust particles on top of the leaves had reduced contact regions to the surface, which decreased the adhesion forces and were much easier to be cleaned away. Many review articles have been published related to superhydrophobic surface fabrication processes and applications [3, 47-49]. In this section, we have a concise discussion of

the superhydrophobic surface design parameters and artificial superhydrophobic surface examples.

Inspired by the lotus leaf in nature, scientists have explored ways to mimic the lotus effect by designing micro-sized surface roughness and low surface energy coatings. Fig. 1.3 (d) shows the top view of a typical artificial superhydrophobic surface with square pillars. The Wenzel equation and the Cassie-Baxter equation now become [50, 51]:

$$\cos\theta_w^* = \left(1 + \frac{4\phi_{solid}}{(a/h)}\right)\cos\theta \tag{1-11}$$

$$\cos\theta_c^* = -1 + \phi_{solid}\,(1 + \cos\theta) \tag{1-12}$$

$$\phi_{solid} = \frac{1}{(b/a+1)^2} \tag{1-13}$$

From the equations, the Wenzel state is dependent on the pillar height while the Cassie-Baxter state is not. In both states, the droplet is in a stable thermodynamic equilibrium. An energy barrier exists to prevent the transition between these two states. To be in Wenzel or Cassie-Baxter state is determined by how the droplet is formed. By calculating the energy of a drop of given volume in equilibrium on a substrate, a small a/h value (slender pillars) is suggested to obtain a robust state. A periodical (b/a) is recommended to make the droplet insensitive to energy state change. A two-tier surface roughness design with both microscale and nanoscale roughness is recommended, which provides a more stable superhydrophobic state and lower contact angle hysteresis [52].

Fig. 1.4 presents some examples. R. Furstner, *et al.* came up with strategies to create multiple types of superhydrophobic surfaces [53]. Shown in Fig. 1.4 (a)-(c), silicon micro-sized pillars fabricated with X-ray lithography and followed by reactive ion etching processes, microstructured copper foil surfaces, and a replica of lotus leaves using silicone molding were fabricated and characterized. All the surface designs had superhydrophobic properties. For instance, on a replica of plant surfaces, water droplets kept a high contact angle (>150°) and a low sliding angle (~7°). Cleaning efficiency was defined by checking the number of SEM images without contamination

particles after surface cleaning with water droplets divided by the total number of SEM images taken. 90-95% of cleaning efficiency could be achieved.

K. Koch, *et al.* created two-tier hierarchical structures of roughness by depositing lotus wax tubules on top of Si or lotus leaf replicas (Fig. 1.4 (d)) [54], achieving larger water droplet contact angle (~170°) and smaller sliding angle (1-2°) compared with one-tier roughness structures like Si micropillars.

Fig. 1.4 (e) shows a nano-cone structure on a flexible Teflon substrate by oxygen plasma etching of a colloidal monolayer of polystyrene beads [55]. The wettability of the surface was controlled geometrically based on plasma treatment time as well as chemically by further gold nanoparticle deposition and silanization.

Fig. 1.4 (f) shows a low-cost porous structure of isostatic polypropylene (i-PP) [56]. i-PP was dissolved in the solvent mixture consisting of methyl ethyl ketone (MEK), cyclohexanone, and isopropyl alcohol, and dropped on a glass substrate. The solvent was further dried in a vacuum oven. The remaining i-PP formed a porous "bird's nest" morphology. From atomic force measurements, the roughness of pure thin i-PP film was 10 nm RMS with a water contact angle of 104°, while the porous coating had 300 nm RMS and improved water droplet contact angle from 104° to 149°.

K. Lau, *et al.* [57] developed superhydrophobic surfaces by growing vertical carbon nanotube forests with a PECVD process, shown in Fig. 1.4 (g). To provide a stable high water droplet contact angle, the carbon nanotubes were coated with thin conformal hydrophobic poly(tetrafluoroethylene) (PTFE) by a hot filament chemical vapor deposition (HFCVD) process. Most of the superhydrophobic surfaces were made of fragile microstructures or polymeric materials, where durability could be an issue for field applications because of the harsh

environment.

Y. Lu, *et al.* created a mechanically strong coating using an ethanolic suspension of perfluoro silane-coated titanium dioxide nanoparticles (shown in Fig. 1.4 (h)) [58]. Two dimensions of TiO_2 nanoparticles (200 nm diameter and 20 nm diameter) were mixed and suspended in the ethanolic solution. The coating was able to be applied to various types of substrates like clothes, paper, or steel by spray, dip, or extrusion coating processes and kept superior high water repellency after 40 cycles of sandpaper abrasion. The robustness of coating processes, substrate choice, and high mechanical strength allowed the paint to have potential applications in harsh environments.

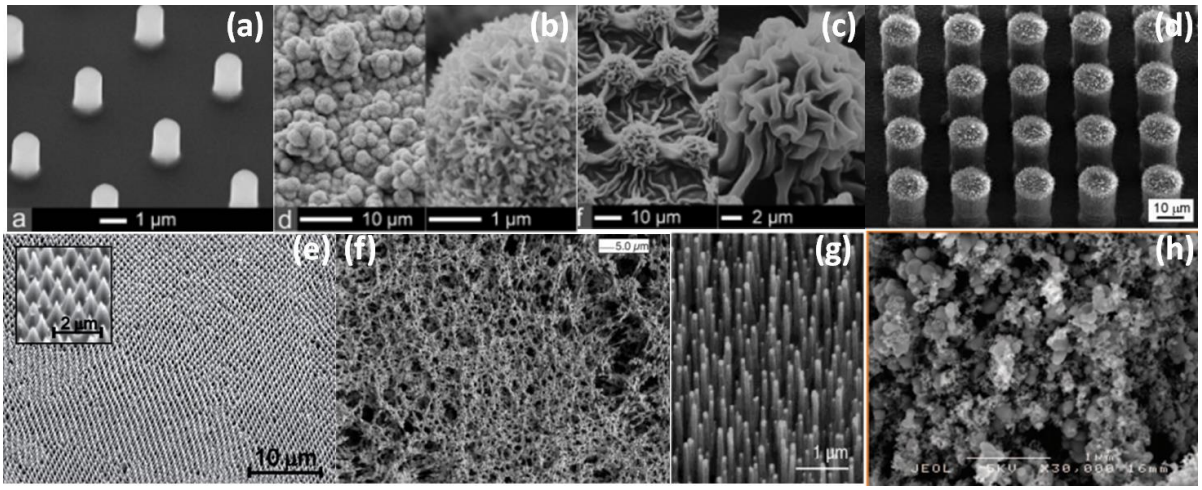

Figure 1.4. Artificial superhydrophobic surface examples imaged by scanning electron microscopy (SEM). (a) Micro-spikes on Si substrates [53]. (b) Heavily structured copper film surface [53]. (c) Silicone rubber replicates of Alocasia structure through molding [53]. (d) Hierarchical structures using Si micropillars covered with lotus wax tubules [54]. (e) Teflon nanocone arrays [55]. (f) Porous i-PP structures from solution drying [56]. (g) Carbon nanotube forest grown by PECVD [57]. (h) TiO_2 particles paint [58].

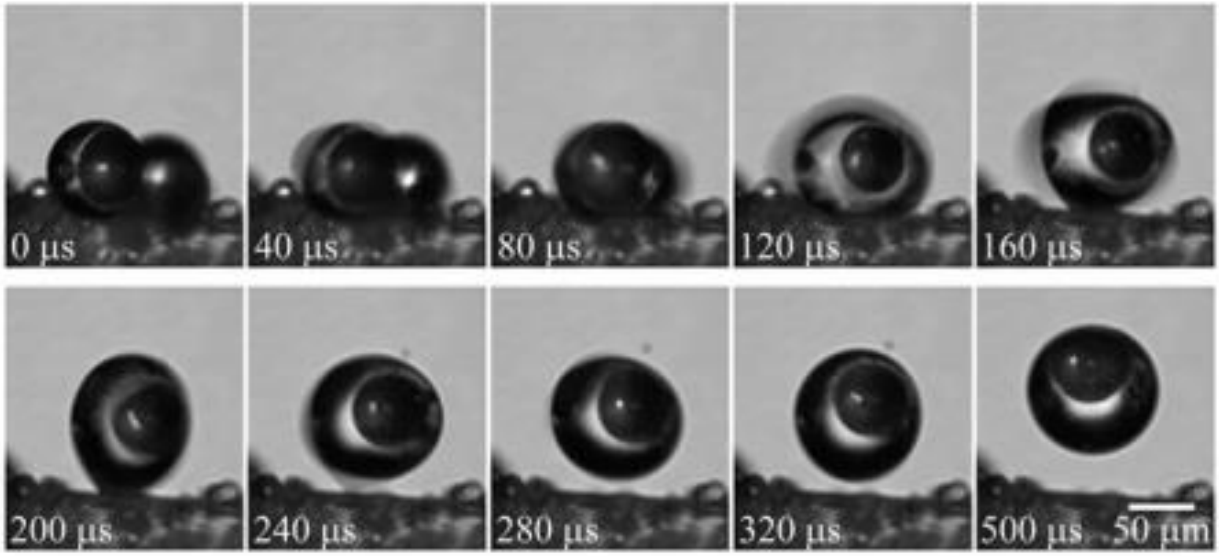

Figure 1.5. Water vapor condenses and spontaneously jumps off a cicada wing surface, encapsulating 50 μm glass beads [59].

Because of the droplet repellency and low adhesion, a condensed droplet on a chilled superhydrophobic substrate can be spontaneously removed. When the tiny droplets coalesce, the released energy can power the out-of-plane jumping of the droplet [60, 61]. Such a jumping condensate process was applied for the surface cleaning mechanism [59]. Inspired by cicada wings, K. Wisdom, *et al*. studied their wing structures and found the self-cleaning mechanism by jumping condensate process [59]. The cicada wing cuticle surface consisted of conical hydrophobic arrays, resulting in super-hydrophobicity with a water contact angle in the range of 148°-168° depending on the location. When the wing surfaces were exposed to vapor flow, the adhering particles or contaminants could be cleaned because of the water condensation process. Shown in Fig. 1.5, the particles were detached from the surface by the water droplet's out-of-plane jumping upon coalescence. The capillary-inertial oscillation of the merged droplet provided the required kinematic energy. The force between the jumping droplet and the particles in contact scaled with the capillary force: $f \sim \gamma R_p$, where γ is the surface tension and R_p is the droplet radius of curvature.

Due to the scaling law, for small particles, it was less favorable to remove the droplet by inertial forces like gravity, vibration, and centrifugal forces (scaled with R_p^2) or by hydrodynamic forces like wind blowing (scaled with R_p^3). The jumping condensate processes (scaled with R_p) provided an advantageous mechanism to dislodge particles from the surface by overcoming adhesion forces (van der Waals force and capillary bridging force) to the substrate.

1.2.5 *Omniphobic Surfaces*

Water possesses a high surface tension compared with most other liquids (except for mercury). Low surface tension liquids rarely exist in nature so the naturally evolved surfaces can barely repel artificial low surface tension liquids in our daily lives [62]. According to the simple theoretical derivation, by combining the Wenzel model and Cassie-Baxter model equations, we obtain the transitioning critical angle between the two states expressed as:

$$\cos \theta_c = (\phi_{solid} - 1) / (r - \phi_{solid}) \tag{1-14}$$

where θ_c is the critical transition contact angle for a droplet from Wenzel state to Cassie-Baxter state [63]. By definition, we have $r \geq 1 \geq \phi_{solid}$, and θ_c is required to be at least 90° to make the transition happen because the right-hand side of equation (1-14) cannot be positive [62]. For low surface tension liquids like hexane and decane, no existing natural or artificial surface coatings can achieve such a high contact angle of the liquids [64, 65].

Researchers have successfully created artificial superomniphobic surfaces with the assistance of re-entrant structures [62] or doubly re-entrant structures [66, 67], in which curvature is another key factor other than surface chemical composition and roughness. The key to realizing superomniphobic surfaces is that the liquid hanging between surface asperities cannot have higher contact angles than given by the intrinsic material wettability [68, 69]. More specially, as shown in Fig. 1.6 (a), if the advancing TPL forms a smaller contact angle, then an equilibrium state can

be reached that prevents the droplet from further impalement [70]. The liquid-air interface inside the re-entrant or doubly re-entrant structure remains convex and the net capillary force generated is upward. According to equation (1-8), when ϕ_{solid} is small (<6%), the surface can repel extremely wetting liquids ($\theta_c^* > 150°$ with $\theta \sim 0°$). However, the liquid is difficult to maintain in suspension with small ϕ_{solid} because the liquid will impregnate into the rough structures without enough solid support. A doubly re-entrant structure is thus necessary with vertical, thin, and short overhangs to minimize the projected solid areas while increasing the solid fraction by vertical surfaces (sidewall angle ~90°). As demonstrated in Fig. 1.6 (b), on a conventional pillar-like superhydrophobic surface, a water droplet is suspended on the micropillar structure when the pillars are hydrophobic. However, for low surface tension liquid, the liquid-solid contact line overcomes this barrier and reaches the lower edge of the re-entrant structure, as shown in Fig. 1.6 (c). For a completely wetting liquid, the contact line further wets down the overhang and reaches the tip of the curvature (Fig. 1.6 (d)). Because of the doubly re-entrant structure, the liquid-solid contact line stops wetting at the interior edge of the vertical overhangs while keeping ultra-low contact angle.

To fabricate the superomniphobic surfaces, efforts have been made to explore re-entrant and doubly re-entrant microstructure arrays. Fig.1.7 (a)–(c) show different types of re-entrant designs. The micro hoodoo structure in Fig. 1.7 (a) was made by reactive ion etching of the SiO_2 layer on top of a Si substrate followed by isotropic etching of the Si substrate using XeF_2. The process resulted in Si pillars with SiO_2 caps [71]. Fig. 1.6 (b) started with lithographic patterning on a copper substrate, followed by through-mold and over-mold electroplating to form hemispherical mound copper structures atop a photoresist layer [72]. After the photoresist strip, the mushroom-like copper structure was created. Fig. 1.7 (c) demonstrates a nano-nail structure by using a deep reactive ion etching process to fabricate tall silicon pillars with SiO_2 nail caps atop [73]. All the

three designs required a fluoropolymer coating as a finishing step to maintain the low surface tension required for stable fluid suspension. A vapor phase immersing deposition process was usually applied on SiO_2 surfaces and a solution soaking process could be applied on metal surfaces. The self-assembled monolayer, terminated with the tricholorosilane group or thiol head group, formed a stable covalent bond and modified the surface energy with a fluorinated tail group [74]. The silanization process was widely used for many surfaces to adjust the surface wetting behaviors [75-78].

As an alternative to lithography processes, A. Tuteja, *et al*. synthesized a class of fluoropolymers (polyhedral oligomeric silsesquioxane, POSS, shown in Fig. 1.7 (d)), with which the substrate was coated by electrospinning. The surface tension of the electrospun fiber mat could be altered by changing the mass fraction ratio of fluoro-POSS and a mildly hydrophilic polymer, thus systematically tuning the water contact angle [62, 71].

Deng, *et al*. created a transparent superomiphobic surface using candle soot as a template, shown in Fig. 1.7 (e) [79, 80]. The soot consisted of piles of nano carbon spheres with a diameter range of 30-40 nm. After depositing the soot on the glass substrate, a layer of silica shell was formed utilizing chemical vapor deposition (CVD) of tetraethoxysilane (TES) catalyzed by ammonia. The sample was sintered in the oven for 2 hours at 600 °C to burn away the carbon cores and link the silica nanoshells. The surface kept good transparency and superomiphobicity up to 400 °C.

Besides the re-entrant structures, doubly re-entrant structures have been fabricated, presenting superior surface properties as compared to re-entrant structures. Learning from smart springtail skins [66], T. Liu, *et al*. microfabricated structures with doubly re-entrant overhangs, shown in Fig. 1.7 (f) [67]. Due to its particular geometry, the surface could repel any of the existing fluids

even without fluoro-polymer treatment of the final surface. Because of a pure combination of SiO_2 and Si, the surface would also withstand high-temperature environments over 1000 °C. Derived from this process flow, metal or polymeric doubly re-entrant omniphobic surfaces were successfully fabricated as well.

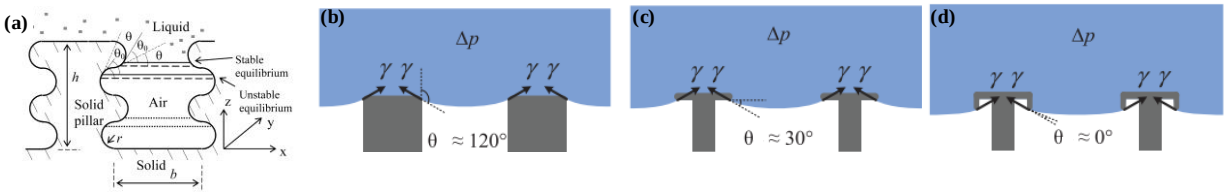

Figure 1.6. Liquid-solid contact angle required for stable liquid suspension on (a) Surfaces with both curved bumps and grooves [70], (b) micro-pillar structures, (c) re-entrant structures, (d) doubly re-entrant structures [67].

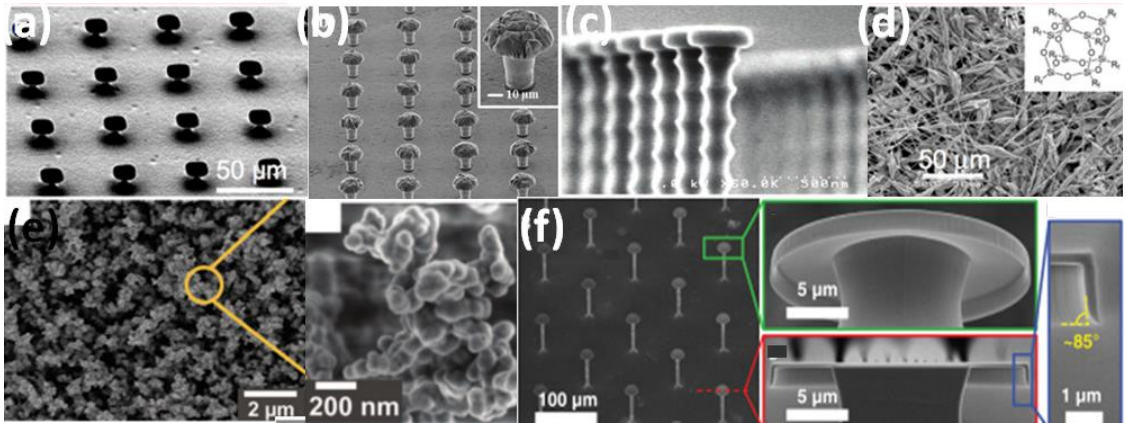

Figure 1.7. Examples of superomniphobic surface designs. (a) Micro hoodoo structures with a rectangular SiO_2 cap on Si micro-pillars [71]. (b) Mushroom structure of copper surfaces [72]. (c) Nano-nail structures [73]. (d) Fluorinated electrospun fibers [71]. (e) Candle soot structure after being coated with silica nanoshell and after carbon core removal by high-temperature sintering [79]. (f) Microposts with doubly re-entrant overhangs [67].

1.2.6 *Superhydrophilic Surfaces*

Superhydrophobicity is not the exclusive strategy to realize self-cleaning functionality, which can

also be realized while the water droplet contact angle atop a surface is extremely low (close to zero). The simplest way to increase the surface hydrophilicity is by oxygen plasma treatment, as demonstrated by B. Gupta, *et al.* [81]. Their process only modified the surface properties without altering the bulk substrate material. Experiments proved that the treated surface had anti-fogging and anti-fouling properties, but the hydrophilicity would decrease over time [82].

Another approach was to take advantage of both the light-induced superhydrophilicity [83-85] and the photocatalytic properties of TiO_2 thin films, namely the "Photo-Kolbe" reaction [82, 86]. The as-prepared TiO_2 surface water contact angle is ~72°. The UV exposure creates oxygen vacancies at bridging sites favorable for dissociative water adsorption (Ti^{3+} sites instead of Ti^{4+} sites), making the water contact angle close to 0°. Microscopically, after UV radiation, the TiO_2 surface wettability is not heterogeneous anymore, and the hydrophilic regions are distributed across the surface with area sizes in the sub-micrometer range, based on measurements by friction force microscopy. Macroscopically, the water will spread on the surface instead of forming droplets, to wash away surface contaminants easily [83].

The photo-induced oxidation/decarboxylation/fragmentation of organic acids is well-known for photo-semiconductors like TiO_2 or ZnO [87-92]. The TiO_2 preparation can use wet chemical processes like sol-gel, dip-coating, or spin-coating processes [93, 94]. A post calcination process is usually required to improve the adhesion between the TiO_2 film and the substrate [95]. Upon UV radiation (< 385 nm) of the TiO_2, the proton with an energy exceeding the bandgap would excite an electron (e^-) from the valence band to the conduction band, leaving a hole (h^+) on the valence band. Valence band holes react with the water through a strong oxidization process on the surface to produce reactive hydroxyl radicals (·OH) and convert surface contaminants, especially

organic residues, into byproducts like water or CO_2 [94]. Because of the weakening of the bonding, the surface contaminants are easily washed away by rain.

1.2.7 *SLIPS Surfaces*

Solid substrates have been modified to create superhydrophobic or superhydrophilic surfaces by etching of physically rough texture or by chemical modification. However, Wong, *et al*. developed a system to create a liquid repellant surface, naming it "slippery liquid-infused porous surface" (SLIPS) [96]. Inspired by the Nepenthes pitcher plant [97], Fig. 1.8 (a) shows the fabrication process of the SLIPS surface. A porous solid surface was infused with low surface tension and chemically inert lubricating liquid, which wicked into the porous substrate while being immiscible and repelling to the test liquids applied to the surface. The contact angle hysteresis for sessile water drops was as low as 2.5° and the sliding angle was smaller than 5°. Fig. 1.8 (b) and Fig. 1.8 (c) demonstrates the outstanding anti-fouling performance of the SLIPS surface by applying crude oil and human blood. In comparison with superhydrophobic surfaces and hydrophilic surfaces, no stains were left on the surface. Both oil and blood would quickly slip away from the SLIPS surface. Besides the superb repellency, the SLIPS surfaces also have self-healing properties [96]. Because of the surface ultra-smoothness and lack of nucleation sites [98-101], no frost formation or a reduced ice adhesion was observed on cold SLIPS surfaces.

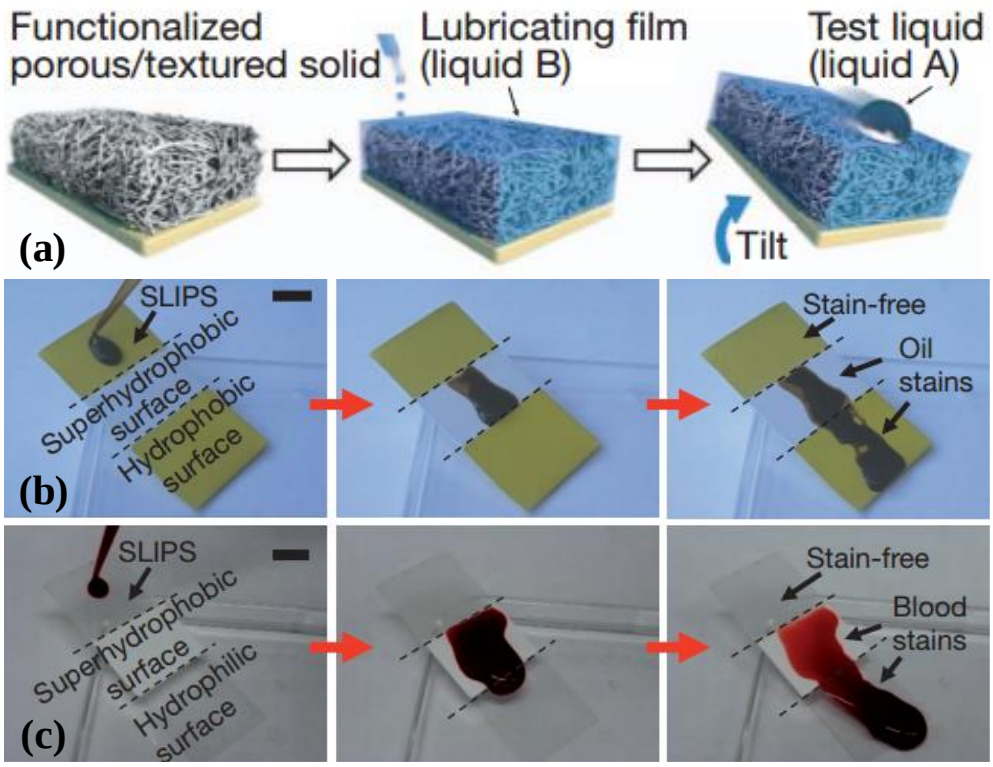

Figure 1.8. (a) SLIPS surface fabrication process flow. Low surface energy, chemically inert fluid was infused into the porous solid substrate. The surface remained smooth with lubricating film between the substrate and the applied liquid. (b) Crude oil and (c) blood movement on SLIPS, superhydrophobic, and superhydrophilic surfaces [96].

Concerning bio-fouling applications, extensive studies have been performed on superhydrophobic surfaces [102-107]. However, the anti-biofouling property of superhydrophobic surfaces could be short-lived as the air-bubble layer trapped between the liquid and the rough surface is not stable and may disappear within several hours [108]. More bacterial adhesion could end up on the superhydrophobic surfaces due to the high surface roughness when compared with intact smooth surfaces. Extensive work has been explored by adopting SLIPS surfaces to prevent bio-fouling issues by various fabrication methods, which were more promising and with better performance than superhydrophobic surfaces. A. Epstein, *et al.* adopted SLIPS surfaces to prevent surface bio-film attachment [109]. Shown in Fig. 1.9 (a), the SLIPS surfaces were fabricated with

porous fluoropolymer substrates (with a pore size of 0.2 μm). By staining the surface with a bacterial culture solution, the SLIPS surface can reduce the cell attachment compared with superhydrophobic surfaces. The coffee ring effect of the biofilm was suppressed on SLIPS by leaving only a pellet of bio-stains after evaporation. Similar liquid infused porous substrate structures were obtained by phosphoric acid etching of enamels [110].

D. Leslie, *et al*. created a SLIPS surface with self-assembled monolayers (SAM), shown in Fig. 1.9 (b). The structure was applied to a wide range of smooth medical device surfaces, which repelled flowing blood and prevented thrombosis [111]. A molecular tethered perfluorocarbon (TP) layer was first coated on the smooth surfaces by soaking the plasma treated surface in the liquid solution. Then a mobile layer of perfluorodecalin (LP) was applied, forming a tethered-liquid perfluorocarbon (TLP) surface. By exposing the uncoated and TLP coated acrylic surfaces to fresh human blood, the TLP surface had 27-fold less platelet adhesion and platelets were considered as one of the major components causing thrombosis. Both *in vitro* and *in vivo* experiments showed promising results, demonstrating that the TLP surfaces were resistant to the physiological shear stress brought by the blood flow while reducing the protein adhesion and thrombosis for at least 8 hours.

Beyond the silane liquid soaking process to create the TP layer, M. Badv, *et al.* improved the hydrophobic salinization process with a more robust, reproducible, and less disruptive chemical vapor deposition (CVD) process in vacuum [112, 113] (Fig. 1.9 (c)). Coronary catheters were treated by two silanization processes, followed by adding perfluorodecalin or perfluoroperhydrophenanthrene to make the TLP surface. The CVD treated surfaces provided better anti-thrombotic performance compared with silane liquid solution soaking processes. As shown in Fig. 1.9 (c), CVD treated catheter surfaces found no blood clot or protein adhesion after

blood immersion. By mixing different self-assembled monolayer silanes (aminosilane and fluorosilane) during the surface treatment, tunable cell repellency, and selective binding of antibodies can be realized. The target anti-bodies would be anchored by the aminosilane while the fluorosilane will repel the non-desired cells, proteins, or plasma clotting assays, creating the bio-functional lubricant-infused surfaces (BLPS) [114].

SLIPS can be fabricated on porous micropillar arrays with sharp overhang structures [115]. As shown in Fig. 1.9 (d), the liquid on top of such surfaces meets a new liquid-air interface, compared with solid-air interfaces of the normal superhydrophobic or superomniphobic designs without liquid infusion as discussed above. The micropillar arrays with sharp overhang structures and nano-porous micropillar top surface finish were created by direct laser writing, which can process any arbitrary 3D components with sub-micrometer resolution. A layer of Al_2O_3 by atomic layer deposition was coated on the outer layer of polymeric micropillars and fluorinated by SAMs. Low surface tension fluid was dropped directly on the micro-pillar porous surfaces and confined by the micropillar surface roughness as well as the overhangs. The composite surface designs can repel low surface tension fluids while reducing more than twice of the adhesion force, as measured with scanning droplet adhesion microscopy.

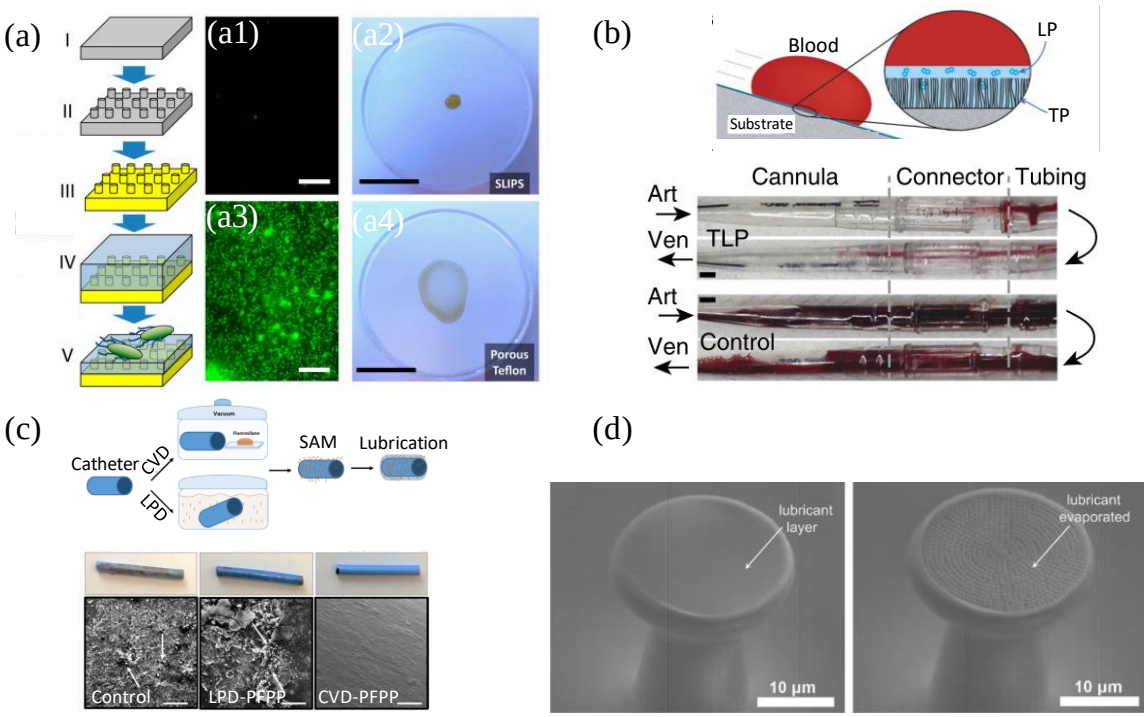

Figure 1.9. (a) The fabrication process of the SLIPS surface using a porous substrate and bio-fouling experiment with and without liquid infusion [109]. (b) SLIPS surface fabricated with liquid soaking deposited SAM layers [111]. The experimental results showed TLP modified tubing and control tubing after 8h of blood flow. The blood flow through arterial (Art) or venous (Ven) cannula is indicated by the black arrow. (c) SLIPS surface fabricated with both liquid soaking and vapor deposited SAM [112]. (d) SEM images of SLIPS and doubly re-entrant superomniphobic composite structures. The left image shows the surface with lubrication and the right image shows the surface after lubricant evaporation [115].

1.3 Active Self-cleaning Microsystems

Besides employing passive surface modification techniques, microsystems can be designed to actively remove unwanted surface contaminants or fluids [8]. Many strategies have been tested using surface tension gradients, electrostatic fields, and vibrations. Moreover, geckos can clean their feet dynamically while naturally walking with hyperextension. In such systems, water droplet movement or dust removal can be accomplished systematically while applying more controlled forces. Thus, the active self-cleaning approach can be utilized in combination with passive surface

modification to improve cleaning efficiency. In this part, we will first introduce the surface cleaning strategies by combining the superhydrophobic and SLIPS surface design with droplet manipulation. Then we will discuss surface dust removal techniques by electro-dynamic screen, repelling surface contaminants by a high alternating voltage. At last, self-cleaning synthetic adhesives inspired by gecko setae structures are discussed.

1.3.1 *Self-cleaning Surfaces by Water Droplet Transport*

Microfluidic systems have been developed using MEMS technology and widely applied for biomedical and chemical applications. The recent development of microfluidic systems using micro- or nano-liter water droplet transport, commonly known as digital microfluidics (DMF), offers the potential for a wide range of applications [116]. To control the water droplet transport, researchers have focused on creating surface tension anisotropy at the interface of gas, liquid and solid, defined as the three-phase contact line (TPL). DMF systems can be used to direct water droplet transport along the surface using chemical gradients [117], thermal gradients [118], electrowetting-on-dielectric (EWOD) [119-121], surface acoustic waves [122], and microtextures [123, 124]. Dust particles or undesired fluids along the path of the water droplet movement can be carried away to other locations, leaving the desired surface regions clean and functional.

Latip, *et al.* explored the anti-fouling properties using EWOD to transport the droplet. The top coatings include hydrophobic (Cytop) and superhydrophobic (NeverWet®) materials [125]. Different concentrations of protein solutions were prepared. A similar test bench setup as shown in Fig. 1.10 (a) was performed to test the contact angle hysteresis by gradually increasing and then reducing the voltage within a period. Compared with superhydrophobic surfaces, the contact angle hysteresis greatly increased on Cytop surfaces with increased protein concentration, maximum applied voltage, and the period with the voltage applied. Higher roll-off angle and afterward higher

fluorescence intensity with labeled protein were observed on the Cytop surface, showing a stronger protein adhesion to the Cytop. As for the droplet transport, both closed parallel plate configuration (Fig. 1.10 (b)) and open coplanar configuration were tested with superhydrophobic coatings. On the coplanar system, a droplet of 35 μL was applied, and the actuation was difficult to control since the droplet continued to roll on the surface due to low friction. However, in the parallel plate system, a droplet with only 5 μL was needed and was successfully transported, merged, or mixed.

M. Jönsson-Niedziółka, *et al*. showed droplet transport with a parallel plate system configuration to remove bio-particles [126]. The top and counter electrodes were separated by 300 μm spacers. A square wave voltage was applied to the selected base electrodes at the frequency of 1 kHz and the switching time between adjacent electrodes was adjusted based on droplet movement speed. The water droplet displacement was driven by the surface wettability change induced by the voltage. The cleaning efficiency was defined as: $\%\text{efficiency} = (1 - N_{in}/N_{out}) \times 100$, where N_{in} is the average number of particles inside the water droplet pathway and N_{out} is the average number of particles outside the water droplet pathway. Examples of water droplet transport along the electrodes and cleaning of the surface are presented in Fig. 1.11. Synthetic particles like polystyrene latex microspheres and bio-particles, including proteins, bacterial spores, and viral stimulants were tested with the system. When the substrate surface was designed to be superhydrophobic, more than 90% of cleaning efficiency could be reached with water droplets even for protein particles, which usually have high adhesion to the substrate and are hard to clean.

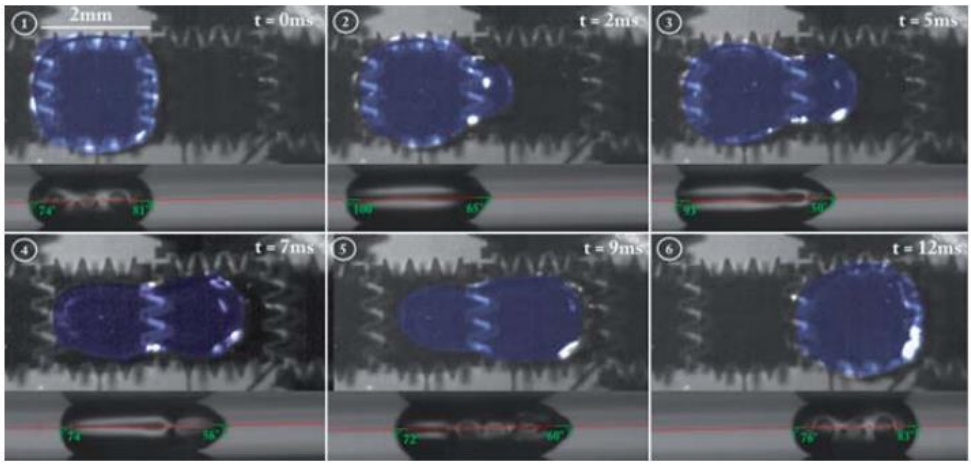

Figure 1.10. Both top and side views of water droplet transport on the superhydrophobic surface at different times [126].

Y. Zhao, *et al*. developed a similar EWOD system for the sampling of microparticles (Fig. 1.12) [127]. The actuation electrodes were insulated with a dielectric layer (SiO_2) and coated with hydrophobic (Teflon) coatings. Driven by sequentially actuated electrodes, the water droplet swept along the surface and picked up particles. The path covered by the water droplet became clear to visual inspection, meaning that most of the particles were collected by the moving water droplet.

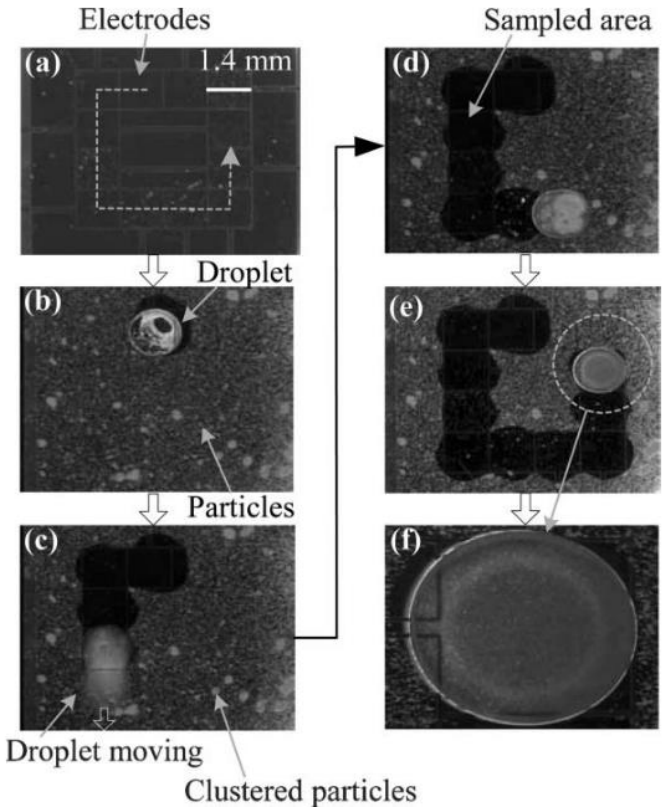

Figure 1.11. (a-e) Glass beads are collected sequentially using water droplets. The glass beads are suspended inside the sweeping water droplets. The dashed line in (a) indicates the path of the droplet for particle sampling and cleaning [127]. (f) shows a close-up view of the droplet with suspended sampled particles.

Besides superhydrophobic surfaces, H. Geng and S.K. Cho combined the SLIPS with an open coplanar EWOD system [128]. The dielectric layer was SU8 and the top coating was replaced with a porous fluoropolymer film infused with lubricating fluid in this configuration. Droplets can be transported along with the SLIPS under voltage actuation. Bovine serum albumin (BSA) protein solution left tiny stains after evaporation on SLIPS while a large “coffee ring” bio-stain pattern was left on hydrophobic coatings. The bio-stain could be cleaned by droplet actuation as shown in Fig. 1.12.

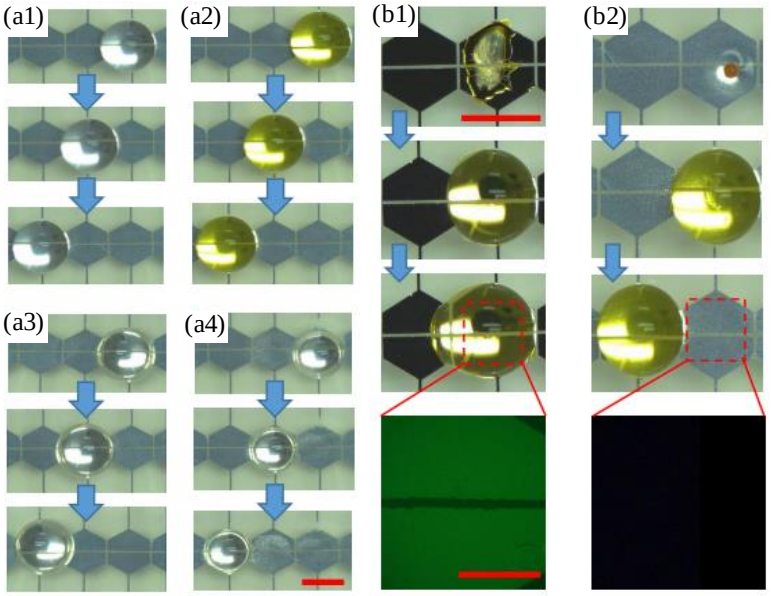

Figure 1.12. (a) Different liquids transported on EWOD-SLIPS surfaces: (a1) DI water, (a2) BSA solution, (a3) propylene carbonate, (a4) isopropyl alcohol. (b) A droplet cleaning bio-stains left by evaporation: (b1) droplet fails to move on hydrophobic coatings due to biofouling, (b2) droplet moves and cleans the bio-stain. The green in the fluorescent images indicates the BSA residues on the surfaces [128].

An EWOD system can also be designed to remove unwanted small amounts of water residue adhering to surfaces. K. Y. Lee, *et al*. developed an open coplanar EWOD system without a top cover plate targeting miniature camera surfaces for automobiles [129]. The electrodes were fabricated with indium tin oxide (ITO), which is transparent and can be integrated with the camera lens as a lens cover. 1~70 μL water droplet sizes were tested with different threshold voltages under surface inclination angles from 0° to 180°. Fig. 1.13 shows a demonstration of water droplet removal as well as micro-particle removal on the camera lens cover.

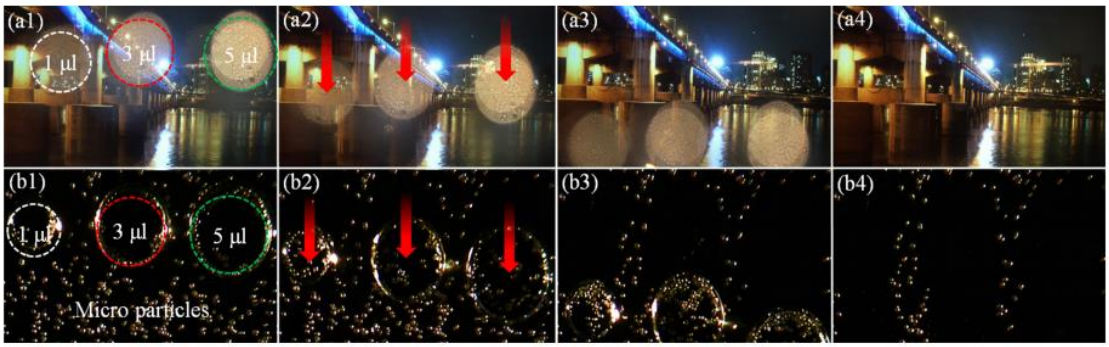

Figure 1.13. Sequential images of cleaning of (a) water droplets and (b) particles with different volumes on the lens cover of a smartphone camera [129].

1.3.2 *Self-cleaning Surfaces by Electro-static Charge*

Electrodynamic screen devices have been developed to remove dust particles for scenarios where the water resource is scarce or not available, as in desert regions. The concept of transporting particles using an electrostatic traveling wave was first developed by Masuda [130], where a series of electrodes were connected to the AC source to serve as contactless conveyors. Mazumder, *et al*. developed an electrodynamic screen (EDS) with a traveling-wave AC field to create a self-cleaning system for the problem of dust accumulation both on Mars missions [131-133] and on terrestrial solar panels [134]. Fig. 1.15 demonstrates a typical EDS design with dust accumulation and cleaning effect before and after the AC voltage was supplied [134, 135]. Interdigitated electrodes were fabricated on printed circuit boards or glass substrates. The electrodes were insulated with a layer of a transparent polymer. As AC voltage was applied (700~1000 V peak-to-peak), the electrodynamic force applied to the particles overcame gravity and the viscous force of air to lift the particles from the surface and transported them to different locations. Over 90% of cleaning efficiency could be achieved by optimizing the frequency, voltage, and signal shape. The power consumption and the cleaning time were only in the order of milliwatts and tens of seconds. Other EDS systems were designed employing a standing-wave AC field, with simplified electrical circuit

designs and high voltage resources. Bing Guo, *et al.* systematically studied the EDS efficiency in terms of EDS dimension size, dielectric cover thickness, dust loading level, dust deposition methods, and particle size distribution for solar energy applications [136, 137]. 90% of dust removal efficiency could be achieved within 10 seconds of energizing at a dust loading level of 100 $g \cdot m^2$ with a voltage level of 6 kV_{pp}. Dust removal efficiency improved with increased dust loading levels, reduced dielectric cover thickness, and large dust agglomerations.

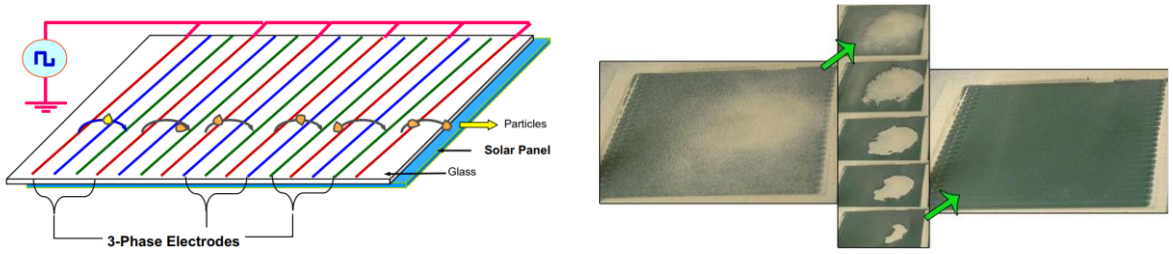

(a) (b)

Figure 1.14. (a) Schematic view of a typical EDS design [135]. (b) Sequential images of the dust removal processes on top of the EDS panel by electrodynamic force [134].

1.3.3 *Self-cleaning Surfaces by Gecko Tape*

Geckos have attracted the attention of researchers for many years due to their ability to climb up smooth vertical surfaces. The gecko's foot has millions of hairs, named keratinous setae, providing large van der Waals adhesive forces [138, 139] that prevent the gecko from falling off from smooth vertical surfaces. Geckos have intimate contact on various surfaces with their sticky toes but their setae virtually always keep clean and dry [140]. W. R. Hansen and K. Autumn [141] studied the gecko's keratinous setae and found the self-cleaning mechanism: Each of the millions of setae on the gecko's toe pads has hundreds of spatulae, sub-micron triangular structures aligned in parallel with each other but not normal to the toes. An imbalance exists between the adhesive force of one or more spatulae to the dirt particles and the dirt particles to the substrate surface. When touching

the clean substrate surface, the dirt has higher contact areas to the surface and tends to stick to the surface rather than the gecko's spatulae. The adhesive and shear force of a contaminated gecko's foot is recovered gradually by successive steps on a clean surface. By comparing the SEM images of spatula arrays after dirtying with microspheres and after several simulated cleaning steps, most of the spatula surfaces were free of micro sphere contamination. The shear force measurement also showed the gradual restoration as the simulated step numbers increased.

Self-cleaning adhesive tapes have been developed using carbon nanotubes [142] and polymer microfibrils [143] mimicking gecko setae. Fig. 1.16 (a) shows contaminated polypropylene fibrils fabricated by a thermal casting process. An estimated 42 million fibrils were created per square centimeter with an average length of 18 μm and an average radius of 18 nm. After 30 contacts on a clean glass substrate with standard simulated gecko steps (Fig. 1.17), 60% of the Au microspheres were removed from the tip of the micropillars (Fig. 1.16 (b)). The shear force could be restored by 33% after 20-25 cleaning steps. As a comparison, a conventional pressure-sensitive adhesive (PSA) went through the simulated steps. The PSA surface was almost completely covered by the Au microspheres, shown in Fig. 1.16 (d).

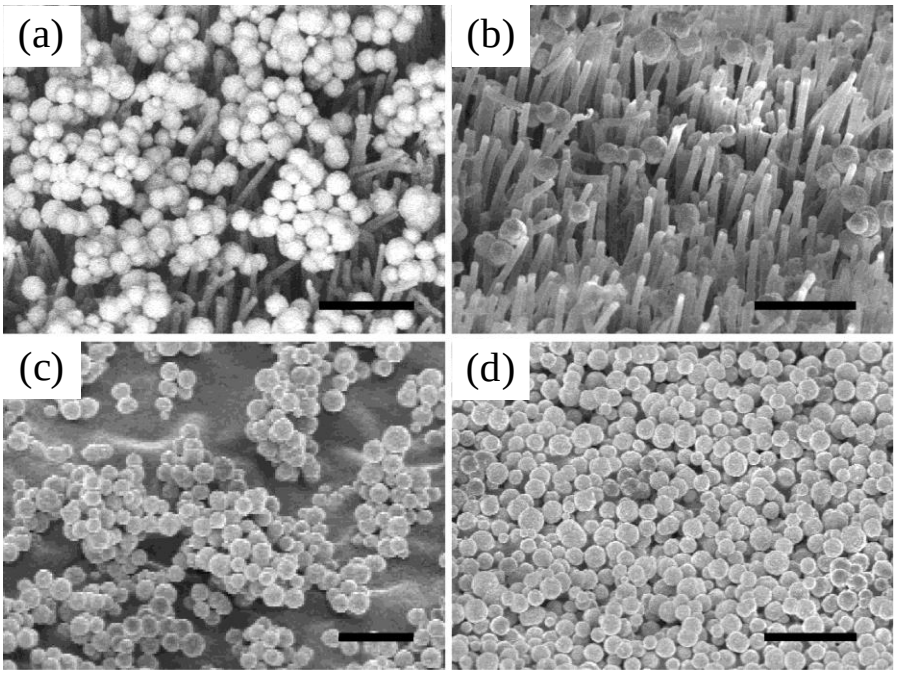

Figure 1.15. (a) Microfiber adhesive contaminated with gold microspheres. (b) Microfiber adhesive after 30 contacts (simulated steps) on a clean glass substrate. Some of the microspheres were trapped inside the microfibers. (c) Conventional PSA surface contaminated with microspheres. (d) PSA surface fully covered by the Au microparticles after the same simulated steps [143].

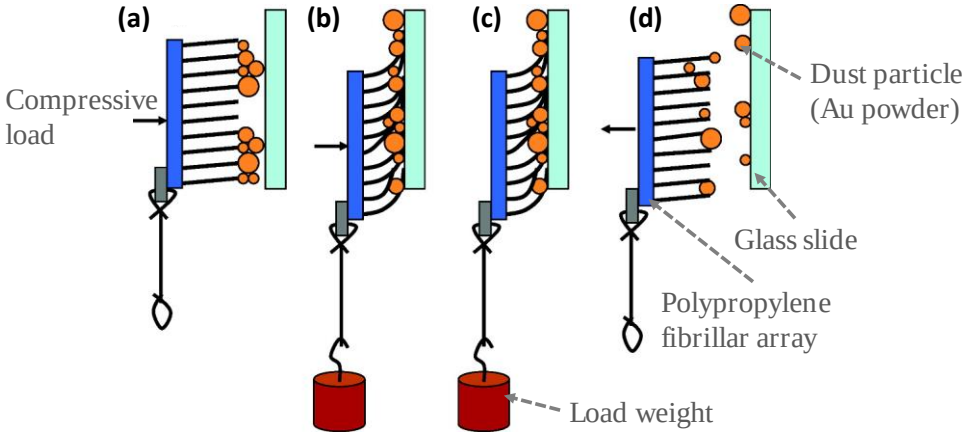

Figure 1.16. Standard protocol of mimicked gecko step cycle: (a) Normal compressive force was applied on the backside of the fiber substrate. (b) Applying shear load added to the compressive force. (c) Removing the compressive force to make the load a pure shear force. (d) Detaching the sample from the clean surface [143].

1.4 CHAPTER 1 CONCLUSIONS

Self-cleaning surfaces can have a broad range of applications from bio-fouling in medical instrumentation to building and vehicle windows to solar panel cover glass in the outdoor environment. The examples mentioned in Chapter 1 provide suggestions and protocols for designing and characterizing self-cleaning surfaces and systems. Compared with passive superhydrophobic or superhydrophilic surface designs, active cleaning systems can perform the cleaning with more delicate control of water movement, and more efficient use of water resources. Both dust and unwanted water residue can be removed at the same time.

Chapter 2. SELF-CLEANING SURFACE DESIGN FOR SOLAR PANELS USING ANISOTROPIC RATCHET CONVEYORS AND VIBRATIONAL SYSTEM

To design the active self-cleaning surface systems with a limited amount of water resources, directional droplet transport is necessary to steer the water droplet along the whole surface and pick up the dust particles. Meanwhile, transparency of the coating material on the solar panel cover glass is required to minimize the amount of light blocked or reflected by the extra coatings. In Chapter 2, we will introduce a self-cleaning surface system developed by combining surface micropatterning and mechanical vibrations. The droplet can be directionally transported along the surface and the movement path can be precisely defined by the micropatterns to cover the whole surface area. The micropatterns are fabricated by creating hydrophilic curved rungs on the hydrophobic background, termed as anisotropic ratchet conveyors (ARCs).

2.1 INTRODUCTION

Solar energy systems, including photovoltaic systems (PV), concentrated photovoltaic systems (CPV), and concentrated solar power systems (CSP), are mostly built in semi-arid or desert areas, that are abundant in sun irradiance but with high levels of sand and dust [144]. The accumulation of dust and environmental contaminants over time, which is often termed as “soiling” or “fouling” issues, has become a growing concern for the PV module efficiency and reliability [145]. The composition of dust particles primarily consists of quartz and silicate minerals but also has lower concentration elements like area-specific minerals, agricultural components, and fuel components. The general dust particle size distribution is in the 30~160 μm range [146, 147]. Dust particles will accumulate on the cover glass of the solar panel modules and reduce the amount of light that

reaches the solar cells to be converted to electricity. According to the solar module monitoring results from Thar desert, India [144], the conversion efficiency loss can be up to 40% over time. The cover glass is the first interface for the PV modules to interact with the incident photons. It is important to maintain this interface clean to ensure the maximum solar power conversion efficiency. Mitigating the soiling of the PV module surfaces on a periodic basis is usually required to maintain efficiency. However, the solar module installations are often inconvenient to access for maintenance staff. The cleaning of solar panel surfaces becomes problematic without labor-free and water-saving approaches.

The traditional PV module cleaning processes involve brushing and water sprinkle rinsing. The methods are labor-intensive and require many water resources. To find an automatic self-cleaning system with reduced labor and water usage, two ARC systems and their corresponding fabrication processes are proposed: a self-assembled monolayer (SAM) based system and a fluoropolymer thin film-based system. Meanwhile, droplet transport mechanisms are discussed by characterizing the anisotropic force, droplet transport speed, dependency on vibration frequency, and power consumption. The optical transmittance and solar power output performance are investigated on the assembled solar module level. A proof-of-concept cleaning demo is presented by assembling ARC coated soda-lime cover glass with solar cells.

2.2 System Design

Anisotropic rachet conveyors are created by patterning curved hydrophilic rungs on the hydrophobic treated substrate (silicon wafer or soda-lime glass). A typical setup to drive the water droplet to move forward is shown in Fig. 2.1 (a) and the top view of the patterned ARC is shown in Fig. 2.1 (b). The substrate patterned with ARC is mounted on the mechanical vibrational stage (electromagnetic linear motor). The vibration stage is subjected to the external driving signal

(typical sinusoidal input voltage and current) to supply orthogonal vibrations. The ARC has been widely researched and can be created with either physically etched pillars [123, 148] or chemically modified flat surfaces [124] to transport the droplet. As a sessile droplet is pipetted on the ARC surface, the water droplet wets the ratchet patterns along the rungs, creating an air-water-solid three-phase contact line (TPL) along its outer edge. We denote the portion of the water droplet edge that aligns with the rung curvature, which has a mostly continuous TPL, as the leading edge of the droplet, while the other portion, which has only intermittent TPLs across different rungs, is called the trailing edge of the droplet. During each vibration cycle, the leading edge provides a higher pinning force than the trailing edge as the water droplet expands and recesses (Fig. 2.1 (c)). This asymmetry in pinning forces causes water droplets to move toward the direction of the rung curvature.

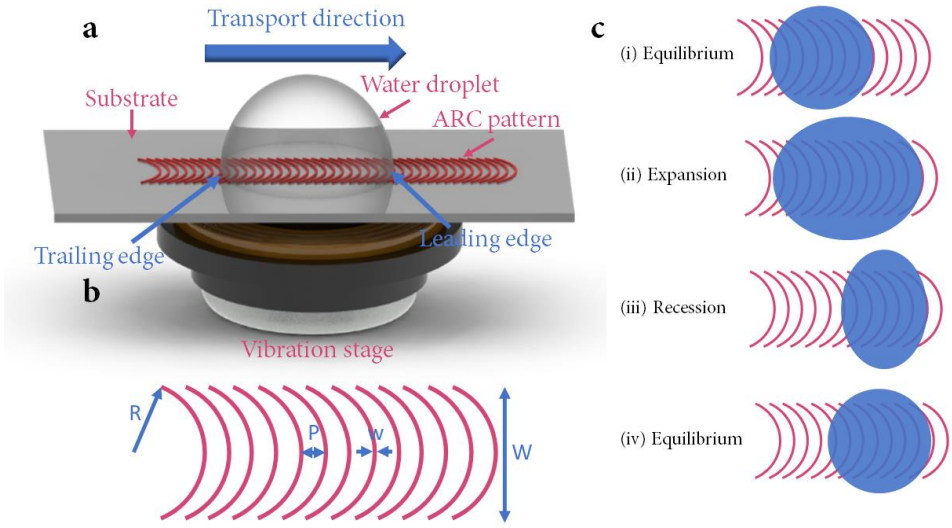

Figure 2.1. (a) Schematic of the typical setup to transport the droplet using ARC. (b) Top view of the ARC design. The parameters include the rung radius of curvature (*R*), ARC rung center to center period distance (*P*), hydrophilic region width (*w*), and the total ARC track width (*W*). (c) The interaction between the droplet and the ARC during each vibration cycle. The droplet footprint expands as the substrate accelerates upwards and recesses as the substrate accelerate downwards during each vibration cycle.

The droplet motion originates from the force asymmetry and hysteresis at the leading and trailing edges of the contact line on the ARC, which consists of heterogeneous regions with hydrophobic/hydrophilic patterns. The effective force exerted on the contact line along the axis of the ARC can be described as:

$$F = d\gamma_{LG}\left(\chi_{phob}\cos\theta_{phob} + \chi_{phil}\cos\theta_{phil} + \chi_b\cos\theta_b\right) \tag{2-1}$$

with d the diameter of the droplet, γ_{LG} the liquid-gas surface tension, and θ_{phob}, θ_{phil}, θ_b the respective equilibrium contact angles on the hydrophobic material, on the hydrophilic material, and their boundary. χ_{phob}, χ_{phil}, χ_b are the portions of the contact line on the respective materials projected orthogonally to the axis of the ARC. $\chi_{phob} + \chi_{phil} + \chi_b = 1$ for the leading edge and $\chi_{phob} + \chi_{phil} + \chi_b = -1$ for the trailing edge. To understand the behavior of the droplet, we need to look at the force asymmetry between the leading and trailing edges of the droplet, as well as the force hysteresis between the advancing and receding contact lines. This leads to 4 distinct equations:

$$F_{lead,adv} = d\gamma_{LG}\begin{pmatrix}\chi_{lead,phob}\cos\theta_{phob,adv} + \chi_{lead,phil}\cos\theta_{phil,adv}\\ +\chi_{lead,b}\cos\theta_{b,adv}\end{pmatrix} \tag{2-2}$$

$$F_{trail,adv} = d\gamma_{LG}\begin{pmatrix}\chi_{trail,phob}\cos\theta_{phob,adv} + \chi_{trail,phil}\cos\theta_{phil,adv}\\ +\chi_{trail,b}\cos\theta_{b,adv}\end{pmatrix} \tag{2-3}$$

$$F_{lead,rec} = d\gamma_{LG}\begin{pmatrix}\chi_{lead,phob}\cos\theta_{phob,rec} + \chi_{lead,phil}\cos\theta_{phil,rec}\\ +\chi_{lead,b}\cos\theta_{b,rec}\end{pmatrix} \tag{2-4}$$

$$F_{trail,rec} = d\gamma_{LG}\begin{pmatrix}\chi_{trail,phob}\cos\theta_{phob,rec} + \chi_{trail,phil}\cos\theta_{phil,rec}\\ +\chi_{trail,b}\cos\theta_{b,rec}\end{pmatrix} \tag{2-5}$$

Force asymmetry occurs when $F_{asym,adv} = F_{lead,adv} + F_{trail,adv} \neq 0$ or $F_{asym,rec} = F_{lead,rec} + F_{trail,rec} \neq 0$, *i.e.*, when there is a non-zero net force while the contact line advances or recedes. Force hysteresis occurs when $F_{lead,adv} \neq F_{lead,rec}$ or $F_{trail,adv} \neq F_{trail,rec}$, *i.e.*, when

the forces during advancing and receding are not equal. Both asymmetry and hysteresis will typically occur on an ARC device. Force anisotropy occurs when $F_{an} = F_{asym,adv} + F_{asym,rec} \neq 0$; the droplet can be expected to move forward during each advancing/receding cycle if $F_{an} > 0$, and backward if $F_{an} < 0$. Due to the ARC design, the leading edge will pin along a hydrophobic rung while advancing ($\theta_{b,adv} = \theta_{phob,adv}$) and along a hydrophilic rung while receding ($\theta_{b,rec} = \theta_{phil,rec}$). The force asymmetry yields the following results:

$$F_{an} = F_{asym,adv} + F_{asym,rec} \tag{2-6}$$

F_{an} provides an indication on the expected movement of the droplet. For example, a larger positive value of F_{an} suggests a faster movement in the positive direction. Note that $F_{asym,adv}$ and $F_{asym,rec}$ assume pinning of the TPL on the ARC patterns and are therefore peak force values, which occur at different times in the voltage oscillation cycle. Therefore, F_{an} is useful as a design parameter but does not capture the complete dynamics of the droplet behavior, which would require the integration of the time-varying pinning forces along the TPL over the heterogeneous ARC surface.

To maximize the force anisotropy, the forward force $\chi_{trail,phil}$ should be as small as possible and $\chi_{trail,phob}$ should be as large as possible. In addition, the forward force increases with a larger difference between the hydrophilic and hydrophobic contact angles. As noted above, while the TPL moves across the ARC substrate, the χ values may vary with time. To simplify our analysis, we base the following calculations on the maximum forces that the ARC can exert on the droplet, which correspond to the maximum pinning of the TPL along the heterogeneous ARC pattern. The detailed force anisotropy derivation process is shown in Appendix B.

2.3 FABRICATION PROCESS

To create ARC surfaces, different material combinations with hydrophobic/hydrophilic behaviors can be applied. In our work, we used a perfluoro-octyltrichlorosilane (FOTS) – trimethylsilanol (TMS), self-assembled monolayer (SAM) system, and a Cytop - TMS spin-coated thin-film system. Table I summarized the material properties, including static contact angle (CA), dynamic CA hysteresis, sliding CA on an inclined surface, and coating thickness. The SAMs are created by chemisorption of the trichlorosilane "headgroups" with the hydroxyl group on the substrate forming a stable covalent bond. The functional "tail group" can be altered providing different surface energies to create hydrophobic/hydrophilic contrast. The FOTS "tail group" is highly fluorinated thus it can provide the hydrophobic surface finish. The deposition process can be either in the vapor phase or in solution. The SAM coating is thick on the molecular level, making the coating transparent and optically flat.

Cytop is an amorphous fluoropolymer with good transparency over the visible and UV wavelength range, good solubility in the solvent to coat, and excellent water repellent property. The refractive index of Cytop is 1.34, which can serve as an anti-reflective coating on glass substrates. Micropatterning on hydrophobic surfaces (like Teflon, Cytop) is difficult using standard photolithography due to poor adhesion between the photoresist and Cytop. Methods have been proposed using a metal buffer layer [149, 150] or plasma pretreatment of the surface, but the original surface properties will be damaged after treatment with decreasing water droplet contact angle. Poly (p-xylylene) polymers are a special series of polymers with the chemical vapor deposition process to form uniform pin-hole free films. Parylene C can be etched with oxygen plasma, making it compatible with standard lithography processes. It has been used to create biomolecular stencil arrays [151] and patterns on soft substrates [152]. By adopting Parylene C as

a stencil mask, we created hydrophilic patterns on top of the Cytop surface without degrading the original surface properties.

2.3.1 *FOTS-TMS Self-assembly Monolayer System*

The fabrication process flow for the FOTS-TMS system is shown in Fig. 2.2 (a). A silicon wafer was first cleaned with a piranha solution at 110 °C for 10 min, rinsed with deionized (DI) water and dried with nitrogen gas using a Spin Rinse Dryer (ClassOne Technology, Inc.). The wafer was then put into the priming oven and treated with hexamethyldisilazane (HMDS) vapor at 150 °C, forming a TMS self-assembled monolayer on the silicon oxide. 1.2 μm photoresist AZ1512 was spin-coated on the wafer surface and the ARC pattern was directly exposed with a Heidelberg-MicroPG-101 mask writer (Heidelberg Instruments Mikrotechnik GmbH). The wafer was developed with AZ340 photoresist developer (AZ340: DI water = 4:1) and treated with oxygen plasma for 1 min at 50 W in a barrel asher (Glow Research) to etch away the exposed TMS layer. The wafer was immersed in FOTS vapor inside the vacuum chamber for 1 hour. Then the photoresist was washed away with acetone, isopropanol alcohol, and DI water before drying. Before testing, we annealed the wafer at 150 °C for 20 min. The fabrication is a one-mask process that minimizes the fabrication cost and turn-around time.

2.3.2 *Cytop-TMS Thin-film System*

To fabricate the Cytop-TMS thin film surfaces (shown in Fig. 2.2 (b)), a silicon wafer was first cleaned with piranha solution at 110 °C for 10 min, rinsed with deionized (DI) water and dried with nitrogen gas using a spin rinse dryer (ClassOne Technology). After Si/glass wafer cleaning, diluted Cytop (Cytop CTL-809M : CTL-Solv.180 = 3:1) was spin-coated on a silicon wafer and baked under 110 °C for 20 minutes followed by 1-hour baking at 200 °C. Then 2.5 μm Parylene

C was evaporated on the Cytop using a commercial parylene coater (PDS 2010, Specialty Coating Systems) under vacuum. 6 μm photoresist (AZ9620) was coated and patterned with the Heidelberg mask writer. The Parylene C stencil mask and Cytop were etched through with O_2 plasma using reactive ion etching (Vision RIE). Then the Parylene C stencil mask was peeled off with tweezers. The surface was treated with spin-on TMS (MicroPrime MP-P20) and baked at 110 °C for 2 min.

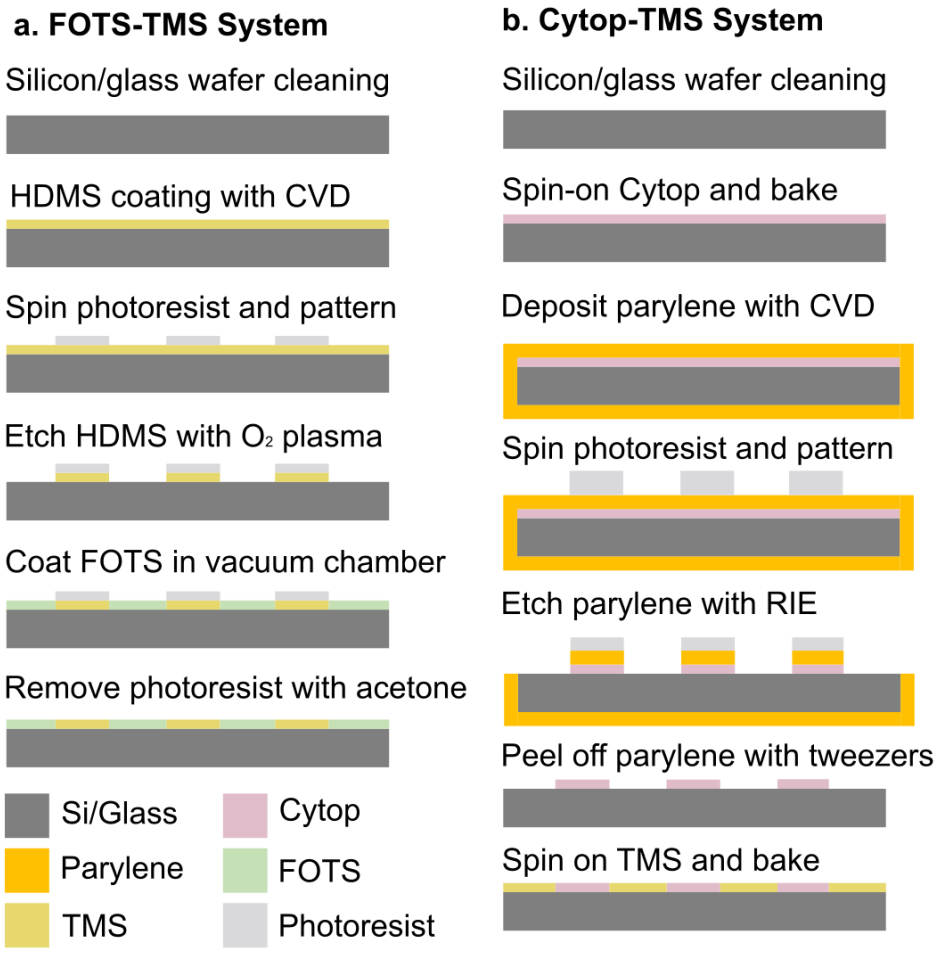

Figure 2.2. (a) The fabrication process of the FOTS-TMS system. (b) The fabrication process of the Cytop-TMS system.

2.4 EXPERIMENT SETUP

2.4.1 *Droplet Transport Vibrational Stage*

The testbench setup is shown in Fig. 2.3 (a). The test wafer was mounted on an aluminum platform, which is attached to the vibration exciter (Brüel and Kjær type 4809) with double-sided adhesive tape. A sinusoidal wave signal was generated by the function generator and amplified by the power amplifier to drive the vibration exciter (Brüel and Kjær type 2718). The vibration amplitude was monitored with the vibrometer (Polytec OFV) with an oscilloscope (Agilent Infiniium). The water droplet movement was captured by a high-speed camera (FASTCAM Mini UX100) at 1000 fps. The image was processed with MATLAB custom code to generate the position and contact angle change of the droplet leading and trailing edges with time. The conversion between the droplet width and pixel size was calibrated with a standard calibration bead with a diameter of 3 mm.

2.4.2 *Light Transmittance and Solar Power Monitoring*

Light transmission data of the two ARC surface coatings on a soda-lime glass substrate was recorded with a Cary 5000 UV-Vis-NIR spectrophotometer (Agilent Technologies, Inc.). A self-customized source meter was used for the I-V curve output of the solar modules, shown in Fig. 2.3 (b). We used an Arduino Nano development board, which was based on the ATmega328P microcontroller. The board was powered by a Mini-B USB and had 14 digital pins as input or output. 8 analog pins were configured as analog voltage reading input, with 10-bits of resolution. We used an MCP4822 dual-channel Digital-to-Analog (DAC) chip to create voltage bias on the solar modules. We configured TLV4110 high current operational amplifiers as a voltage follower and the op-amp can handle up to 500 mV output current. A 1 Ω resistor was used as the current sensing resistor. As the current monitoring part, we used an AD8210 current monitor chip. The

whole system was designed to use a single power supply, so an AD780 high precision reference was configured at 2.5V as the DC shift from the ground. The Arduino took voltage output from the current sensing chip and converts the analog data to digital through the 10-bit resolution analog port. The whole circuit system is powered by the external power source since the power output at the Arduino development board is noisy and has low current output capability. The system is calibrated with resistive load. The schematic and layout of the I-V curve testbench circuit before component soldering is shown in Fig. 2.4.

2.4.3 *Contact Angle and Sliding Angle Measurement Setup*

Both water droplet static contact angle (CA) and dynamic contact angle measurements on uniform coated FOTS and Cytop surfaces were measured with Krüss Drop Shape Analyzer (DSA 100). For dynamic contact angle measurement, the water dispensing and retreating speed was at 10 μL/s with a total volume of 30 μL. For the droplet sliding angle measurement, a self-customized experiment setup was designed, shown in Fig. 2.3 (c). The testing wafer was mounted on an acrylic tilting stage with one end at the tip of another lifting stage while the other end was fixed by hinges. A 3-axis accelerometer (MMA8451 from Adafruit) was attached to the end of the acrylic tilting stage. The accelerometer output was communicated with an Arduino microcontroller through I2C communication pins. The inclination angle can be derived from the acceleration output of the x, y, z-axis [153]. The ARC track radius of curvature pointing either upward or downward was tested by applying a droplet on the measurement ARC track and observing the tilting angle while the droplet started to slide off the surface by gravity.

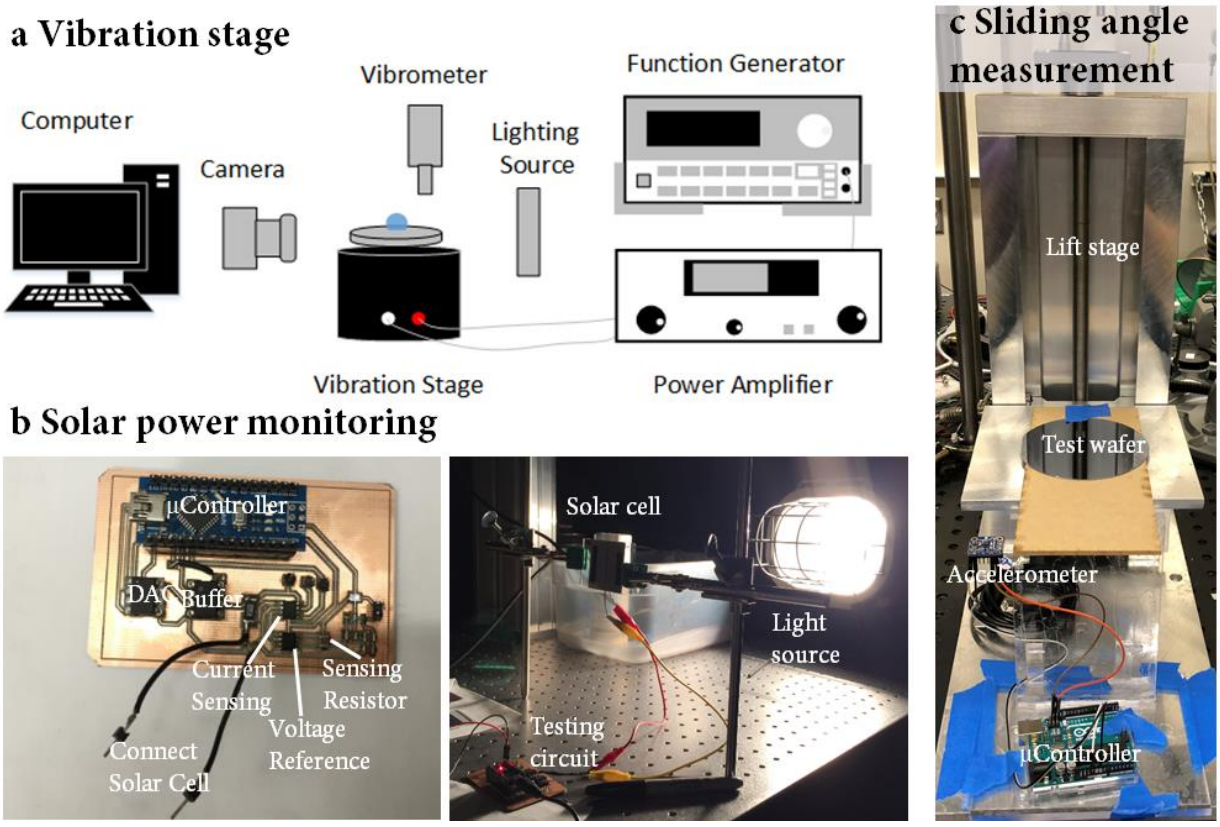

Figure 2.3. (a) Diagram of the vibration stage experimental setup. (b) Self-customized inclination angle measurement setup. (c) PCB circuit of the source meter design and I-V curve measurement testing setup.

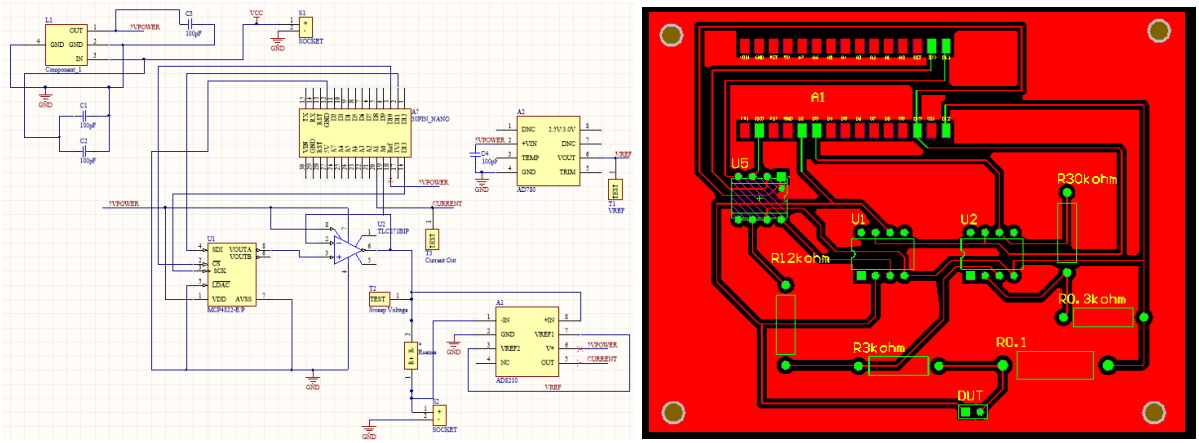

Figure 2.4. (a) Schematic design of the source meter. (b) Layout design of the source meter.

2.5 CHARACTERIZATION RESULTS

2.5.1 *Patterned Cytop Surface Properties*

The characterization results of the surface properties of the coating materials are shown in Table 2.1. The patterned Cytop after etching and peeling off the Parylene C shadow mask is shown in Fig. 2.5. The ARC patterns were successfully patterned on Cytop thin film with smooth edges. To characterize the Cytop surface properties, we measured both static contact angle (CA) and dynamic sliding angle (SA) on the as-deposited Cytop surface and after the Parylene C etching process. 15 μL droplets were used for SA tests. Each analysis result was generated from 3 water droplets at different substrate locations. As evident from the results shown in Fig. 2.6, Cytop maintained its hydrophobic surface properties with high CA and low SA after peeling off the patterned Parylene C stencil mask. The measured Cytop CA after Parylene C peeling off is higher than the sacrificial layer methods by using SiO_2 e-beam evaporation to pattern Cytop [154].

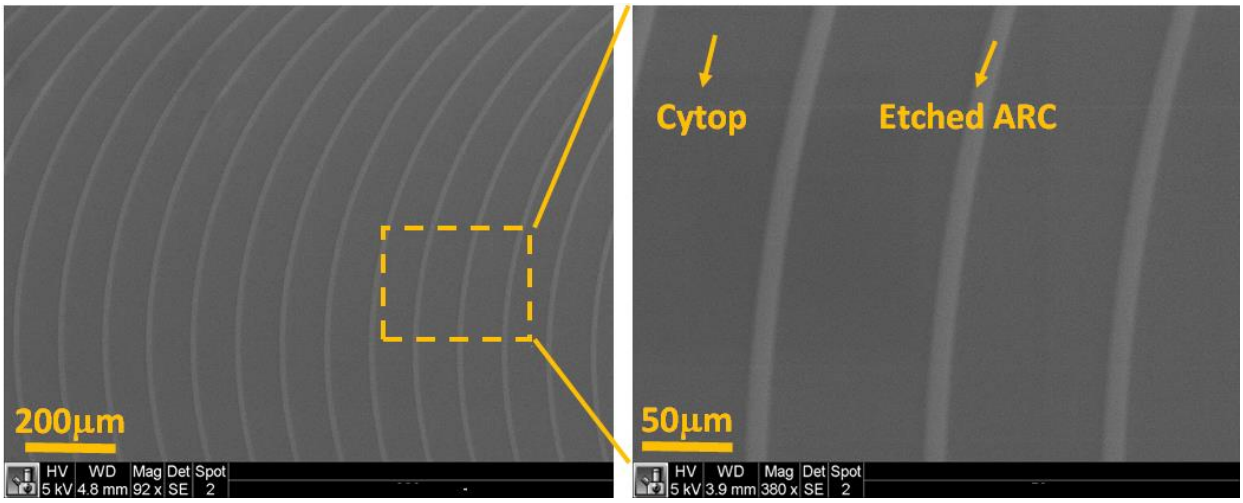

Figure 2.5 SEM images of ARC patterns on Cytop. For each curved rung, the radius of curvature (R) is 1000 μm, the etched linewidth (w) is 10 μm, and the period (P) between adjacent rung centers is 100 μm.

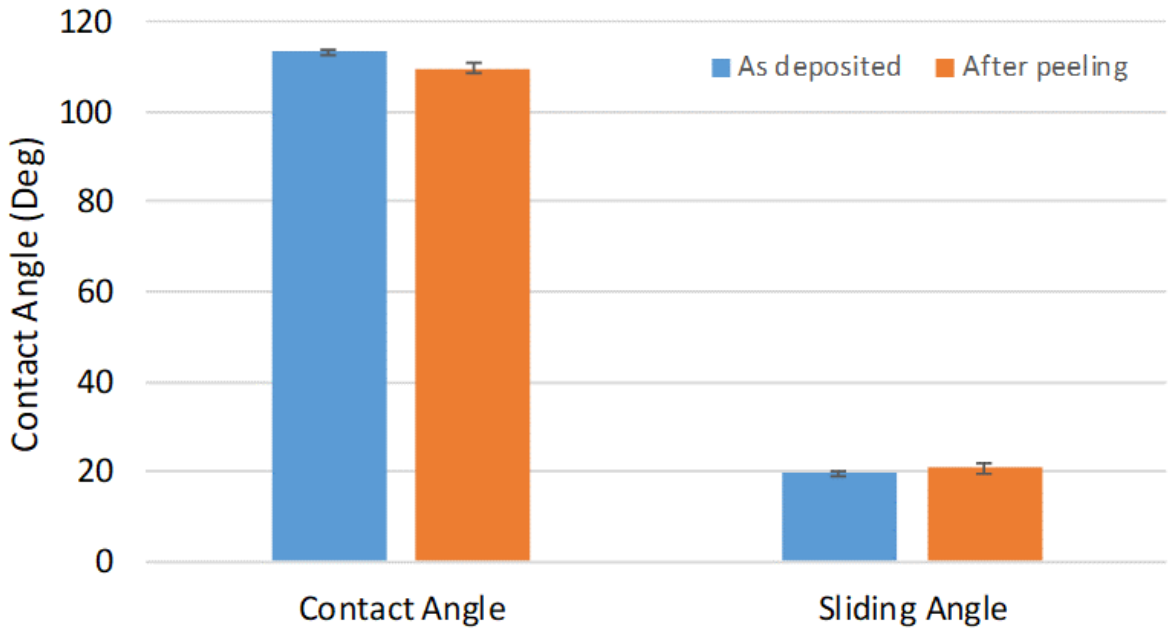

Figure 2.6. Contact angle and sliding measurement results of Cytop surface as-deposited and after peeling off Parylene C.

Table 2.1. Summary of coating materials surface property characterization results

Material	Cytop	FOTS	TMS
Static CA (°)	110	108	75
Advancing CA (°)	115	117	79
Receding CA (°)	101	88	64
Hysteresis (°)	14	29	15
Sliding Angle (°)	22	77	22
Thickness (nm)	70	molecular-level thick	molecular-level thick

Sliding angles were measured with 15 μL water droplets on a polished silicon wafer substrate. Cytop thickness was measured with a stylus profilometer.

2.5.2 *Droplet Transport*

The test wafer with ARC patterns was mounted on a vibration stage. A 10 μL (2.84 mm in diameter) water droplet was pipetted on the surface and the droplet silhouette was monitored via high-speed camera, with a frame rate of 1000 fps. We tested both FOTS-TMS and Cytop-TMS systems, with the design parameters of R = 1000 μm, P = 100 μm, w = 10 μm, and W = 1.8 mm. Fig. 2.7 (a) and Fig. 2.7 (b) show a typical droplet leading and trailing position change, contact angle change and line speed with time as the substrate vibrated orthogonally. The droplet transport speed was 7.5 mm/s on the FOTS-TMS ARC surface and 27 mm/s on the Cytop-TMS ARC surface. In this design, we translated substrate orthogonal vibration into droplet lateral expansion and recession, and thus moved the droplet by the anisotropic forces at the leading and trailing edge where the solid-liquid-gas three-phase contact line resided.

The droplet transport speed can be estimated as [148]:

$$v = n_{\mathrm{ARC}}\, P\, f \tag{2-9}$$

where n_{ARC} is the number of ARC rungs in which the droplet advances during each vibration cycle and f is the vibration frequency. The dynamic movement of the three-phase contact line across the discrete surface pattern of our ARC is a complex interaction, which makes it difficult to derive a predictive model for n_{ARC}. Empirically, the number of rungs the droplet advances during each vibration cycle varies depending on the vibration amplitude, frequency, and surface coating properties [155]. For a particular droplet transport situation of Cytop-TMS system (Fig. 2.8 (b)), the leading edge expanded on average by 0.73 mm and recessed on average by 0.23 mm during a single vibration cycle, compared with 0.39 mm of expansion and 0.89 mm of recession for the trailing edge. Taking the period P = 100 μm into consideration, the leading edge covered about 7

rungs during the expansion phase and 2 rungs during the recession phase, with a net rung advancement of $n_{ARC} = 5$.

With the aid of ARC, the droplet can overcome the force of gravity and climb on the inclined surfaces under orthogonal vibration. We fabricated the inclined mounting surface with a 3D printer using PLA plastics. The minimum vibration acceleration required to move the droplet along single ARCs at frequencies 20~100 Hz was experimentally determined at different inclination angles, shown in Fig. 2.8 (a). Fig. 2.8 (b) shows the water droplet movement uphill on the 15° inclination surface. With higher inclination angles, the droplet tended to be "shaken-off" from the surface.

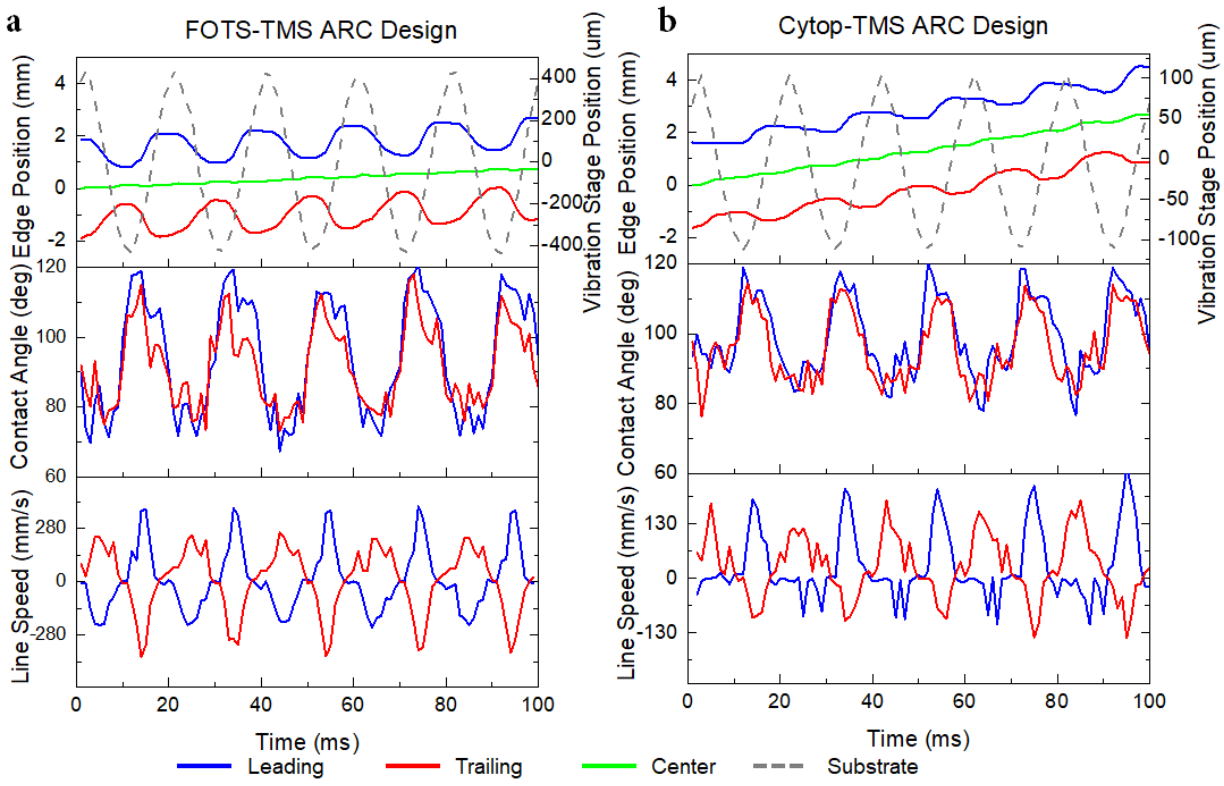

Figure 2.7. Droplet leading and trailing edge position, contact angle, line spreading speed change with time. We define line speed as the derivative of the droplet edge position over time. (a) FOTS-TMS ARC design. The vibration acceleration is 4.1 g at 50 Hz. (b) Cytop-TMS ARC design. The vibration acceleration is 1.1 g at 50 Hz. g = 9.8 m/s^2.

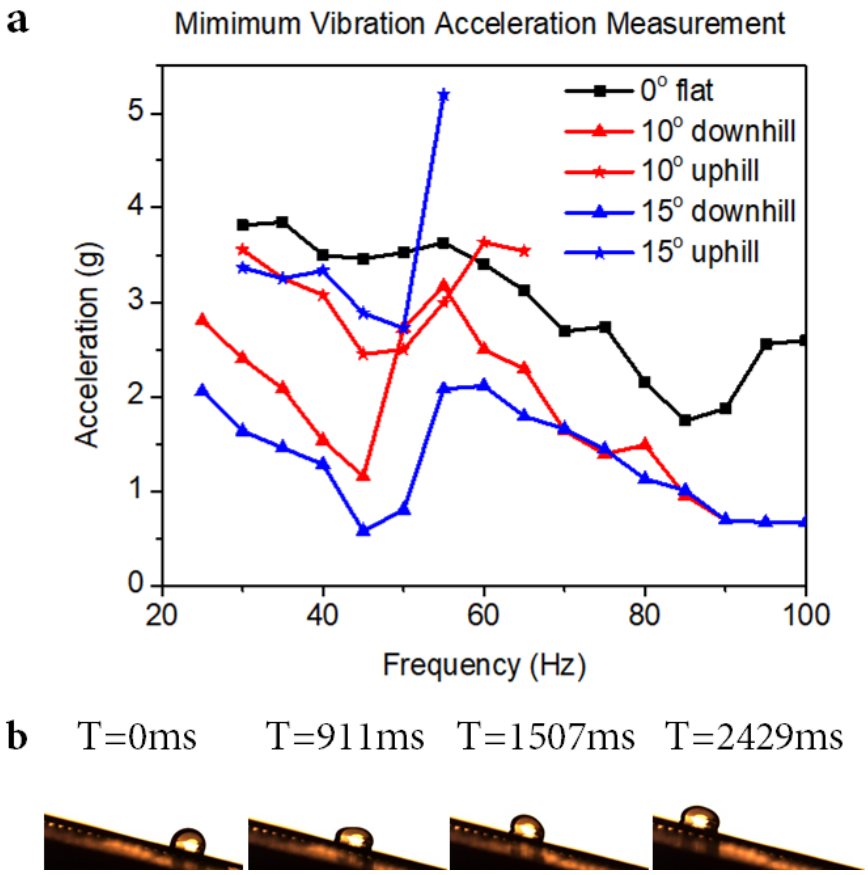

Figure 2.8. (a) Minimum acceleration requirement for a 7 µL droplet to move on flat and inclined surfaces fabricated with the FOTS-TMS self-assembly system. The droplet can move uphill or downhill depending on the direction of the ARC rung structure. (b) Droplet transport along the inclined surfaces

2.5.3 *The Frequency Response*

It is important to understand the frequency response of the droplet and to match it with the dynamic behavior of the PV modules [156]. The water droplet exhibits different resonance modes depending on mass and surface tension, which has been researched by X. Noblin *et al*. [157], J. Sharp *et al*. [158], and S. Mettu *et al*. [159]. To estimate the droplet resonance mode, we consider the standing capillary waves existing around the surface of the droplet. The dispersion relationship for the gravity-capillary waves can be expressed as [160]:

$$\omega^2 = gk + \gamma k^3/\rho \tag{2-10}$$

where ω is the angular frequency, θ equals the contact angle, γ is the surface tension, g is the gravity constant, k is the wave vector, and is ρ the density of the fluid. For short waves, the effect of gravity can be neglected. Then the capillary wave can be expressed using:

$$\omega^2 = \frac{\gamma k^3}{\rho} = \frac{\gamma}{\rho}\left(\frac{2\pi}{\lambda}\right)^3 \tag{2-11}$$

where λ is the capillary wavelength. As shown in Fig. 2.9, if we consider only a cross-section of the droplet, then the profile length is defined as the arc length at the liquid-air boundaries [161]. Along the profile length, there exist half integers of wavelength, then:

$$l = R \cdot 2\theta = \frac{n\lambda}{2} \tag{2-12}$$

n=2,3,4,… is the mode number. If we assume that the shape of the droplet resting on the surface is a spherical cap, the volume of the spherical cap can be expressed as:

$$V = \frac{m}{\rho} = \int_{R-h}^{R} \pi(R^2 - y^2)dy = \frac{\pi R^3}{3}(\cos^3\theta - 3\cos\theta + 2) \tag{2-13}$$

Combining equations 2-10, 2-11, 2-12, and 2-13, the expression of the n^{th} resonance mode of the droplet can be expressed as:

$$f_n^2 = \frac{\pi}{2}\left(\frac{n^3\gamma}{24m}\frac{cos^3\theta - 3\cos\theta + 2}{\theta^3}\right)^{\frac{1}{2}} \tag{2-14}$$

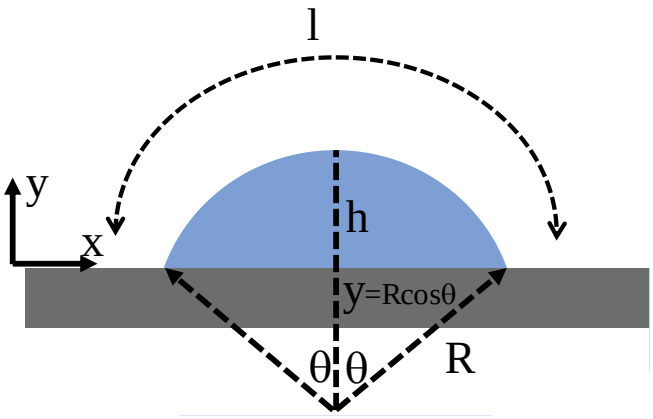

Figure 2.9. Diagram of the droplet on a surface. The droplet is estimated as a spherical cap.

We modeled the droplet on the uniform hydrophobic surface under vibration as a forced mass-spring oscillator system [162] and then characterized the water drop resonance frequency in low-frequency bandwidth regions (10 – 100 Hz, at every 5 Hz) by monitoring the droplet width change at different vibration frequencies. The vibration acceleration was kept constant at 1 g, meaning the droplet was driven by a periodic external force. Fig. 2.10 (a) shows the plot of relative droplet width change of 5 μL, 10 μL, and 15 μL droplets at different frequencies. Due to the mechanical resonance behavior of the droplet, it was relatively easy to drive the center volume of the droplet on the substrate using frequencies close to its resonance, when relatively low orthogonal vibration energy was required to achieve enough droplet sideway expansion amplitude. Fig. 2.10 (b) shows examples of the droplet transport with higher modes on ARC surfaces at 50 Hz, 200 Hz, 300 Hz, and 500 Hz. The acceleration required to move the water droplet along the ARC rises as the mode number increases.

To study the required power input to drive the droplet, if we ignore the mass of the substrate, we have the following expression describing a damped oscillator with a harmonic driving force [163]:

$$\frac{d^2}{dt^2}x(t) + \Gamma\frac{d}{dt}x(t) + \omega_0^2 x(t) = \frac{F_0\cos(\omega_d t)}{m} \tag{2-15}$$

where $x(t)$ is droplet position with time, Γ is the damping constant of the electromagnetic vibration exciter (in s^{-1}), F_0 is the driven force, $\omega_0/2\pi$ is the natural frequency of the oscillator and $\omega_d/2\pi$ is the driven frequency. The solution to the equation above is:

$$x(t) = A\cos(\omega_d t) + B\sin(\omega_d t) \tag{2-16}$$

$$A = \frac{(\omega_0^2-\omega_d^2)a}{(\omega_0^2-\omega_d^2)^2+\Gamma^2\omega_d^2} \tag{2-17}$$

$$B = \frac{\Gamma\omega_d a}{(\omega_0^2-\omega_d^2)^2+\Gamma^2\omega_d^2} \quad (2\text{-}18)$$

where A is the elastic amplitude and B is the absorptive amplitude. $a = \frac{F_0}{m}$, can be measured from experiments. The average power within any single oscillation period is related to the *B* term:

$$\langle P\rangle = \frac{1}{T}\int_0^T F\frac{dx}{dt}dt = \frac{1}{2}F_0\omega_d B = \frac{1}{2}ma\omega_d B \quad (2\text{-}19)$$

To estimate the power required to drive the droplet, we measured the minimum acceleration required to drive the droplet over the 20~100 Hz frequency bandwidth, shown in Fig. 2.11 (c). We then calculated the average power based on equation (2-19). All the parameters could be inserted through measurement or datasheet, except for the damping coefficient of the electromagnetic vibration exciter. All the parameters could be inserted through measurement or datasheet, except for the damping coefficient of the electromagnetic vibration exciter. We estimated a large damping coefficient $\Gamma = 1000\ s^{-1}$ in our calculation based on the fact that the electromagnetic vibration exciter was a highly damped system and the conversion efficiency from electrical to mechanical was low at its maximum load (~0.1%) among the working frequencies [164]. The power calculations based on experimentally measured data on Cytop-TMS ARC designs are presented in the demo section below.

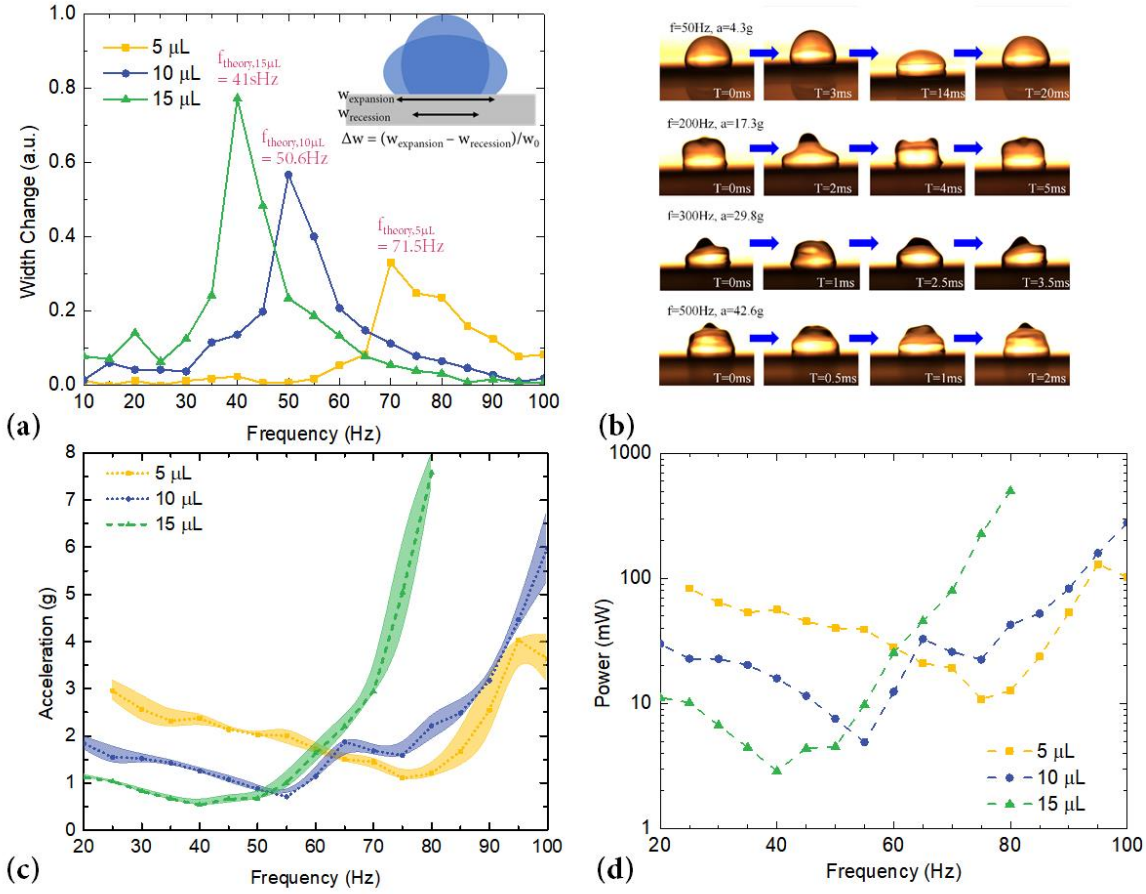

Figure 2.10. (a) The frequency response of water droplets with different volumes on Cytop surfaces under the same vibration acceleration input of 1 g. The initial droplet width w_0 on the Cytop surface was measured as 2.24 mm, 2.87 mm, 3.39 mm separately by image processing. (b) Water droplet (7 μL) transport modes under different frequencies. The ARC track requires vibration input with higher accelerations to drive the water droplet forward as the frequency increases. (c) Minimum vibration acceleration map required to transport the droplet. Three droplets were measured at each frequency point. Data is shown ± one standard deviation for n = 3. (d) Estimated power consumption of the electromagnetic shaker. The overall load weight was measured at 200 grams. The spring constant of the system is 12 N/mm according to the instrument datasheet.

2.5.4 *Surface Anisotropic Force by Sliding Angle Measurement*

To evaluate the anisotropic forces, a slip test was performed with different ARC designs (Fig. 2.11). The inclination angle is defined when the droplet started to slide off the tilted surfaces. The gravity of the water droplet overcomes the surface adhesion at the inclination angle. The ARC radius of curvature is pointed either uphill or downhill on inclined surfaces, indicated in Fig 2.11. The anisotropic pinning force can be expressed as:

$$F_{anis} = F_{slip,uphill} - F_{slip,downhill} = mg \sin \delta_{uphill} - mg \sin \delta_{downhill} \qquad (2\text{-}20)$$

where δ is the surface inclination angle. We performed a slip test on the Cytop-TMS ARC surface. For the (a1) - (a3) design group, we changed the center-to-center period width (*P*) with 50 μm, 100 μm, and 200 μm while keeping other parameters the same. For the (b1) - (b4) design group, we altered the ARC pattern radius of curvature (*R*) with 1000 μm, 1100 μm, 1500 μm, and straight lines. From the results of the change in period (a1) - (a3), the sliding angle for both uphill and downhill decreases as the period gap increases. The anisotropic forces remained similar for different designs. However, we could observe a decrease of the anisotropic force as we increased the ARC radius of curvature from the measurement results of (b1) - (b4). The average anisotropic force on a radius of curvature *R* = 1000 μm, 1100 μm, 1500 μm was 73 μN, 66 μN, and 11 μN, respectively. When there were only straight hydrophilic lines, no sliding angle differences were observed for uphill and downhill measurements and the anisotropic forces were close to zero. To achieve a better ratcheting performance, we chose the ARC radius of curvature *R* = 1000 μm to drive the droplet to move.

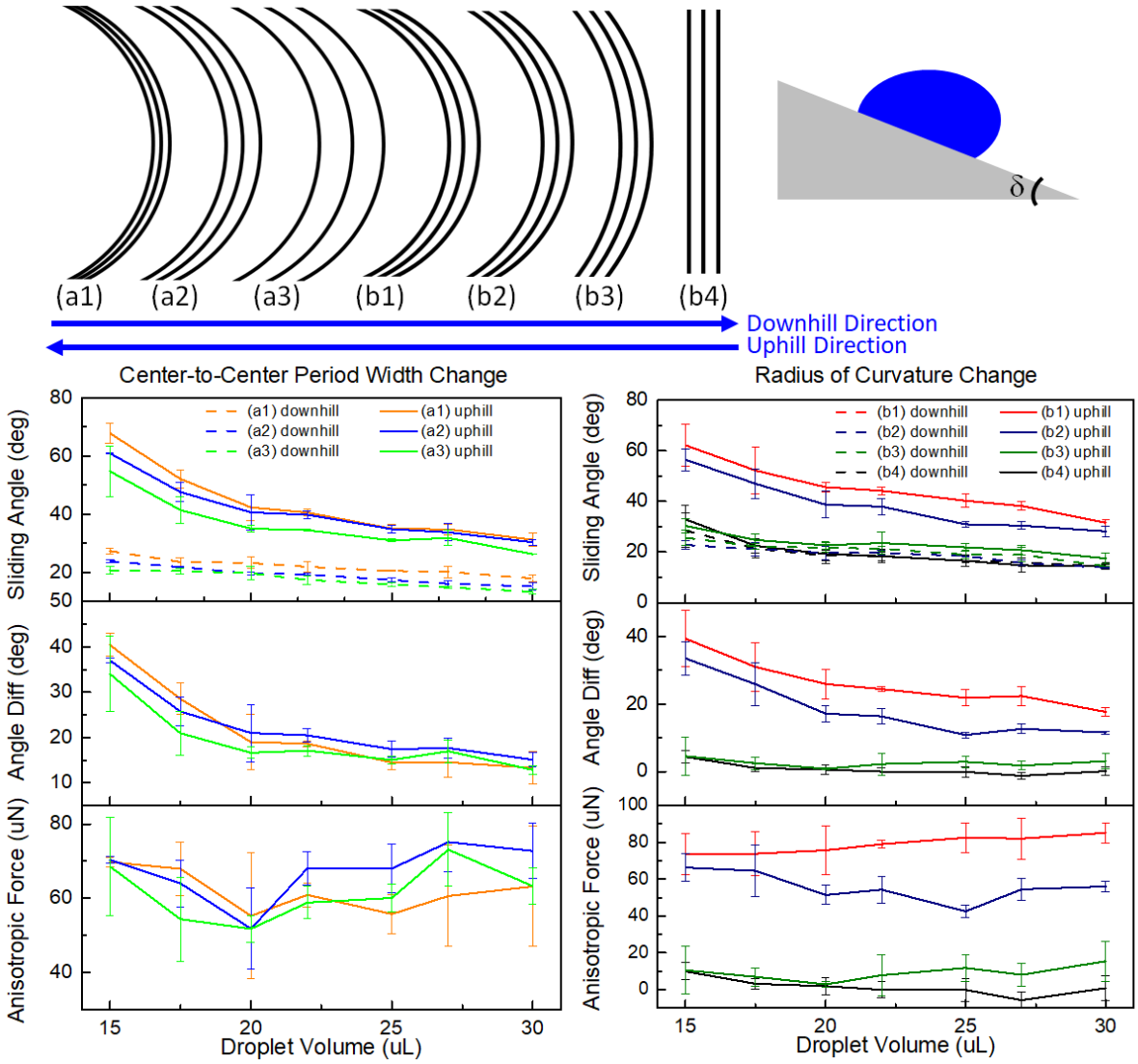

Figure 2.11. (a) The frequency response of water droplets with different volumes on Cytop surfaces under the same vibration acceleration input of 1 g. The initial droplet width w_0 on the Cytop surface was measured as 2.24 mm, 2.87 mm, 3.39 mm separately by image processing. (b) Water droplet (7 µL) transport modes under different frequencies. The ARC track requires vibration input with higher accelerations to drive the water droplet forward as the frequency increases. (c) Minimum vibration acceleration map required to transport the droplet. Three droplets were measured at each frequency point. Data is shown ± one standard deviation for n = 3. (d) Estimated power consumption of the electromagnetic shaker. The overall load weight was measured at 200 grams. The spring constant of the system is 12 N/mm according to the instrument datasheet.

2.5.5 *Dust Particle Adhesion Force and Water Droplet Cleaning Force*

Several parameters influence the surface interactions between the dust particles and the surfaces they deposit on, including particle material characteristics, environment conditions (relative humidity and temperature), surface roughness, and treatments [165]. Theoretical conceptualization of the particle mobilization caused by the advancing and receding of the three-phase contact line (TPL) is based on the analysis of the major forces acting on the dust particles. The forces majorly include adhesion forces and detachment forces (surface tension force and hydrodynamic force). For small dust particles (diameter < 500 μm), the adhesion forces mainly come from the van der Waals force and the electrostatic force in dry environments, as well as the capillary force in humid environments [146, 166]. The adhesion force for a single particle on a surface can be in the range of 100~300 nN, characterized by an AFM tip [146].

As a droplet is applied on the contaminated surface and transported under vibration, dust particles will be removed from the surface by the droplet, demonstrating the dominance of detachment forces over adhesion forces. There are two main sources of detachment force: capillary force and hydrodynamic shear force.

When a water-air interface comes in contact with dust particles, shown in Fig. 2.12 (a) and (b), the capillary force at the interface can be expressed as :

$$F_\gamma = 2\pi R\gamma \sin\phi \sin(\theta - \phi) \tag{2-21}$$

where γ is the water/air surface tension (72 mN/m at 25 °C), R is the radius of the spherical dust particle, θ is the contact angle between the water and the dust particle, and ϕ is the filling angle describing the position of the water/air interface on the particle surfaces. We have the maximum capillary force on vertical and horizontal directions [165] when $\phi = \frac{\theta}{2}$.

$$F^z_{\gamma,\max} = 2\pi R\gamma \sin^2\frac{\phi}{2}\cos\alpha \tag{2-22}$$

$$F_{\gamma,\max}^{x} = 2\pi R\gamma \sin^2\frac{\phi}{2}\sin\alpha \quad (2\text{-}23)$$

where α is the contact angle between water and the substrate. Since the particle sizes are small, the buoyancy force and the gravity force are negligible. As the droplet is being actively agitated by vibration, the dust particles are cleaned up by the advancing and receding of the water-air interfaces. The dust particles will be brought inside of the water droplet due to the internal circulating flow of the vibrating droplet [167].

Besides, the moving water/air interface exerts a hydrodynamic shear force on the particles. If the shape of the particle is spherical, then the maximum tangential shear force, which happens when the particle is completely exposed to the moving fluid, can be expressed as [168]:

$$F_s = 1.7\,(6\pi)\,\eta R_p v \quad (2\text{-}24)$$

where F_s is the shear force on the particle, η is the water dynamic viscosity (8.9×10^{-4} Pa·s) and v is the fluid water/air spreading speed.

To estimate the cleaning capillary and shear force, we assumed a droplet line speed at the order of 200 mm/s based on previous characterization results. The radius of the nitride particle was 200 μm with water/nitride contact angle 73° and water/Cytop contact angle 110°. Based on the theoretical calculation provided by equation (2-22) and (2-23), the surface tension forces were at the order of 10 μN in the vertical direction and 30 μN in the horizontal direction. For the maximum shear force from the droplet leading-edge expansion is at the order of 1 μN from equation (2-24). Compared with the adhesion force measurement results, the surface tension force and water hydrodynamic shear force were enough to remove the surface contaminants as the droplet moved onto the surface contaminants. Fig. 2.12 (c1)~(c4) demonstrates the cleaning process for particles (SiN_x powder) by a moving water droplet under the high-speed camera. Dust particles were dislodged by the surface tension force and the hydrodynamic force while encapsulated by the

internal flow of the vibrating droplet. The droplet was able to carry the SiN_x particles along. Similar phenomena could also be observed with carbon powder.

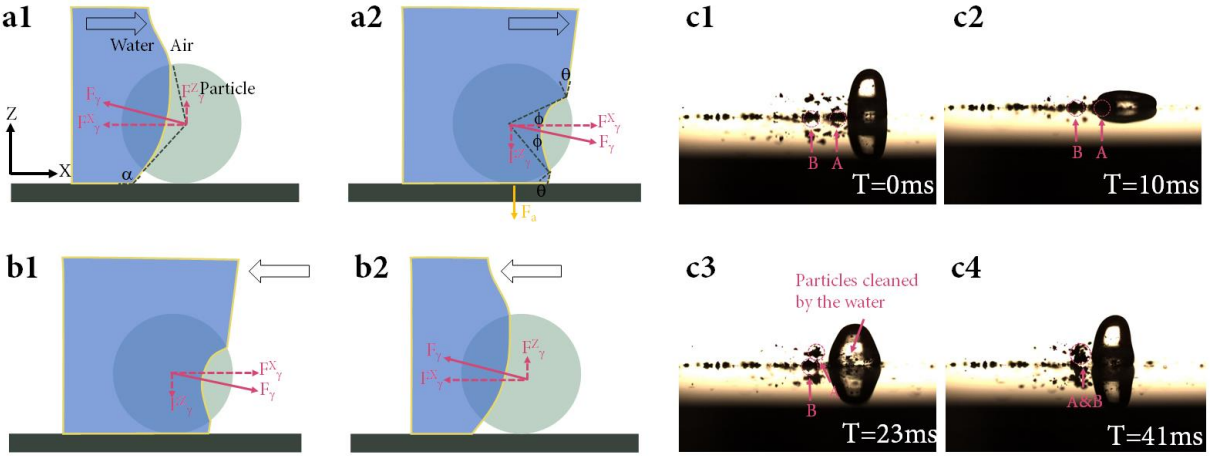

Figure 2.12. (a1) and (a2) show the direction of the surface tension force when the TPL is advancing to immerse the dust particles on the surface. (b1) and (b2) show the direction of the surface tension force when the TPL is receding away from the dust particles on the surface. (c1)~(c4) demonstrate how the bulk hydrophilic SiN_x powder is detached from the surface and relocated by the interfacial surface tension. When the droplet expands, the water-air interfacial force removes powder particles from point A to point B. Eventually, they will be trapped inside the droplet and carried away with the moving droplet.

2.6 Self-cleaning Surface Design: FOTS-TMS ARC Zig-zag Pattern

To create a surface cleaning system with a droplet, we designed a zig-zag pattern of the ARC, shown in Fig. 2.13. The droplet travels along the defined zig-zag pattern, looping around the cleaning area. We used a 10 μL droplet on an ARC track with 1.75 mm width and 1.5 mm edge-to-edge gap distance. The droplet footprint had overlapping areas while moving on the adjacent tracks to fully cover the surface. The total surface area is roughly 5.76 cm^2 (2.4 cm by 2.4 cm). At the corners, the droplet must abruptly change its velocity to the perpendicular moving direction. We iterated our designs and picked the design shown in Fig. 2.13 (b) by adjusting the relative

position of perpendicular tracks at the turning corner. Fig. 2.13 (c) represents subsequent video frames of the cleaning process of sugar sweetener on the surface. The water droplet was applied on the first loop at time T = 0 s and started the cleaning process. The vibration frequency was 50 Hz. At T = 12 s, a second droplet was applied on the second loop surface. All sweetener on the ARC areas was cleaned by the droplet. We observed a slowing motion of the droplet as it collected more sweetener that increased its mass and viscosity.

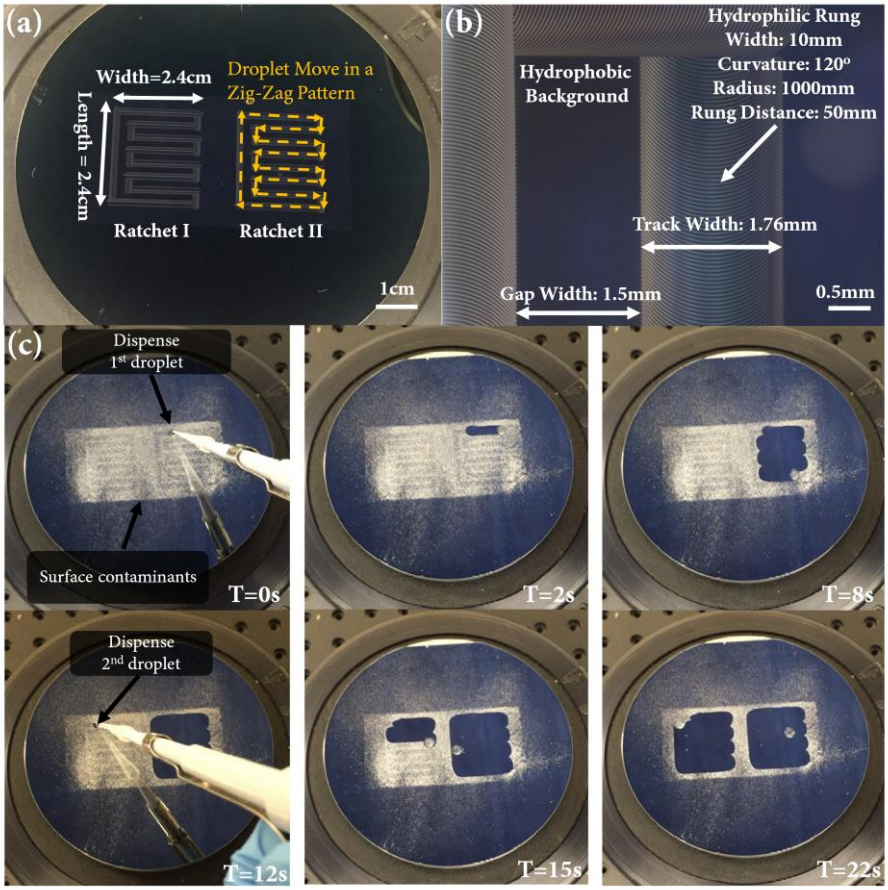

Figure 2.13. (a) Entire ARC track design after lithographic patterning. The droplet will follow the zig-zag pattern on each ratchet structure. The photoresist pattern will be removed after FOTS deposition, leaving only a transparent and optically flat monolayer surface. (b) ARC track at a corner showing the ratchet rung structure after lithographic patterning. (c) Surface cleaning performance for sweetener (dextrose, maltodextrin, and sucralose) contamination on the ARC surface consisting of two ARC tracks shown in (b).

2.7 Self-cleaning Surface Design: Cytop-TMS ARC Zig-zag Pattern

We then created a Cytop-TMS ARC on the soda-lime cover glass of an in-house assembled PV module. An a-Si solar cell was cut to 30 mm by 24 mm and glued between the cover glass and an acrylic substrate. Silicon nitride powder was applied (with a total mass of 10 mg) on the surface through a polyester mesh with a pore size of 250 μm. Shown in Fig. 2.14, a 13.5 μL droplet was pipetted atop and followed the zig-zag ARC track while cleaning the surface contaminants. The response of the solar module output efficiency was monitored in real-time with Arduino and Matlab. As the droplet picked up nitride particles, the solar output efficiency started to increase. we observed a 23 percentage-point gain by cleaning, from 69.1% after contamination to 92.1% after 15 s of cleaning. We observed particles bouncing on the solar cell surfaces from time to time that were captured as the droplet swept by. Due to the irregular motion of the dust particles bouncing on the vibrating surface, a longer cleaning process was anticipated to clean all the dust particles on top of the solar cell.

The total energy consumption by the vibration system is proportional to the cleaning time. In our case, the droplet cleaning time for a 30 mm by 24 mm area (720 mm^2) was T_{clean} = 15 seconds, as compared to an average sunshine time of T_{sun} = 8 hours for power generation by the solar modules during a single day. The polysilicon solar cell we used has an average power rating of ~0.16 mW/mm^2. We define P_1 as the power consumption for cleaning the system shown in Fig. 2.14 ($P_1 \approx 7$ mW, estimated from Fig. 2.10 (d)), P_2 as the power generation for a clean solar module ($P_2 \approx 0.147$ mW/mm^2) and P_3 as the power generation per surface area for a soiled solar module ($P_3 \approx 0.111$ mW/mm^2). Then we can calculate the energy gained due to cleaning as $(P_2 - P_3) \cdot T_{sun} \cdot 720\ mm^2 \approx 207\ mWh$, while the energy consumption due to cleaning is $P_1 \cdot T_{clean} \approx 0.03$ mWh. Even when considering the efficiency of only 0.1 % for the conversion from electrical

to mechanical power, the vibration system would only consume 30 mWh. This result indicates that we can substantially improve the overall daily solar output energy by keeping the surface clean with our self-cleaning system. To further reduce the system power consumption, a better vibration system should be designed to reach the minimum power consumption at the resonance frequency of the surface cleaning droplet.

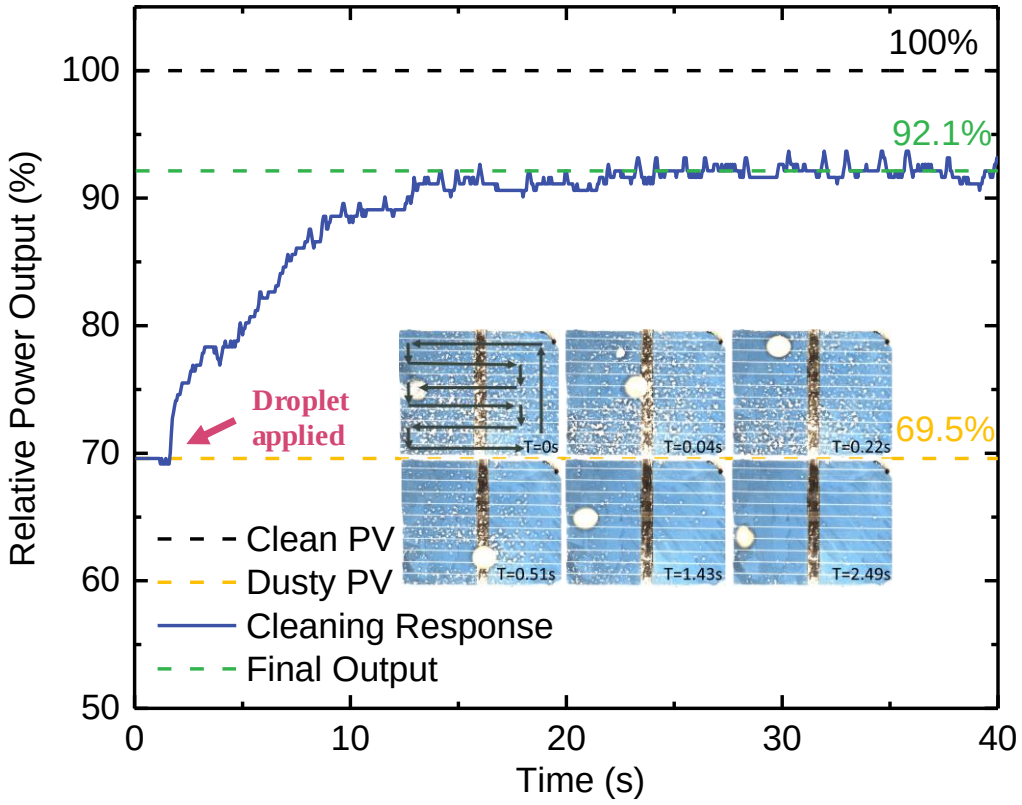

Figure 2.14. The real-time power output response of the solar module during the cleaning process. The solar module was connected to a resistive load for power monitoring. (insert) Top view of the cleaning process with continuous 3 cleaning cycles. The droplet is 13.5 μL in volume at a vibration frequency of 50 Hz. The droplet zig-zag path is shown at T=0 s with the red dotted line.

We tested the surface cleaning function with different categories of typical contamination, including dust and dirt particles, soluble and insoluble contaminations, summarized in Table 2.2.

Most water-soluble materials (like salt and sweetener) plus low surface adhesion insoluble particles (like sand, SiO_x, SiN_x, carbon powers) can be effectively cleaned with the droplet from the self-cleaning surface. Hydrophobic surface contaminants like polytetrafluoroethylene (PTFE) tended to stay at the boundary of the water droplet instead of being trapped inside the droplet. The droplet surface was gradually covered with solid powder so that the surface tension at the TPL was reduced. Eventually a "droplet marble" was formed jumping on the surface as agitated by vibration.

Table 2.2. Materials tested on the self-cleaning surface

Material	Sand (< 600 μm)	Salt*	Sweetener**	SiO_x and SiN_x	Carbon powder	PTFE
Can be cleaned or not	Y	Y	Y	Y	Y	N

*The salt is sodium chloride.

** The major contents of the sweetener are dextrose, maltodextrin, and sucralose.

2.8 CONCLUSIONS

In this chapter, we demonstrated a proof of concept self-cleaning surface system with ARC tracks using both FOTS-TMS and Cytop-TMS coatings. Cytop was successfully patterned using Parylene C as the stencil mask. Solar module optical transmission and solar cell power I-V measurements were performed, demonstrating the Cytop coating can provide antireflection properties on the soda-lime cover glass and improve solar output efficiency. Different surface contaminants including water-soluble, insoluble, hydrophobic, and hydrophilic dust particles were characterized. Our system relies on the surface tension anisotropy at the TPL of the droplet boundary to move the droplet along while dislodging and removing surface contaminants during droplet expansion and recession phases under vibration. Compared with hydrophobic surfaces

based on the lotus effect, our system has the advantage of systematically transporting the droplet to designated locations compared with uncontrolled droplet rolling by gravity on hydrophobic surfaces. The cleaning process only utilizes a sessile droplet with minimized water usage. The entire fabrication consists of a single-mask process to reduce manufacturing costs.

Chapter 3. SELF-CLEANING SURFACE AND LAB-ON-CHIP SYSTEM USING ELECTROWETTING-ON-DIELECTRIC

3.1 INTRODUCTION

Digital microfluidics (DMF) with water droplets provides a useful tool for many applications, including lab-on-chip platforms [169], bio/molecular diagnostics [170, 171], self-cleaning surfaces [126, 172], mass spectroscopy [173], and displays [174, 175]. Droplets are driven across the surface through anisotropy created by heat [176, 177], electrical field [178], chemical modification [179], vibration [180], *etc.* In DMF, discrete sample or reagent droplets have been manipulated by multiple platform functions such as transporting, merging, mixing, creating, and splitting.

Electrowetting-on-dielectric (EWOD) is a widely used technique to manipulate droplets [181]. A typical EWOD setup to characterize contact angle change is shown in Figure 3.1 (a). A water droplet is initially placed on a hydrophobic insulator surface. When a voltage is applied between the droplet and the electrode underneath, the electrostatic field will significantly modify the solid-liquid interfacial tension, leading to a reduction of contact angle and an improved wetting of the droplet on the solid surface. Depending on the application, two main EWOD configurations are often used, shown in Fig. 3.1 (b), the parallel-plate system, and 3.1 (c), the co-planar system. For the parallel-plate system, the water droplet was sandwiched in between the top and bottom electrodes, insulated by a dielectric layer (SU8, SiO_2 [120] or Parylene C [182]) and hydrophobic (Teflon^{TM} AF [183, 184] or Cytop® [185, 186] coatings. The electrode on one plate was patterned and the electrode on the other was fully grounded. The whole system can be placed in air or immersed in oil. When applying a voltage between the adjacent electrodes, the surface tension at the solid-liquid interface will be reduced due to the charge accumulation, and thus the droplet

contact angle on the energized surface will decrease dramatically becoming “hydrophilic”. The droplet will move to the “hydrophilic” side driven by the imbalanced surface tension force.

The parallel-plate system can prevent droplet evaporation and is less sensitive to gravity influence, compared with the co-planar system, where the cover plate is removed. In the parallel-plate system, full droplet manipulation functionality can be achieved including the possibility to generate and split droplets from a reservoir. Even low surface tension fluid can be possibly moved depending on its complex permittivity (together with lowering the gap distance between the two plates) [187]. Since the gap distance between the top and bottom plates is small, droplets with sizes in the nano-to-pico-liter range are often used. However, the co-planar system has broad applications and can be integrated into many other systems that do not permit a top cover plate [188]. For the parallel-plate system, the droplet is sandwiched in between the top and bottom electrodes. Patterned electrodes are on one plate and a single grounding electrode covered by hydrophobic coating is on the other plate. It is not easy to apply droplets manually to the parallel-plate system. For the coplanar-plate system, the droplets can be pipetted directly onto the electrodes for the next step operation. Larger droplet manipulation (μL size) is possible on the open coplanar DMF system.

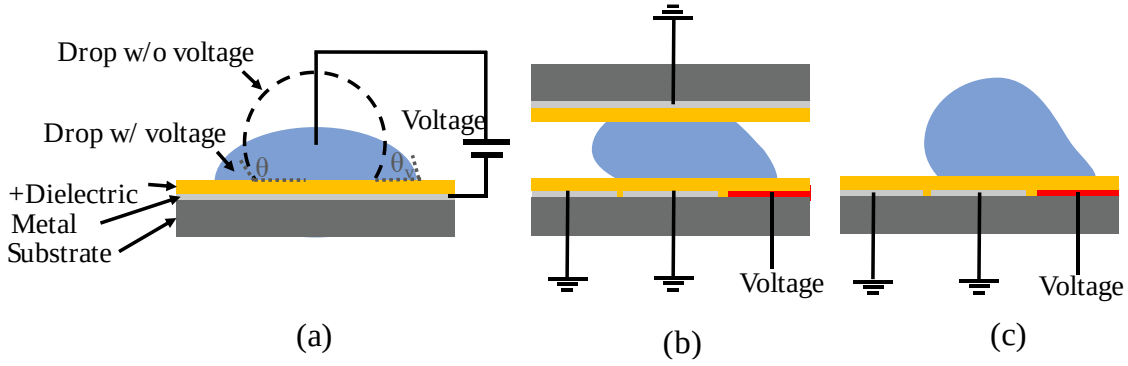

Figure 3.1. EWOD setup: (a) Typical EWOD setup to measure contact angle change by an external voltage. (b) Parallel-plate EWOD design to transport droplet. (c) Open coplanar EWOD design. The energized electrodes are marked as red color in (b) and (c).

When an external electrical field is applied, both of γ_{SG} and γ_{LG} remain approximately unchanged [189]. γ_{SL} can be assumed to be composed of a chemical component (electrical potential independent) and an electrical potential dependent part, which is expressed as [189-191]:

$$\gamma_{SL(V)} = \gamma_{SL} + \gamma_{SL}^{el} = \gamma_{SL} - \frac{1}{2}CV^2 \tag{3-1}$$

where $\gamma_{SL(V)}$ is the solid-liquid surface tension under external electrical voltage, γ_{SL}^{el} is the electrical potential dependent part, and C is the capacitance of the dielectric layer per area (measured in F/m^2).

Combined with Young's equation, we can derive the Young-Lippman equation as:

$$\cos(\theta_v) = \frac{\gamma_{SG} - \gamma_{SL(V)}}{\gamma_{LG}} = \frac{\gamma_{SG} - \gamma_{SL}}{\gamma_{LG}} + \frac{CV^2}{2\gamma_{LG}} = \cos(\theta) + \frac{CV^2}{2\gamma_{LG}} \tag{3-2}$$

The Young-Lippman equation can also be written as:

$$\gamma_{LG}\cos(\theta_v) = \frac{CV^2}{2} + \gamma_{LG}\cos(\theta) \tag{3-3}$$

where $\frac{CV^2}{2}$ is the electrowetting force per unit length f_{EWOD}, $\gamma_{LG}\cos(\theta)$ is the capillary force per unit length f_{CAP} and $\gamma_{LG}\cos(\theta_v)$ is the total force or electrocapillary force per unit length f_{TOT} (all measured in N/m), showing that the effect of electrowetting is to add electrowetting force on top of the capillary force on the three-phase contact line. Fig. 3.2 shows a top view of the droplet transported on the electrodes. The electrocapillary force along the x-axis, which is the driven force to move the droplet, can be integrated by [192]:

$$F_x = \int_L f_{TOT}\,\vec{n}\,\vec{\imath}\,dl = d\,f_{TOT} \tag{3-4}$$

The force is independent of the three-phase contact line shape and only relates to the electrode width. The force remains constant during the motion when the droplet moves along the two electrodes. The friction force for the droplet to transport at steady-state includes the viscous flow within the droplet, the viscous effect between the droplet and the medium, as well as the friction around the three-phase contact line [193]. The power consumption for the EWOD devices can be

at the order of hundreds of nW due to the capacitance effect. The EWOD system can be a power-efficient choice for many applications.

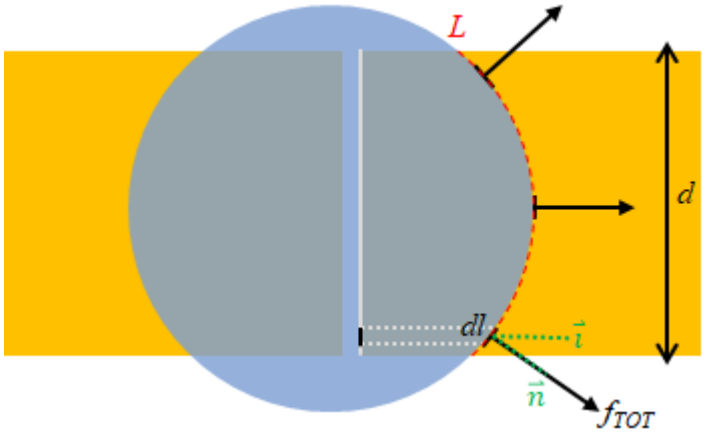

Figure 3.2. Top view of the droplet sitting between the two electrodes. The right electrode is turned on and the droplet will be driven to the right by the EWOD force. In the figure, *L* is the total three-phase contact line, *dl* is the unit length on the contact line, $\vec{n}$ is the normal unit and $\vec{t}$ is the parallel unit to the x a-axis.

One potential limitation of the DMF system is the complex control circuit to address each electrode. The typical dimension of the electrode pad is in the order of several mm by mm. To scale up the EWOD system or transport the droplet to different locations of the reaction platform, tens of electrodes are required together with the same number of control channels for the circuitry board. To simplify the design and wiring complexity, several different types of "continuous electrowetting" prototypes have been explored, in which the droplet can be continuously transported with reasonably high speed. Lee *et al.* applied voltage to an enclosed electrolyte channel containing liquid metal drops [194]. Due to the resistive effect of the electrolyte channel, a voltage difference existed between the two ends of the liquid metal slug. The electrical double layer (EDL) at the metal and electrolyte interface was modulated to create surface tension imbalance and propelled the droplet to the lower voltage side. Nelson *et al.* [195] and Ni *et al.*

[196] developed continuous rectified electrowetting by combining diode like structures patterned on a stripe of a highly resistive electrode. Due to the resistive voltage gradient, as the water droplet was applied to the electrode surface, the diodes underneath the water droplet can be either forward biased or reverse biased. The charge built up solely on the reversely biased diode side causing the surface energy change. The droplet thus moved continuously toward the more positive voltage side. By incorporating the AC square wave signal at mediate frequencies (1000 Hz) with a different DC bias, micro-stepping of the droplet could also be implemented on a diode like coplanar electrodes covered by leaky dielectric layers [197]. Fan *et al*. utilized an asymmetric electrode design to continuously pump the droplet with a low-frequency AC square wave (<10 Hz) on an open surface. Droplets are as small as 1 μL could be transported by the asymmetric electrowetting [183].

In this chapter, we design two EWOD systems with the concept of anisotropic ratchet conveyors (ARC), namely the EWOD-ARC system, to directionally transport the droplet. For the first system, we use an AC EWOD actuation approach combined with surface micropatterning to transport the droplet with a reduced number of electrodes. AC EWOD has been used to create global droplet shape oscillations by local capillary force alternations near the contact line in the capillary regime [198]. To transport the droplet, periodic hydrophobic/hydrophilic micro-sized patterns, termed as anisotropic ratchet conveyors (ARCs), are required to provide anisotropic hysteresis force during each droplet shape oscillation cycle. For the second system, we design periodically patterned electrodes on an open coplanar-plate configuration. When the sinusoidal AC voltage is applied, the droplet on top of the electrodes can be continuously pumped to move, with no need for control circuitry. We characterize the frequency response of different droplet volumes as well as the droplet transport on inclined surfaces. By incorporating DC electrodes, we

can realize droplet synchronizing, merging, and mixing functions. A self-cleaning surface system is also designed to clean the surface contaminants on the self-assembled solar panels.

3.2 EWOD System with Anisotropic Ratchet Conveyor Patterning

3.2.1 *System Design*

First of all, we characterized the DC response of the EWOD system. Fig. 3.3 (a) shows the experimental testbench setup in the insets; the experimental contact angle measurements and theoretical calculations of the water droplet contact angle change under the applied voltage are shown together. A 10 μL water droplet was applied on top of a gold electrode, with SiN_x and Cytop as the dielectric layer. A platinum probe (30 gauge) electrode was inserted on top of the water droplet. Two voltage-polarity configurations were tested, shown in the insets of Fig. 3.3 (a). Using equation (3.2), we have $\cos(\theta_v) = \cos(\theta) + \frac{CV^2}{2\gamma_{LG}}$, where θ_v is the apparent contact angle under applied voltage and *C* is the equivalent capacitance between the water droplet and electrode with Cytop and SiN_x as the dielectric layers. In the experimental setup, the film thicknesses and dielectric constants for SiN_x and Cytop were $d_{SiNx} = 220$ nm, $\varepsilon_{SiNx} = 4.2$ and $d_{Cytop} = 100$ nm, $\varepsilon_{Cytop} = 2.1$, respectively, and $\varepsilon_0 = 8.85 \times 10^{-12}\,\frac{\mathrm{F}}{\mathrm{m}}$ is the vacuum permittivity. The equivalent capacitance *C* can be determined by

$$\frac{1}{C} = \frac{1}{C_{SiNx}} + \frac{1}{C_{Cytop}} = \frac{C_{SiNx}+C_{Cytop}}{C_{SiNx}C_{Cytop}} \tag{3-5}$$

resulting in $C = \left(\frac{\varepsilon_0}{d_{SiNx}/\varepsilon_{SiNx}+d_{Cytop}/\varepsilon_{Cytop}}\right) \approx 8.85 \times 10^{-5}\ \mathrm{F/m^2}$. The measurement results corresponded well with the theoretical calculation. Fig. 3.3 (b) shows a linear relation between $\cos(\theta_v) - \cos(\theta)$ and V^2 below the saturation voltage of approximately ±35 V DC, beyond

which the droplet contact angle stopped decreasing with a further increase of the voltage magnitude. The total capacitance of the electrowetting experimental setup can be derived from the slope of the fitting line by solving Eq. (3) for *C*, which was on the order of 8.2×10^{-5} F/m^2.

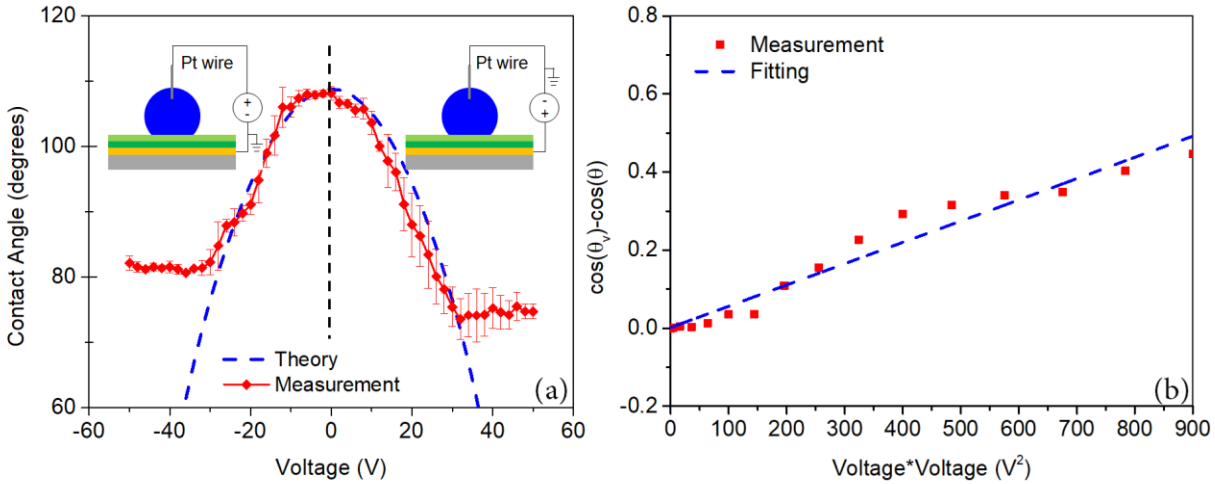

Figure 3.3. (a) Experimental results of the static contact angle change under an applied DC electrical field for a sessile water droplet on a Cytop coated substrate without ARC patterns. The contact angle eventually saturates without further decreasing with increased voltage magnitude. (b) The linear fit plot of the experimental results for $(\cos(\theta_V) - \cos(\theta))$ versus V^2.

We then designed our AC EWOD system, as shown in Fig. 3.4, with coplanar electrodes. The coplanar electrodes consisted of one center electrode and two side electrodes. The side electrodes were connected at one single end. AC voltage was applied between the center and side electrodes to sustain a global droplet shape oscillation by the periodic alternating EWOD force. In terms of surface patterning process, methods have been proposed to reduce surface hydrophobicity like plasma treatment or adhesion layer but the original surface properties will be altered, resulting in water droplet contact angle decrease after surface treatment [149, 199, 200]. To solve this problem, we adopted Parylene C as a stencil mask and created hydrophilic patterns on top of the Cytop surface without degrading the original surface properties.

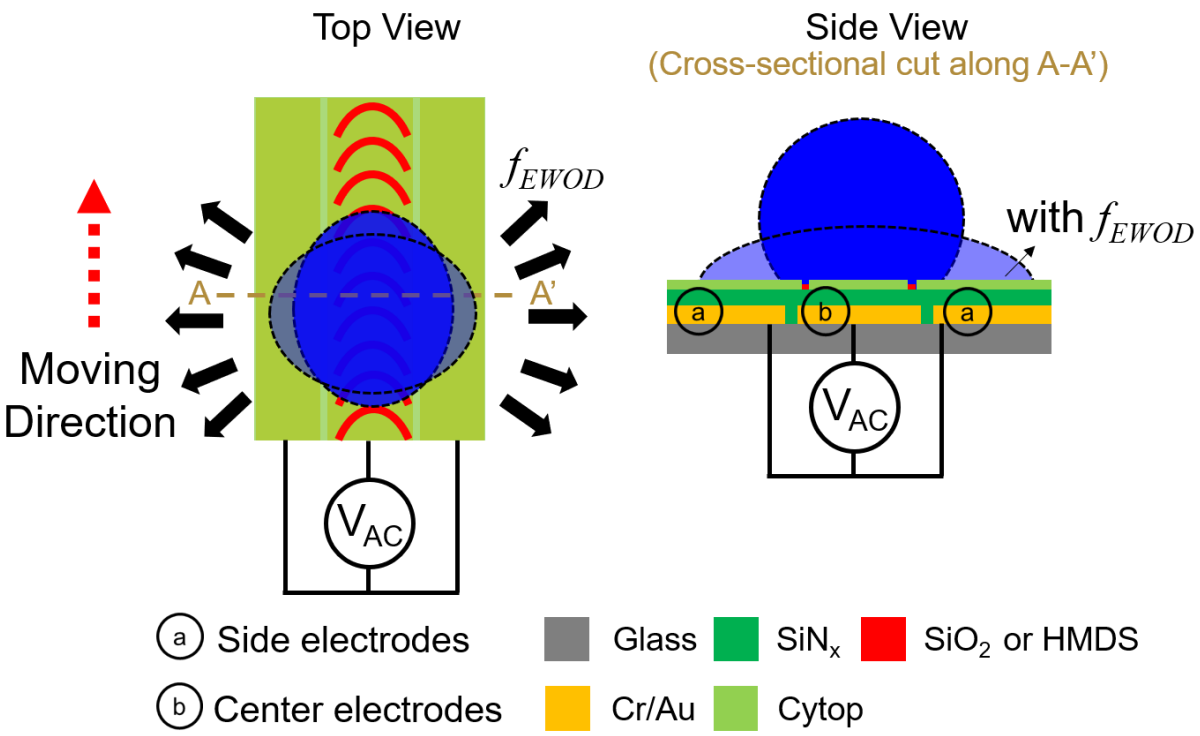

Figure 3.4. The top view and side view schematic of the coplanar EWOD system with ARC texture patterns. The dashed line between A and A' from the top view plot on the left represents the cross-sectional cut plane for the side view plot on the right. The water droplet oscillates due to the EWOD force (f_{EWOD}) when an AC signal is applied, which is demonstrated by the partial overlapping of the spherical droplet and the flattened droplet by f_{EWOD} on the hydrophobic Cytop surface. The curved ARC rungs provide an anisotropic wetting force on the leading and trailing edge of the droplet, causing the directional movement of the droplet.

3.2.2 *Fabrication Process*

The system was fabricated on a 4" soda-lime glass wafer. Shown in Fig. 3.5, 10 nm Cr and 50 nm Au were patterned by electron beam evaporation to create coplanar electrodes using a lift-off process. The SiN_x layer was deposited using PECVD. Diluted Cytop (Cytop: CT-Solv 180 = 1:3) was spin-coated and cured at 200 °C for 1 hour. The wafer was coated with 2.5 µm Parylene C as the stencil mask. 10 nm Al was evaporated on the Parylene C surface as an etch stop mask and

patterned to define the ARC tracks. The exposed Parylene C area was etched with RIE. The wafer was coated with 50 nm SiO_2 by electron beam evaporation or treated with hexamethyldisilazane (HMDS) by spin coating. The Parylene C layer was carefully peeled off using tweezers before further testing.

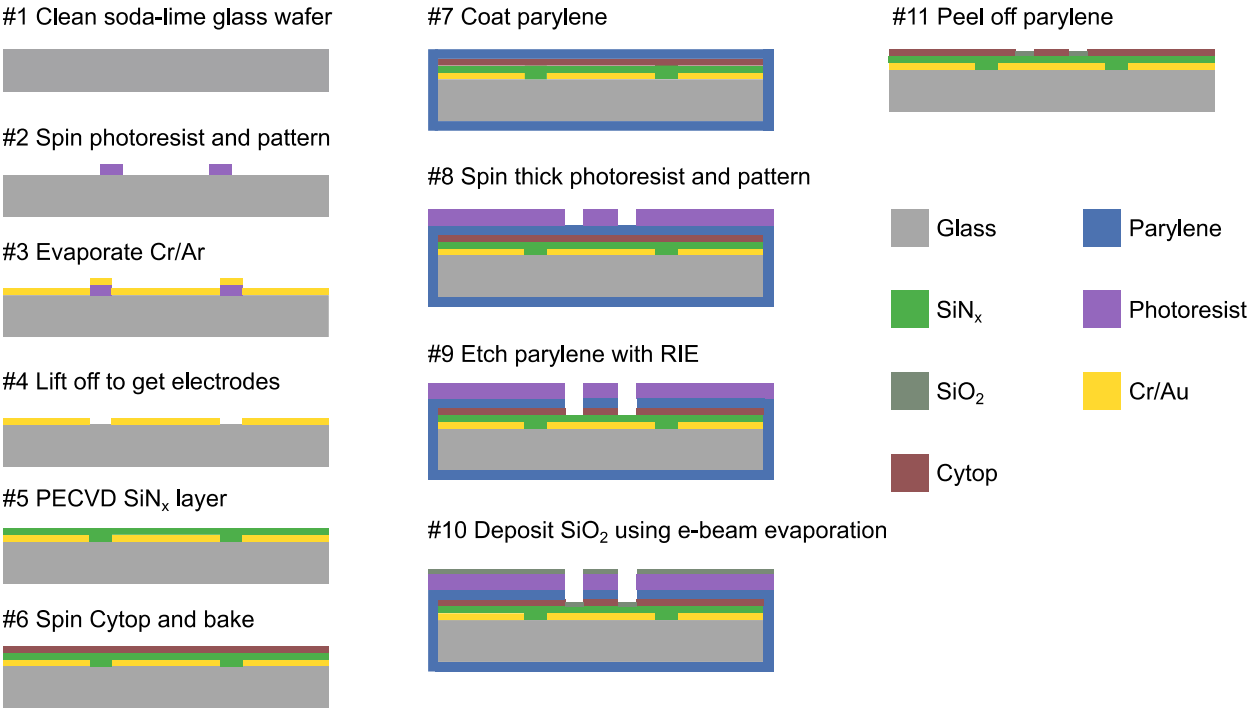

Figure 3.5. Detailed fabrication process flow diagram.

3.2.3 *Experimental Setup*

AC signals were provided by a function generator and amplified by a voltage amplifier (PZD700, Trek Co.) with a voltage amplifying factor of 200 V/V. A water droplet with 15 µL volume was pipetted and the droplet silhouette monitored by a high-speed camera (FASTCAM Mini UX100) with a sampling rate of 2000 fps.

3.2.4 *Characterization Results*

When applying an AC voltage on the coplanar electrodes, the water droplet started to oscillate laterally driven by the alternating electrowetting force. Simultaneously, the portion of the solid-liquid-air three-phase contact line (TPL) on the center electrode recessed and advanced in response to the droplet expanding and contracting laterally. We denoted the contact line aligned with the ARC curved pattern as the leading edge and the opposite side as the trailing edge. Like in prior experiments where the droplets were driven by the orthogonal vibration [148], both leading and trailing edges periodically wetted and dewetted the ratchets at hydrophobic/hydrophilic boundaries of the ARC pattern. Due to the periodic curved shape of the ARC design, anisotropic hysteresis force occurred at the TPL causing the droplet to move towards the direction of the ARC curve.

The top view of the system with its dimensions after fabrication is shown in Fig. 3.7 (a) and a detailed picture of the ARC pattern with its dimensions are shown in Fig. 3.7 (b). The ARC rungs are designed to match approximately the curvature of the footprint of the droplet [124, 148]. A typical movement of the water droplet's leading and trailing edges with time is plotted in Fig. 3.7 (c). The leading and trailing edges expanded at 0.23±0.019 mm and 0.21±0.013 mm, respectively, from the initial position in the expansion phase, while the leading and trailing edge recessed 0.11±0.015 mm and 0.33±0.007 mm in the contraction phase. The leading edge conformed to the hydrophilic ARC rungs, creating a longer TPL and thus a higher pinning force than the trailing edge, which made only intermittent contact with the hydrophilic rungs. The anisotropic hysteresis force caused the water droplet to move forward. When an alternating electrical field ($V(t) = V_0 \sin \omega t$) was applied, the EWOD force could be described as $f_{EWOD} = \frac{1}{2}CV^2$ (measured in N/m), which is proportional to $(1 - \cos 2\omega t)V_0^2$, driving the droplet to oscillate at twice the frequency of the AC voltage [201]. The droplet oscillation frequency in our case was equal to 100 Hz,

corresponding to 50 Hz AC voltage applied. The average droplet movement speed can be estimated by checking either the leading or the trailing edge position change over a certain period. As shown in Fig. 3.7 (c), the total position change of the trailing edge (ΔY) is approximately 1.3 mm within 100 ms of transport time, which results in an estimated transport speed of 13 mm/s.

The droplet motion originates from the force asymmetry and hysteresis at the leading and trailing edges of the contact line on the ARC, which consists of heterogeneous regions with hydrophobic/hydrophilic patterns. The effective force exerted on the contact line along the axis of the ARC can be described using equation (2-1). Fig. 3.8. (a) shows a typical scenario when the droplet rests on the ARC rungs. The leading edge of the droplet continuously wets along the hydrophilic/hydrophobic boundaries while the trailing edge has intermittent contact with hydrophobic and hydrophilic regions. By inserting the empirically determined χ values from Fig. 3.8 (a) and the contact angle hysteresis data of hydrophobic and hydrophilic materials into equation (2-1), we can calculate the apparent contact angle hysteresis at the leading and trailing edges during advancing and receding. We experimentally measured the advancing and receding angle of Cytop and HMDS using a drop shape analyzer (KRÜSS DSA100L). With $\theta_{phob,adv} = 115°$, $\theta_{phob,rec} = 101°$, $\theta_{phil,adv} = 79°$, and $\theta_{phil,rec} = 64°$, we obtain: $\cos\theta_{app,lead,adv} = -0.42$, $\cos\theta_{app,trail,adv} = 0.32$, $\cos\theta_{app,lead,rec} = 0.35$, and $\cos\theta_{app,trail,rec} = -0.01$. Further, with $d = 3$ mm and $\gamma_{LG} = 0.072$ N/m, we get: $F_{lead,adv} = -91.3$ μN, $F_{trail,adv} = 75.7$ μN,$F_{lead,rec} = 70.1$ μN, and $F_{trail,rec} = -2.3$ μN. The force asymmetry during advancing and receding is $F_{asym,adv} = -15.6$ μN and $F_{asym,rec} = 67.8$ μN, respectively. From equation (6), the results imply force anisotropy of $F_{an} = 52.2$ μN toward the moving direction.

Fig. 3.8 (b) plots the corresponding contact angle change of the leading and trailing edges with time. We observed that within each cycle, the leading edge had larger apparent contact angle hysteresis than the trailing edge, leading to larger hysteresis forces over each vibration cycle. Our system can transport a range of droplet sizes within a certain frequency bandwidth under a fixed voltage amplitude input. To move a droplet with a volume of 15 μL, the frequency can vary from 5 to 50 Hz. Fig. 3.9 shows a top view of two ARC ratchets pointing in opposite directions patterned on AC EWOD tracks. Two 15 μL water droplets were transported with 20 Hz sinusoid AC voltage in the opposite directions simultaneously, demonstrating a successful EWOD-aided controlled water droplet transportation platform without the need for complex control circuitry.

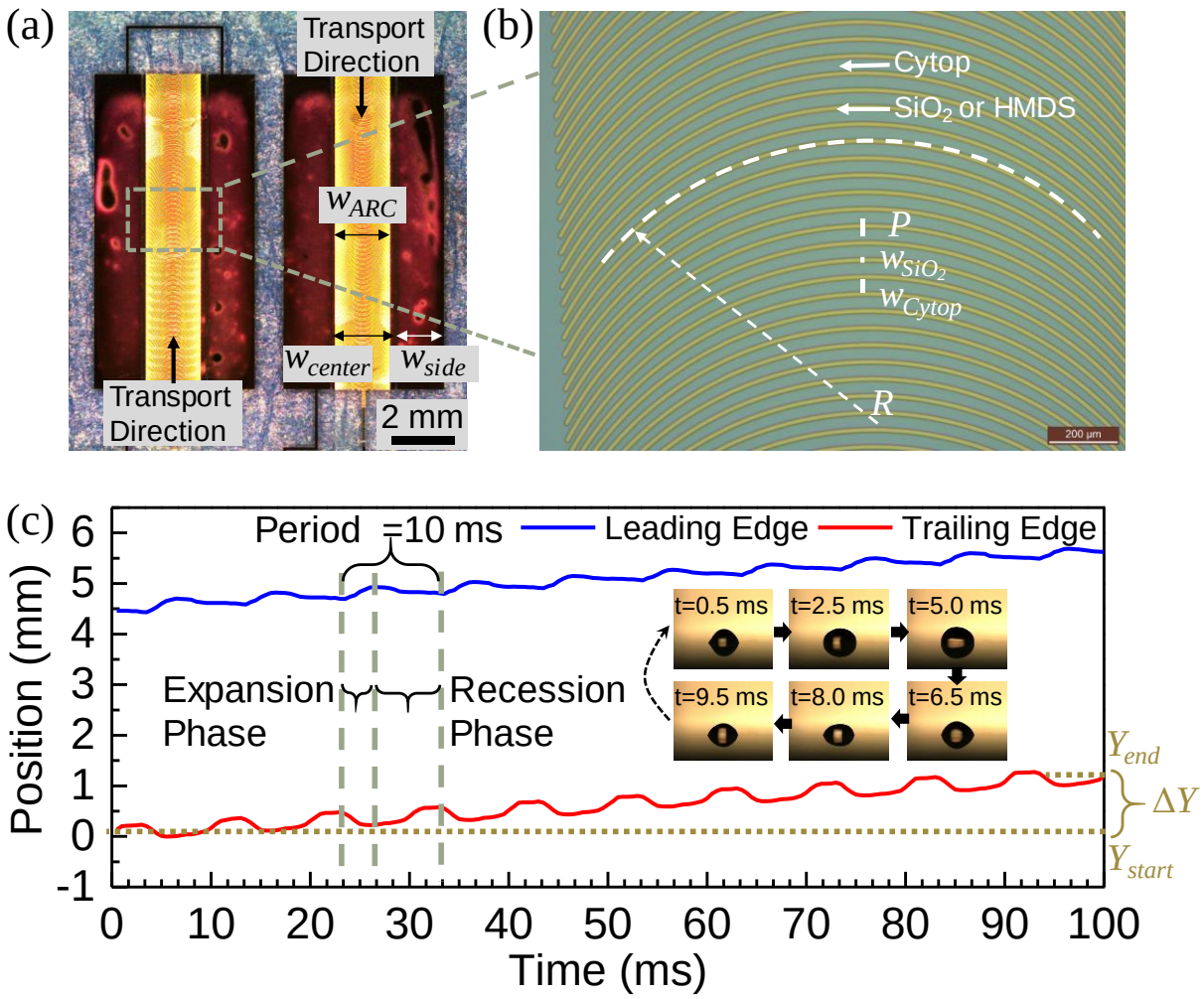

Figure 3.6. (a) Top view of the fabricated device. Two ARC tracks with opposite droplet transport directions are shown side by side. The width of the center electrodes (w_{center}) is 2 mm, the side electrode width (w_{side}) is 1.5 mm and the gap between the electrodes is 50 μm. The width of the ARC (w_{ARC}) is 1.76 mm. (b) Optical microscope image of the ARC patterns. The rung period pitch (p) is 50 μm, with the hydrophilic stripe width (w_{SiO_2}) 10 μm and the hydrophobic stripe width (w_{Cytop}) 40 μm. The radius of curvature (r) for the ARC is 1000 μm. (c) Change in position of leading and trailing edges of a 15 μL water droplet on the Cytop-SiO_2 surface with time. The applied voltage was a 60 V_{peak} sinusoid signal at 50 Hz. Insets show water droplet silhouettes recorded by the high-speed camera within one period (T = 10 ms). The droplet transport speed can be estimated by the trailing edge position change ($\Delta Y = Y_{start} - Y_{end}$) over the measurement period (100 ms).

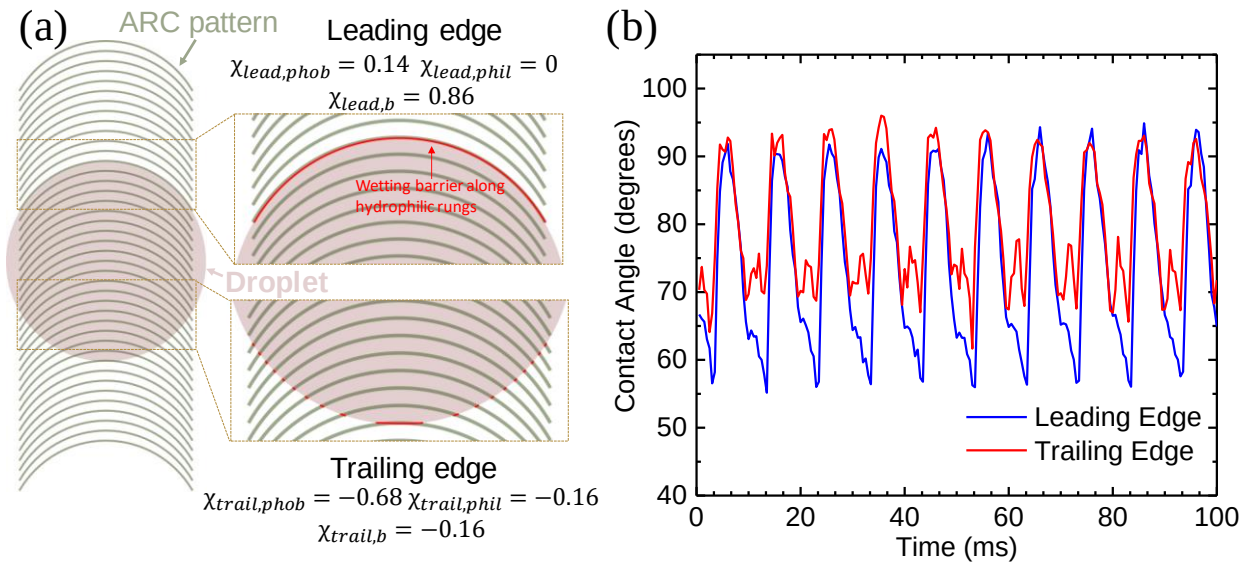

Figure 3.7. (a) Schematic of a droplet on an ARC surface. In the drawing, the diameter of the droplet is 3 mm. The radius of the rung is 1.5 mm with a rung width of 10 μm. We use image processing techniques to obtain an estimated value $\chi_{lead,b}$ for the projected wetting barrier length along the leading edge. For the trailing edge, we assume $\chi_{trail,phil} = \chi_{trail,b}$. (b) The contact angle change of droplet leading and trailing edge with time. Pinning anisotropy of the leading and trailing edge can be seen during each oscillation cycle period (T = 10 ms) as a difference in the corresponding contact angles.

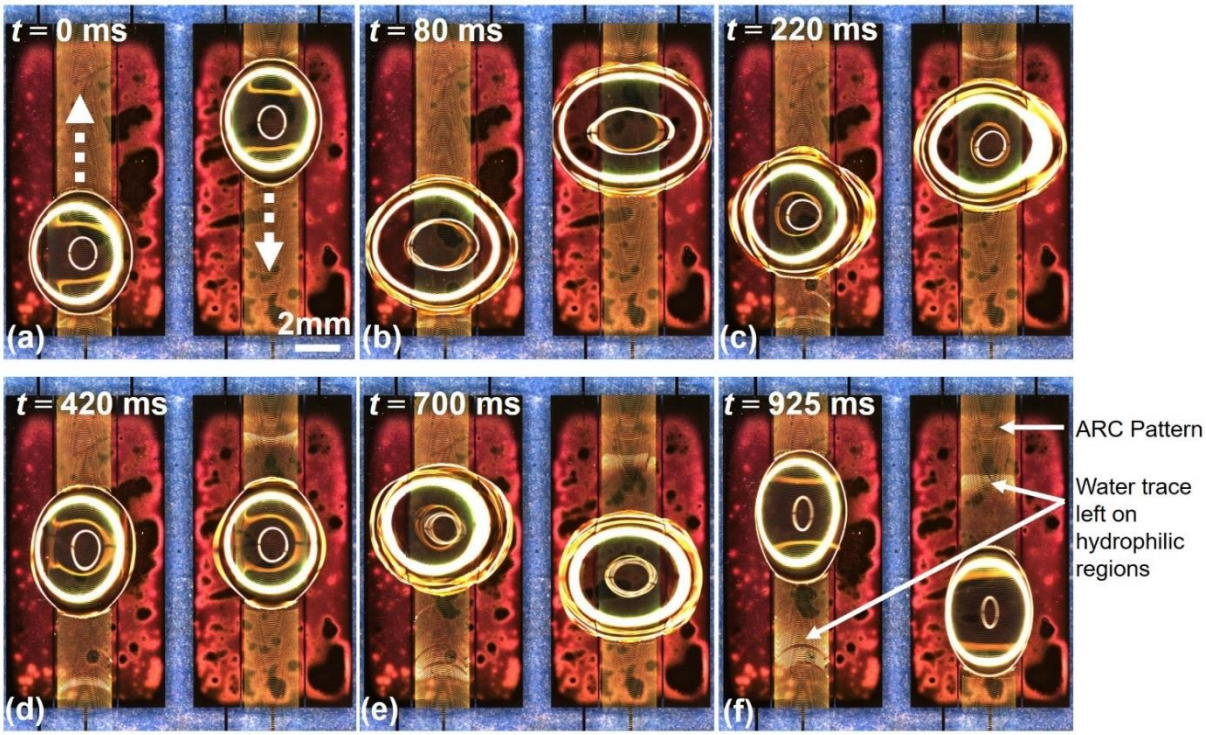

Figure 3.8. Top view of water droplet transport under a 20 Hz 60 V_{peak} sinusoid electrical signal on Cytop-SiO_2 surface. The two adjacent ARC tracks were designed to transport two droplets in opposite directions at the same time. The droplet transport directions are indicated by the white arrow in (a). We noticed that the water trace on the hydrophilic regions could be reduced by using less hydrophilic surface finish treatment (*e.g.* hexamethyldisilazane) compared with SiO_2.

3.3 Droplet Control Using Patterned Coplanar Electrodes

Besides the combination of coplanar electrodes and ARC, we also developed a method to transport the droplet with patterned coplanar electrodes with uniform top coating. When a sine AC voltage is applied, the droplet on top of the electrodes can be continuously pumped to move, with no need for control circuitry. In our design, inspired by the ARC structure, we develop the arc shape and chevron shape electrodes and apply sine waves in between the adjacent electrodes. Different droplet sizes (5~15 μL) have been tested and the droplet transport speed can reach 20 mm/s for 15 μL at 20 Hz external AC frequency. Meanwhile, by introducing DC EWOD electrodes, we can

perform multiple droplets manipulating functionalities including droplet synchronizing, merging, and mixing, which provides potential applications including active self-cleaning surfaces and lab-on-chip instruments.

3.3.1 *System Design*

Electrodes with periodic arc or chevron shapes are patterned on the substrate, followed by a uniform dielectric passivation layer and a hydrophobic top coating (Fig. 3.9). When an alternating electrical field ($V(t) = V_0 \sin\omega t$) is applied, the surface hydrophobicity at the droplet three-phase contact line (TPL) changes. The EWOD force drives the droplet to oscillate at twice the frequency of the AC voltage. Anisotropic EWOD forces are created by the asymmetric electrode design during each oscillation cycle, causing the droplet to move along the surface.

3.3.2 *Fabrication Process*

The system was fabricated on Si wafers or glass substrates. The substrate was first cleaned with piranha solution (H_2SO_4:H_2O_2 = 4:1) at 110 °C for 10 min, rinsed with deionized (DI) water and dried with nitrogen gas using a Spin Rinse Dryer (ClassOne Technology, Inc.). For the Si wafer, a layer of 2 μm SiO_2 was deposited with PECVD (SPTS Technologies, Inc.) at 350 °C as the substrate insulation layer. The substrate was then treated with oxygen plasma for 1 min at 50 W in a barrel asher (Glow Research) and then put into the priming oven with hexamethyldisilazane (HMDS) vapor at 150 °C. 1.2 μm photoresist AZ1512 was spin-coated on the wafer surface and the electrode ratchet pattern was directly exposed with a Heidelberg-MicroPG-101 mask writer (Heidelberg Instruments Mikrotechnik GmbH). The photoresist was developed with AZ340 photoresist developer (AZ340 : DI water = 4:1) for 1 min. The substrate was coated with 10 nm Cr and 60 nm Al by e-beam evaporation and soaked in acetone for lift-off. Then a layer of 350 nm

SiN_x was deposited by PECVD (SPTS Technologies, Inc.) at 350 °C on top of the electrodes as the dielectric layer. Diluted Cytop solution (Cytop : CT solv180 = 1:3) was spin-coated and baked at 200 °C for 1 hour with a final thickness of ~70 nm.

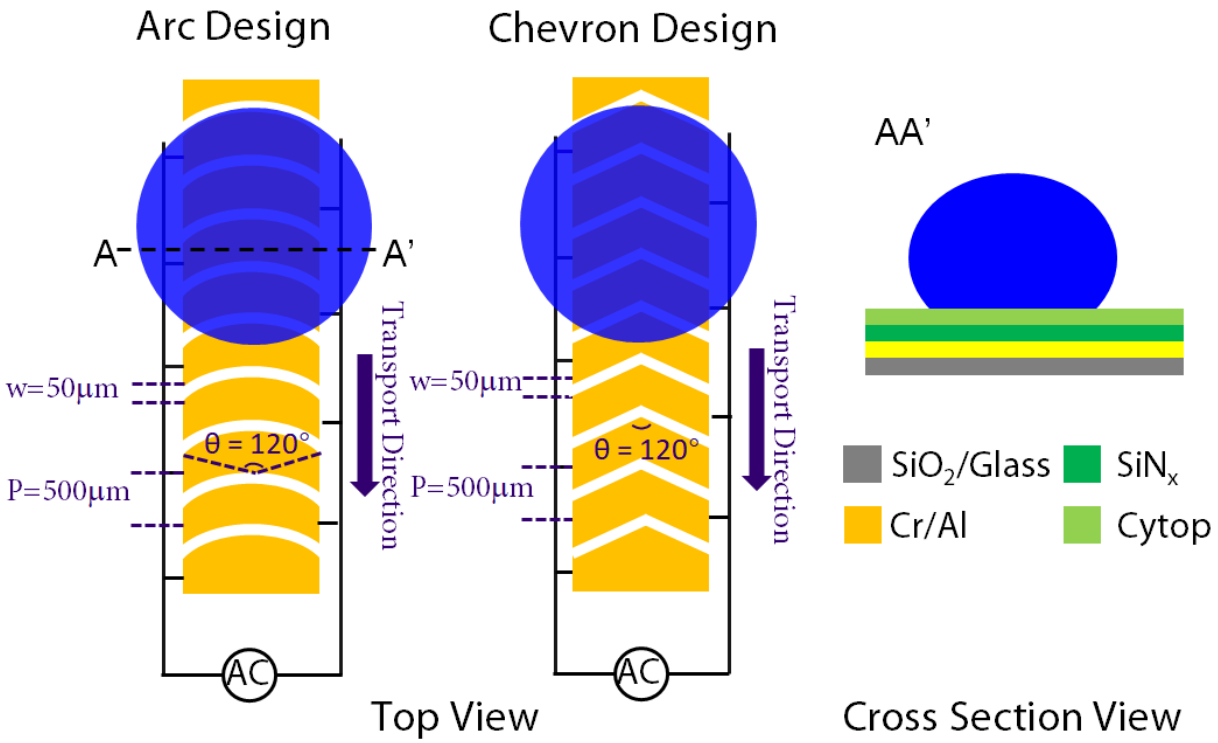

Figure 3.9. Top view and cross-section view of the basic AC EWOD system with anisotropic rachet conveyor electrodes. Both the arc and chevron-shaped electrodes are tested. The period (*P*) of the adjacent electrodes is 500 μm, the gap width (*w*) is 50 μm, the width of the electrode track (*W*) is 2 mm and the angle (θ) is 90° or 120°.

3.3.3 *Experimental Setup*

AC signals were provided by a function generator (Agilent 33120A) and amplified by a voltage amplifier (PZD700, Trek Co.) with an amplifying factor of 200 V/V. DC signals were provided from a high voltage DC power source. A water droplet was pipetted, and the droplet silhouette was monitored by a high-speed camera (FASTCAM Mini UX100) with a sampling rate of 1000 fps. The droplet position and contact angle change with time were analyzed with MATLAB custom

code. The function generator and high-speed camera were synchronized by a transistor-transistor logic (TTL) input port to characterize the phase delay between the sine AC voltage and the droplet oscillation. Droplet transport on an inclined surface was characterized by a self-customized tilting stage. The inclination angle was measured with a triple-axis accelerometer (MMA8451, Adafruit, Inc.).

3.3.4 *Droplet Transport Characterization*

We characterized the droplet leading and trailing edge position change, line spreading speed, and contact angle change with time, shown in Fig. 3.10 (a). The AC voltage is 160 V_{pp} at 20 Hz. The position oscillation shows a periodicity of 25 ms (40 Hz). The droplet transport speed was estimated from the change in center position as 20 mm/s. The Reynolds number was calculated as: $Re = \rho \times v \times L/\mu$, where ρ is the water density (1000 kg/m^3), v is the velocity of water movement (20 mm/s), L is the characteristic length - the droplet diameter (3.2 mm), and μ is the dynamic viscosity (8.90×10^{-4} kg/ms). The Reynolds number was 72 suggesting a laminar flow. Fig. 3.10 (b) shows a sequential top view of droplet transport. The droplet leading and trailing edges moved to the next adjacent electrodes during each single oscillation cycle.

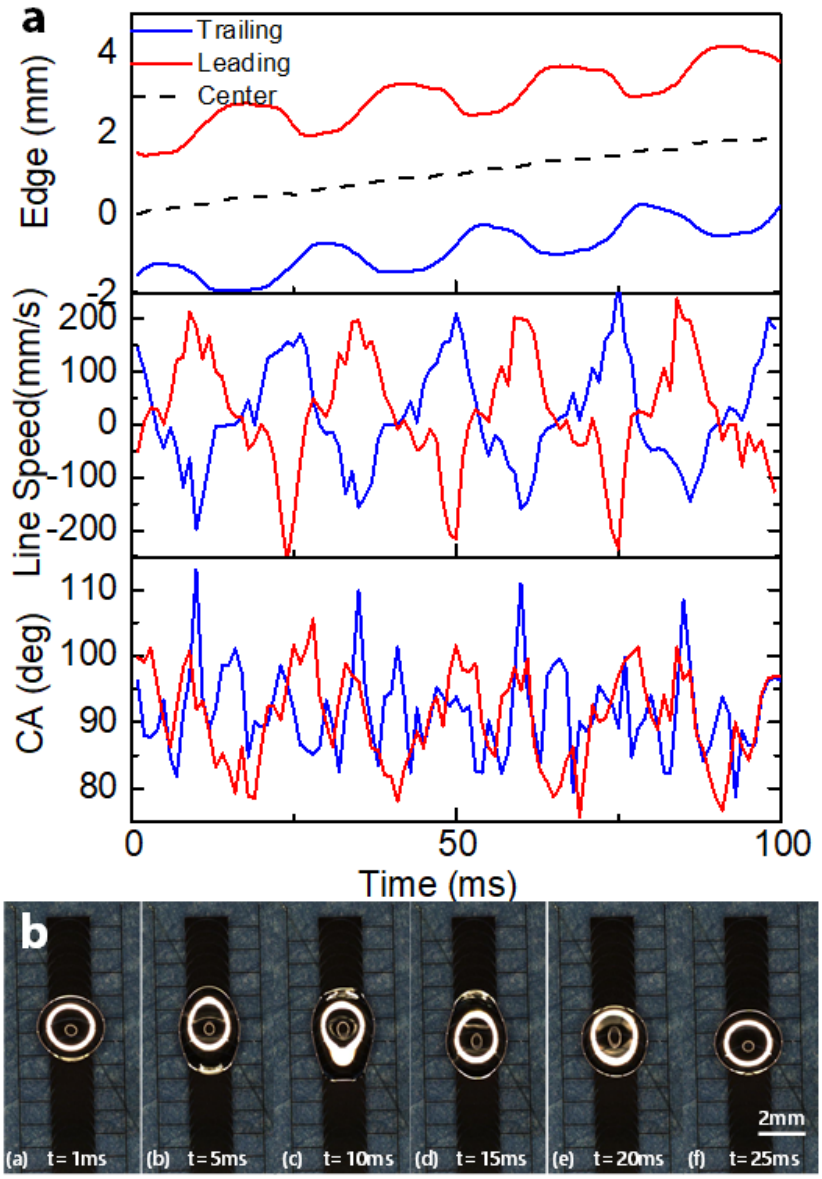

Figure 3.10. (a) Droplet leading edge, trailing edge, edge center, edge line spreading speed, and contact angle (CA) change with time. The droplet volume is 15 μL. (b) Top view of 10 μL droplet transport on ARC electrodes.

3.3.5 *Droplet Frequency Response*

As shown in Fig. 3.11, we calculated the Bode plot of the change in droplet width versus frequency. The total change in width attained the maximum value at the resonance frequency. For a half AC cycle, the maximum droplet expansion width is limited by the size of the energized electrode

beneath the solid-liquid interface, because the adjacent reference electrodes are hydrophobic and prevent the droplet to spread further. By synchronizing the external AC signal and the droplet edge oscillation with time, we extracted the phase delay information between the external EWOD force and the change in droplet width. The droplet response was in phase at low frequencies and could reach 180° out of phase at higher frequencies.

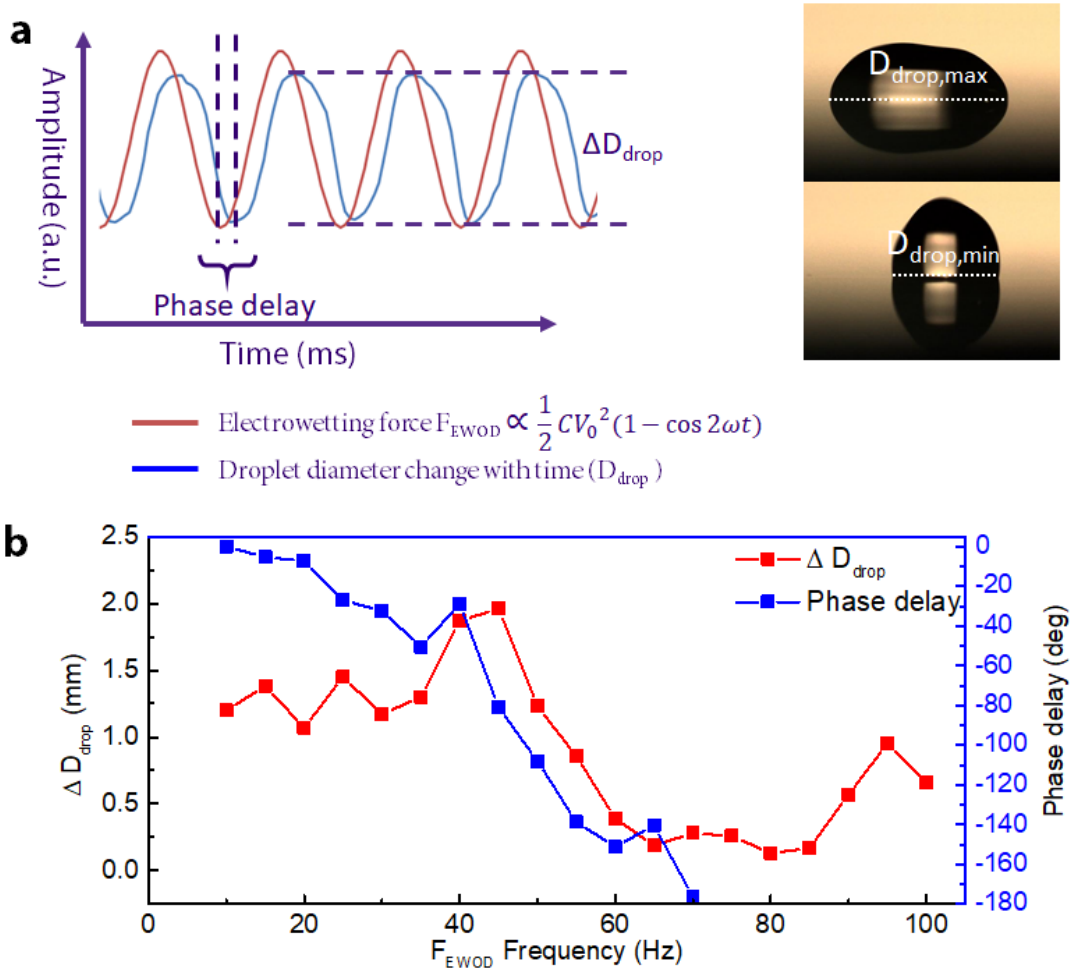

Figure 3.11. (a) Simultaneous plot of change in droplet total width and electrowetting force f_{EWOD}. The pictures on the right show 15 µL droplets when D_{drop} was at maximum and minimum position. ΔD_{drop} is the difference between $D_{drop,max}$ and $D_{drop,min}$. (b) ΔD_{drop} and phase delay of the 15 µL droplet plot with time. The resonance frequency occurred when the droplet width change was at maximum and the phase delay was close to -90°.

3.3.6 *Droplet Transport on Inclined Surfaces*

We tested the capability of manipulating droplets on inclined or even upside-down surfaces on our EWOD-ARC system, to determine the practical feasibility of distinct geometric configurations beyond a single plain surface. DMF EWOD systems with patterned electrodes have been demonstrated on inclined [202], vertical [203] or flexible curved surfaces [204], termed as all-terrain droplet actuation (ATDA). Fig. 3.12 presents the maximum inclination angle for the droplet to be moved in sideways and uphill directions on the tilted surface. The resisting force to prevent the droplet from sliding down the inclined surface is usually described in terms of contact angle hysteresis, and the condition for the droplet to remain pinned to the surface is:

$$\pi r\,\gamma\,(\cos\theta_R - \cos\theta_A) > \rho V\,g\,\sin\alpha \tag{3-6}$$

where θ_A and θ_R are advancing and receding angles, r is the droplet radius, γ is the water surface tension, ρ is the water density, α is the surface inclination angle and V is the water droplet volume. In our case, due to the EWOD effect at the interface between the droplet and the electrodes, the surface tended to become more hydrophilic with increased advancing/receding angle difference to help pin the droplet. Our tests show that small droplets (~5 μL) could overcome gravity and move sideways on vertical surfaces without sliding, as well as on upside-down surfaces.

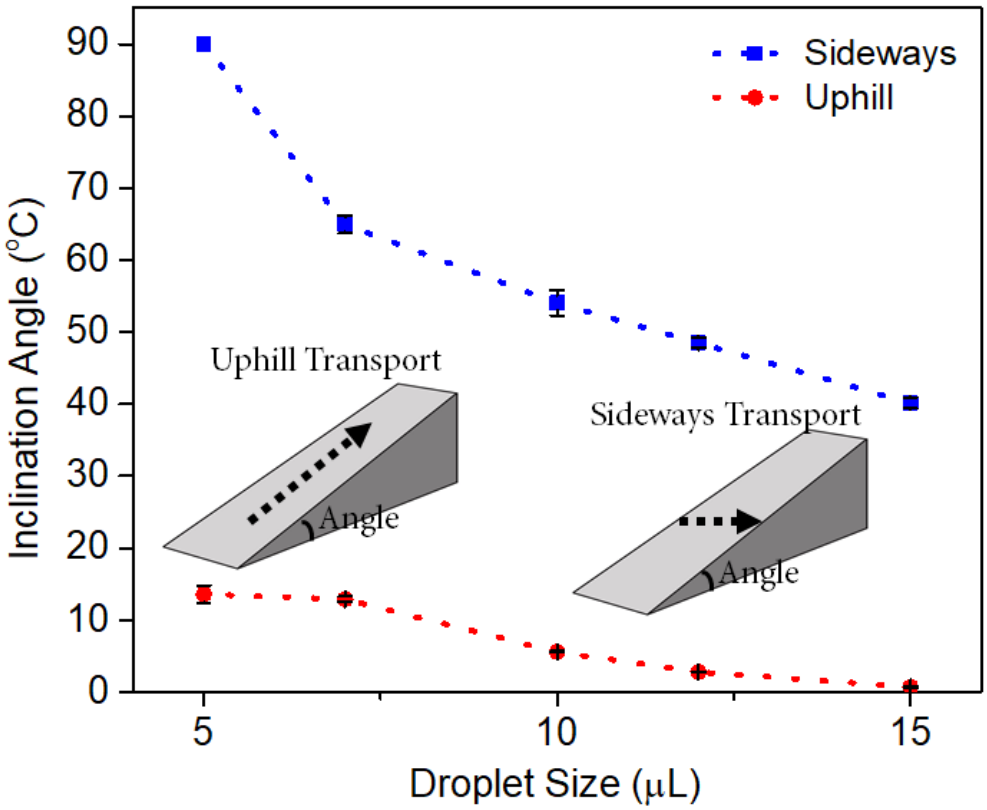

Figure 3.12. Maximum inclination angle for different volumes (5~15 μL) of droplets to transport on EWOD-ARC electrodes with 240 V_{pp} 30 Hz sine wave. For each volume data point, 3 droplets were tested. The droplets were applied on top of the electrodes while being energized. The dotted arrow in the figure presents the designated droplet movement direction defined by the electrode patterns.

3.3.7 *Droplet Sorting, Mixing and Merging*

By introducing side DC electrodes, we were able to expand the functionality of our EWOD-ARC design to perform droplet synchronization, merging, and mixing. Fig. 3.13 shows an example of droplet synchronization. We fabricated the side DC electrode pair layer first and AC electrodes were patterned on top of the DC pair electrodes, insulated with a 350 nm SiN_x layer. The size of the single DC electrode was 3 mm by 2 mm and the gap distance between the two DC electrodes was 50 μm. When only AC electrodes were energized, the droplet would move from one end to

the other. When both AC and DC electrodes were energized, the droplet movement was trapped and stopped by the DC field, shown in Fig. 3.13 (a)-(d). When the DC bias was removed, the droplet continued to move along the electrode track and resumed transportation by the AC field (Fig. 3.13 (e)-(f)).

Fig. 3.14 shows a design configuration when two droplets can be moved in opposite directions. The DC electrode pair was patterned at the center. The two droplets were first transported by the EWOD-ARC tracks and moved in the opposite direction (Fig. 3.14 (a)-(b)). Then the droplets were trapped and merged at the center by the DC electrodes (Fig. 3.14 (c)-(d)). The merged droplet continued to be agitated and to be further mixed by the AC signal (Fig. 3.14 (e)-(f)).

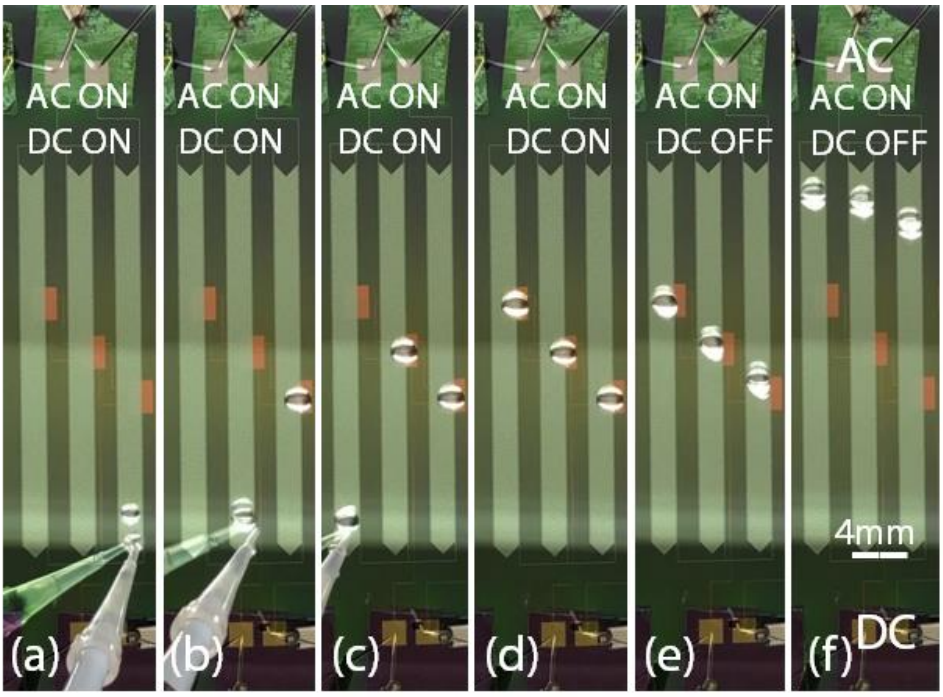

Figure 3.13. Sequential images of droplet synchronization on a SiO_2 substrate with three EWOD-ARC tracks. DC electrodes were at the bottom, separated from the top AC electrodes with a 350 nm SiN_x dielectric layer. Another SiN_x layer and a Cytop layer were coated on top of the AC electrodes.

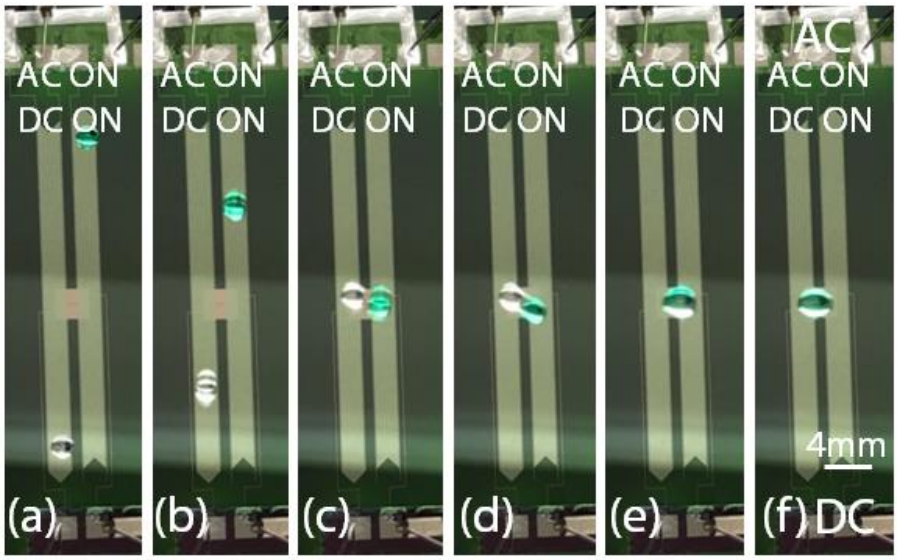

Figure 3.14. Sequential images of droplet merging and mixing with the aid of AC and DC (100 V). The green droplet was colored with food color solution.

3.3.8 *Self-cleaning Surface Design with EWOD*

We designed self-cleaning surfaces with patterned coplanar electrodes. Glass substrate with transparent ITO coating on top was patterned with multiple electrode tracks. Fig. 3.15 (a) demonstrates the pattern design. The track width was 3 mm and the gap distance between the adjacent track is 1.5 mm. A 2×2 electrode track group was patterned to cover 2" by 2" surfaces. The patterned ITO substrates were then coated with SiN_x and Cytop. The glass substrate was then attached on top of the 2" by 2" amorphous silicon solar cell. Dust particles were applied on top of the patterned surfaces. The self-customized solar module was mounted on a 30° inclined surface. 240 V_{pp} 30 Hz AC voltage was applied to the electrode track groups. Fig. 3.15 (b1) – (b9) showed surface cleaning procedures. Discrete 10 μL water droplets were applied to the electrode tracks. The droplets were able to be transferred to the other end while cleaning the surface contaminants along the path. Multiple droplets could be applied to a single track and merged at the other end. The dirty droplets would fall off the surface by gravity after merging several 10 μL droplets.

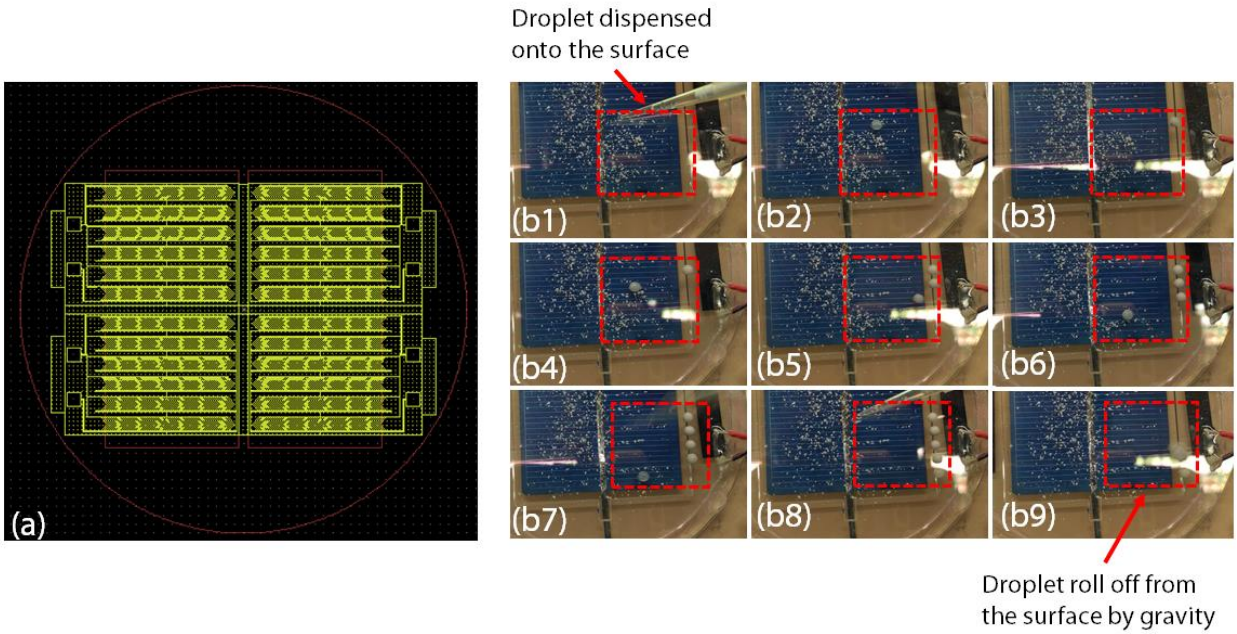

Figure 3.15. (a) Layout CAD design of 2×2 electrode track groups design. (b1)-(b9) shows sequential images of patterned ARC-EWOD tracks on the solar panel cover glass surface. The red dotted square region (size 1" by 1") is patterned with ARC-EWOD tracks. The entire solar panel sample is mounted on a 30° inclined surface.

3.4 CONCLUSION

In conclusion, an AC EWOD actuation approach combined with surface micropatterning was introduced. The microscopic patterning technique on a hydrophobic Cytop layer was realized by using Parylene C as a stencil etching mask. The water droplet static contact angle change was studied and characterized by the specific EWOD system design. Instead of using orthogonal vibrations to the substrate, droplet oscillation was initiated with electrowetting on the dielectric. The droplet was transported by the anisotropic force along with the ARC patterns using only two globally controlled electrodes. For the second system, we designed periodically patterned electrodes on an open coplanar-plate configuration. The droplet can be transported along a large distance without complicated control circuitry. Droplet transportation speed, contact angle change,

phase delay, and the capability to move on inclined surfaces were tested. We also realized functions including droplet synchronizing, merging, and mixing by introducing additional DC electrodes. Besides Cr/Al, our design works with ITO electrodes, creating an optically transparent platform. We also explored the possibility of integrating our technology into active self-cleaning surfaces and lab-on-chip applications.

Chapter 4. DIRECTIONAL DROPLET TRANSPORT AND FOG REMOVAL ON TEXTURED SURFACES USING LIQUID DIELECTROPHORESIS

4.1 INTRODUCTION

The ability to remove microparticles or micro drops from a surface is important for many applications, including self-cleaning surfaces [172, 205, 206], condensation heat transfer enhancement [207, 208] and anti-icing applications [96]. In the era of Internet of Things (IoT), robotics and autonomous vehicles (AV), it is crucial to keep the surface of optical sensors clean, like cameras or lidars, and to reduce the risk of malfunctioning and miscommunication [129]. Approaches have been proposed to actively or passively capture or counteract condensation and accelerate the speed of moisture removal from the surface. Walker *et al.* designed transparent light-absorbing metasurfaces using alternating thin layers of Au and TiO_2 to reduce the defogging time under sun exposure [209]. Bai *et al.* [210] and Song *et al.* [211] designed bio-inspired wettability gradient surfaces by creating hydrophilic wedge patterns on a hydrophobic or super-hydrophobic background to enable spontaneous water drop movement and improve the water collection efficiency. Yan *et al.* developed an enhanced water capture system taking advantage of the EWOD effect [212].

In this chapter, we performed an active surface cleaning approach for surface fog removal by a combination of anisotropic ratchet conveyors (ARCs) and liquid dielectrophoresis (L-DEP). L-DEP agitates the droplet with interdigitated coplanar electrodes on an open surface configuration [213-215]. Anisotropic forces at the leading and trailing edges of the droplet directionally transport the droplet over each modulation cycle. The water condensation can be cleaned by the droplet transport along the ARC track.

4.2 System Design

Two electrohydrodynamic approaches have been widely applied to manipulate the water droplet wettability on a solid surface with an external electrical field, namely EWOD and L-DEP [216]. EWOD happens under DC or low AC frequencies (<1 kHz) with extra charge accumulating at the liquid-solid interface to alter the interfacial tension. L-DEP utilizes much higher frequencies (~10 kHz – 200 kHz), and the polarization of the dipoles within the liquid gives rise to Maxwell stress at the liquid-air interface [217]. The L-DEP body force density acting on liquids can be expressed in terms of the Korteweg-Helmholtz relation [181]:

$$\overrightarrow{f_k} = \sigma_f \vec{E} - \frac{\varepsilon_0}{2} E^2 \nabla \varepsilon_f + \nabla \left[\frac{\varepsilon_0}{2} E^2 \frac{\delta \varepsilon_f}{\delta \rho} \rho \right] \quad (4\text{-}1)$$

where ρ is the liquid density, ε_f is the liquid permittivity, E is the electrical field intensity and σ_f is the free charge. The first term on the right describes the electrostatic force, the second term describes the dielectrophoresis force and the last term can be neglected because the fluid density remains constant. The penetration depth of the electrical potential, and thus the electrical field, decays exponentially from the liquid-solid interface into the liquid. The L-DEP force is strongest at the three-phase contact line. The motion of the liquid will be confined along the electrodes due to the periodic energy barriers.

4.3 Fabrication Process

The system was fabricated on Si wafers or glass substrates. The substrate was first cleaned with piranha solution (H_2SO_4:H_2O_2 = 4:1) at 110 ℃ for 10 min, rinsed with deionized (DI) water and dried with nitrogen gas using a spin rinse dryer (Avenger Ultra-Pure, ClassOne Technology, Inc.). For the Si wafer, a layer of 2 μm SiO_2 was deposited with PECVD (Delta LPX, SPTS Technologies, Inc.) at 350 ℃ as the substrate insulation layer. To fabricate the interdigitated

electrodes (IDE), Cr thin film (100 nm) was deposited on the substrate by PVD sputtering (LAB 18, Kurt J. Lesker, Inc). Photoresist AZ1512 (1.2 μm) was spin-coated on the wafer surface and the electrode ratchet pattern was directly exposed with a Heidelberg-MicroPG-101 mask writer (Heidelberg Instruments Mikrotechnik GmbH). The photoresist was developed with AZ340 photoresist developer (AZ340:DI water = 4:1) for 1 min. The IDE electrodes were etched by wet chemical processing using the Cr etchant for 2 min. SiN_x thin film (350 nm) was deposited on top of the electrodes as the dielectric layer by a CVD process. Diluted Cytop (Asahi Glass Co. Ltd) was spin-coated on the dielectric layer and baked under 180 °C for 1 hour as the hydrophobic region. For Cytop patterning, we utilized Parylene C as a stencil mask since photoresist could not form a uniform layer on top of the hydrophobic Cytop surface [218-220]. Parylene C (2.5 μm) was evaporated on the Cytop using a commercial parylene coater (PDS 2010, Specialty Coating Systems, Inc.) under vacuum. Photoresist AZ9260 (6 μm) was coated and patterned. The Parylene C stencil mask and Cytop were etched through together with O_2 plasma using reactive ion etching (Vision 320 RIE, Plasma-Therm, Inc.). The Parylene C stencil mask was peeled off with tweezers. The exposed SiN_x regions without the Cytop coverage was treated with spin-on hexamethyldisilazane (HMDS) for a hydrophilic surface finish. The whole wafer was baked at 110 °C for 2 min to improve the bonding of the HMDS to the SiN_x regions.

4.4 Experimental Setup

AC signals were provided by a function generator (33120A, Agilent Inc.) and amplified by a voltage amplifier (PZD700, Trek Co.) with an amplifying factor of 200 V/V. A water droplet was pipetted, and the droplet silhouette was monitored by a high-speed camera (FASTCAM Mini UX100) with a sampling rate of 1000 fps. The droplet edge and contact angle change with time were analyzed with MATLAB custom-made code. The function generator and high-speed camera

were synchronized by a transistor-transistor logic (TTL) input port to capture the droplet shape change with time under the electrical field. To transport the droplet, an Arduino compatible electromagnetic relay board was controlled by a digital signal that turned on and off the electrical voltage applied to the IDE. The water droplet static contact angle (CA) on uniformly coated Cytop surfaces were measured with a Krüss Drop Shape Analyzer (DSA 100). For the droplet sliding angle measurement, a custom-made experimental setup was designed using a 3-axis accelerometer (MMA8451 from Adafruit).

4.5 Characterization Results

We first tested 3 different IDE electrode designs with a layer of uniform Cytop coating for the study of droplet spreading width and contact angle under a high frequency square wave input signal. The non-uniform electric fringe field-induced dipoles in liquid resulted in the L-DEP force on the droplet. The L-DEP force was sensitive to the input voltage and frequency [181, 221, 222], and the maximum change in droplet width under different frequencies were plotted in Fig 4.1. It follows from equation (4-1) that for deionized water, σ_f is close to zero and the L-DEP body force becomes $\overrightarrow{f_k} = -\frac{\varepsilon_0}{2} E^2 \nabla \varepsilon_f$. A larger AC voltage amplitude input led to a stronger E-field and a stronger L-DEP body force. At the same time, the dielectric constant of water was dependent on the input frequency and thus influenced the magnitude of the L-DEP body force. A stronger L-DEP body force resulted in more droplet deformation and contact angle change. Compared with the interdigitated straight-line design electrodes, the folded-line design electrodes helped the droplet to overcome the periodic energy barriers and spread wider. The maximum droplet width under L-DEP could be more than twice compared to the initial droplet width on the Cytop surface with zero voltage input.

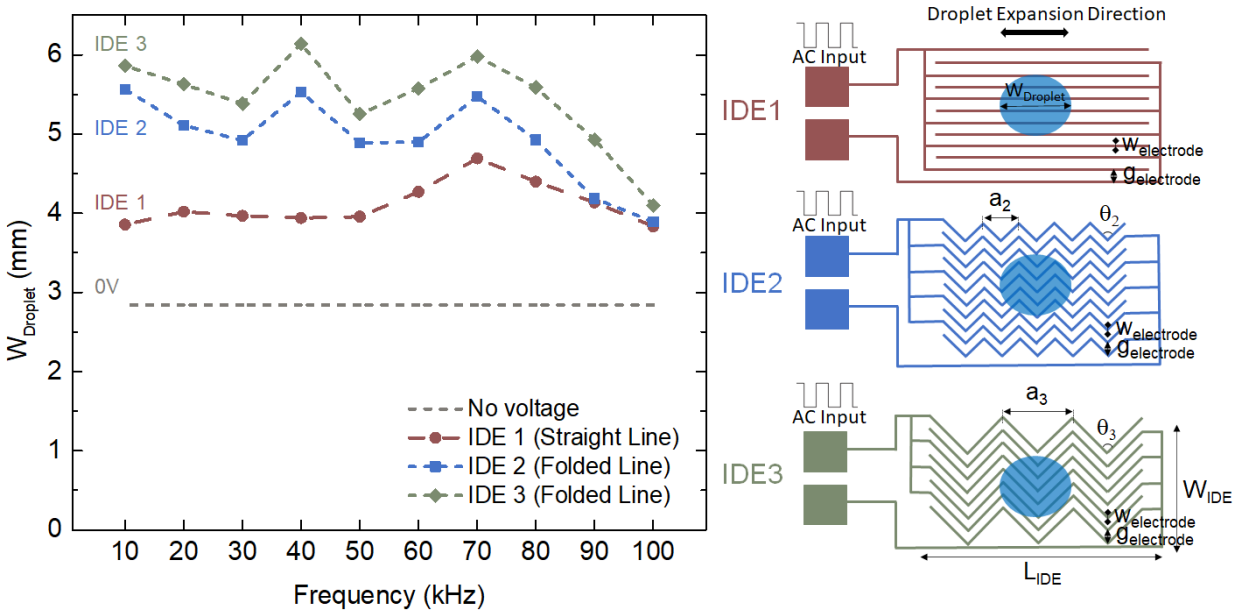

Figure 4.1. Droplet (10 μL) width in steady state in response to the AC square wave input frequency. The AC voltage amplitude is 400 V_{pp}. The frequency varies from 10 kHz to 100 kHz. We investigated 3 designs of the IDE electrodes with straight-line design and two folded line designs. The gap between adjacent electrodes ($g_{electrode}$) is 50 μm. The width of each single electrode ($w_{electrode}$) is 50 μm. The total length of the IDEs (L_{IDE}) is 12.5 mm. The total width of the IDEs (W_{IDE}) is 5 mm. For the folded line design, a_2 = 1 mm, a_3 = 2 mm, and $\theta_2 = \theta_3 = 90°$.

Fig. 4.2 shows the droplet contact angle change under different voltage amplitudes on the straight-line IDE electrodes. The voltage ranged between 0 and 360 V. As the input voltage increased within the tested range, the droplet spread along the longitudinal finger electrodes and the contact angle altered from 108° to 38°, demonstrating a strong wetting and super-spreading behavior of the droplet under L-DEP force, which was impossible to achieve using an electrowetting-on-dielectric (EWOD) platform. Our previous measurements showed that the contact angle under DC voltage only altered between 108° and 80° [218]. The droplet contact angle stopped to further decrease because of the contact angle saturation [223].

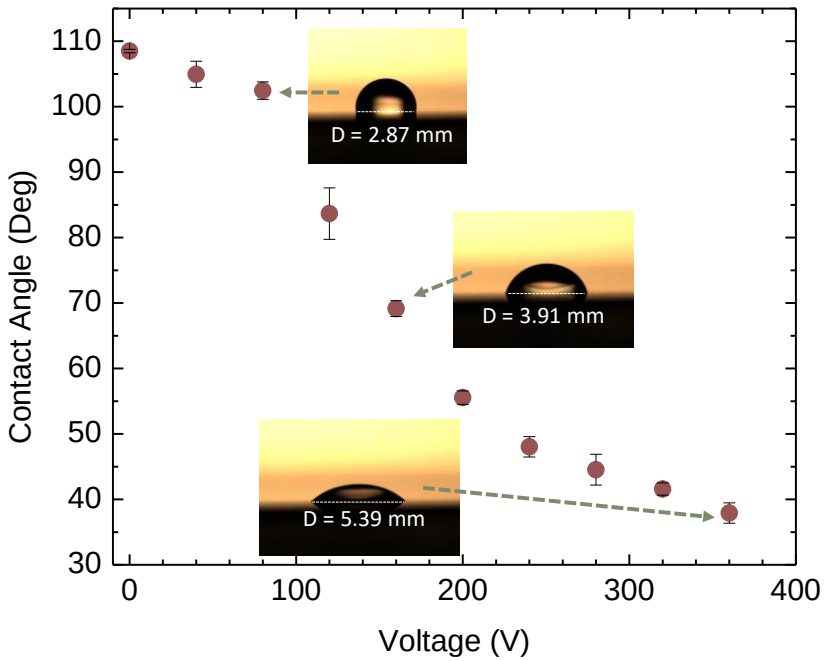

Figure 4.2. Droplet (10 μL) contact angle change vs. AC square wave voltage amplitude. The AC square wave voltage has a frequency of 10 kHz. Data is shown with ± one standard deviation for n = 3 different measurements.

We then patterned hydrophilic curved ARC rungs on Cytop using the Parylene C stencil mask process. Fig. 4.3 (a) shows an example of the ARC patterns on top of the IDE and dielectric layers. The ARC pattern was parallel to the longitudinal IDE finger directions. As shown in Fig. 4.3 (b), the Cytop maintained good hydrophobicity with a high contact angle and a low sliding angle after peeling off Parylene C compared with the Cytop surface as deposited. Fig. 4.3 (c) showed the configuration setup to control the droplet to move on the ARC patterned surface using L-DEP force. The function generator continuously outputs the AC square voltage, which was amplified by the voltage amplifier. With the assistance of the ARC pattern, we were able to directionally move the droplet by modulating the input AC voltage with an electromagnetic relay. The relay was turned on and off with the Arduino microcontroller so that the droplet would expand and recess periodically along with the ARC pattern. The droplet was then transported along the surface

with the help of anisotropic forces at the leading and trailing edge during each cycle.

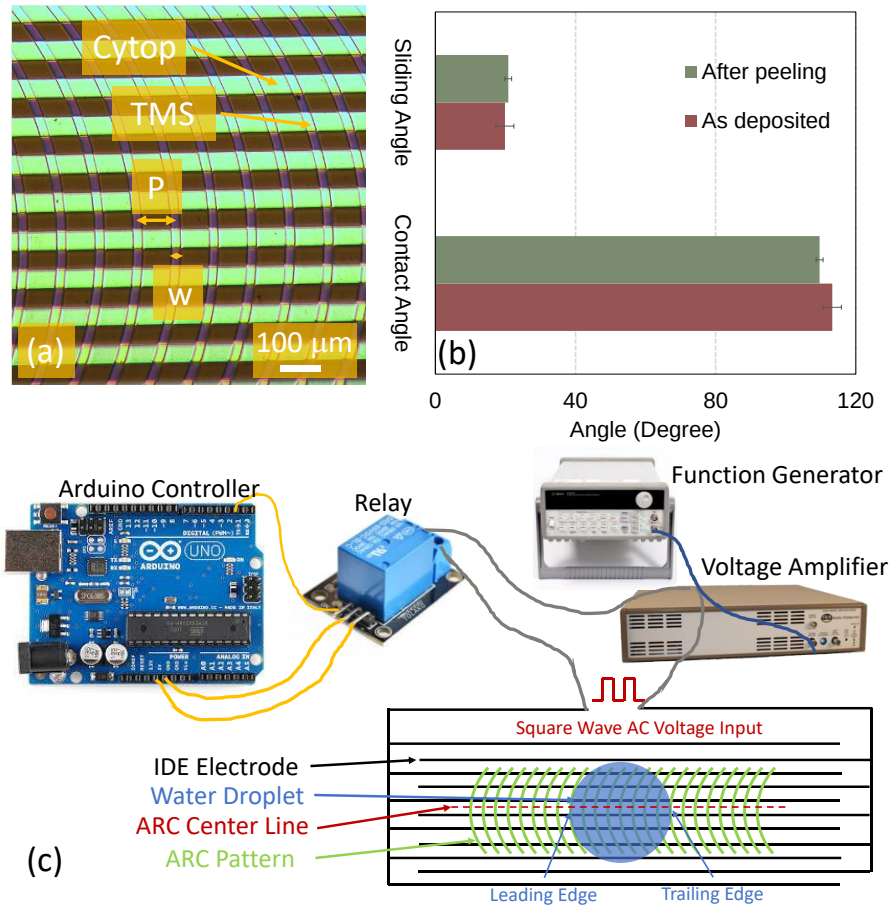

Figure 4.3. (a) SEM images of ARC patterns on Cytop. For each curved rung, the radius of curvature (R) is 1000 μm, the etched linewidth (w) is 10 μm, and the period (P) between adjacent rung centers is 100 μm. (b) Contact angle and sliding angle measurement for Cytop before and after peeling off Parylene C. (c) Schematic of the test setup and ARC patterned surface.

Fig. 4.4 shows the characterization results of the droplet leading and trailing edge position change and spreading time. The AC square voltage was turned on and off every 100 ms (5 Hz modulation frequency). During the expansion phase, when the AC square voltage was connected, the leading edge expanded by 290 μm within 14 ms, and the trailing edge expanded by 460 μm within 16 ms. During the recession phase, when the AC square voltage was disconnected, the leading edge was pinned by the ARC pattern with little movement while the trailing edge recessed

at 750 μm within 24 ms. The average movement distance during each modulation cycle was about 290 μm. The total time spent on the droplet expansion and recession was 40 ms, thus the potentially fastest modulation frequency was 25 Hz, and the potentially fastest droplet transport speed under this condition was estimated at the order of 7.25 mm/s.

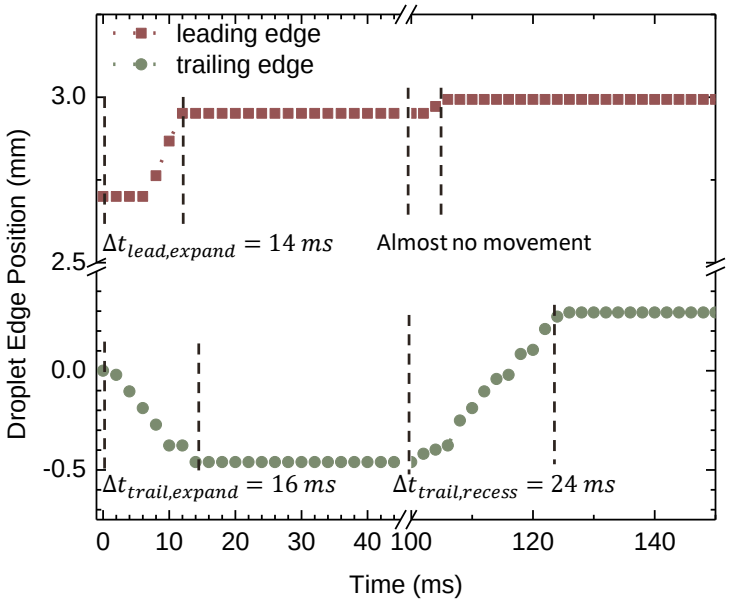

Figure 4.4. Droplet (10 μL) edge position change with time during expansion and recession phase. The AC voltage is 300 V_{pp} at a frequency of 10 kHz. The AC voltage is modulated by the electromagnetic relay every 100 ms to connect or disconnect with the IDE electrode.

Fig. 4.5 shows a top view demonstration of the droplet transport by our L-DEP platform with the assist of ARCs. Compared with the mechanically driven system, the L-DEP platform could transport the droplet independently of the droplet self-resonance frequency while using only two control terminals without complex control circuitry. In the mechanically driven system, the external drive frequency was chosen to match the sessile droplet resonance frequency (at the order of tens of Hz) in order to achieve the maximum expansion amplitude. The droplet expansion amplitude rapidly decayed as the mechanical drive frequency deviated from the droplet resonance frequency and the droplet stopped moving. In contrast, on the L-DEP platform, the droplet's

maximum expansion was tuned by the external electrostatic field. The longitudinal length of the IDE electrodes was 20 mm and the total width was 6.4 mm. The ARC track was patterned at the center of the IDE electrodes. We also tested different droplet sizes on the same ARC track design and droplets from 2 μL to 20 μL could be transported along. The current drawn from the voltage amplifier was measured at a peak-to-peak level of 11 mA under a 400 V_{pp} actuation voltage at 20 kHz. The power consumption when the droplet rested on ARC patterns increased ~2.6% when compared with the droplet resting on the uniform Cytop surface.

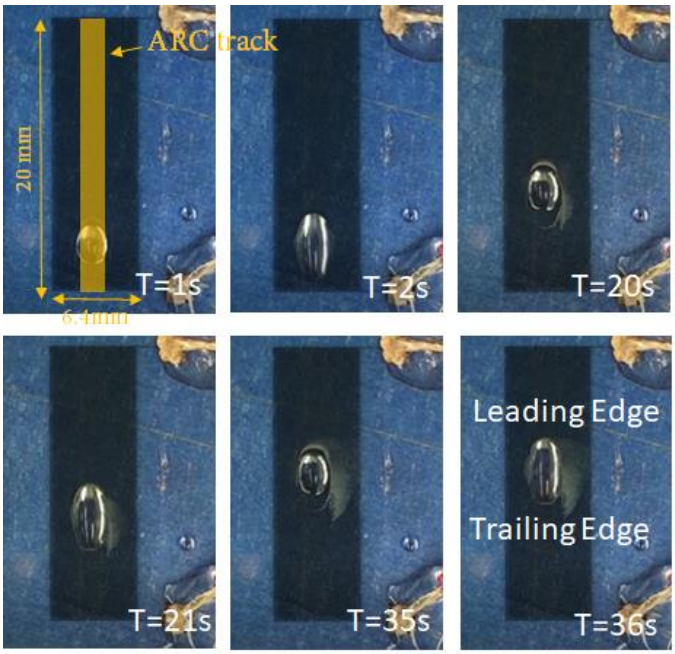

Figure 4.5. Top view of a 10 μL droplet moving on the IDE electrodes with ARC patterns. The AC voltage was 400 V_{pp} at 20 kHz. The average transport speed was estimated as 0.17 mm/s. The electromagnetic relay was switched on and off every 1 s. The patterned ARC track region is highlighted in yellow shading in the T=1s figure.

We exposed our device surface to a humidifier for at least 60 seconds to cover the entire device surface with tiny drops that mimic a foggy surface. The drop sizes on the surface ranged between 1~100 μm in diameter based on image processing with ImageJ software. The estimated thickness

was in the order of tens of microns on average. Then we pipetted a droplet on the ARC track and turned on the AC voltage input. As evident from the sequential images in Fig. 4.6, the droplet was able to move along the ARC track and clean the fog away. Fig. 4.6 (a) shows the initial state when the droplet was put on the foggy surface and Fig. 4.6 (b)-(f) present the droplet when it was actuated. We noticed that the external voltage helped in the merging of the tiny drops to larger ones before the surface was further cleaned by the 10 μL droplet. The L-DEP force could still deform the droplet in the presence of multiple tiny water drops on the surface. This behavior is different from the EWOD system, where the droplet would stop moving or reduce its moving speed when a layer of fog is present, since the fog layer blocks the solid-liquid interface. The system was only tested with fog generated from DI water. We believe that our system could remove fog with low conductivity (<1 mS/m), while a modified design in terms of dielectric materials and electrode geometry optimization would be necessary for more conductive solutions (in the order of 10 mS/m).

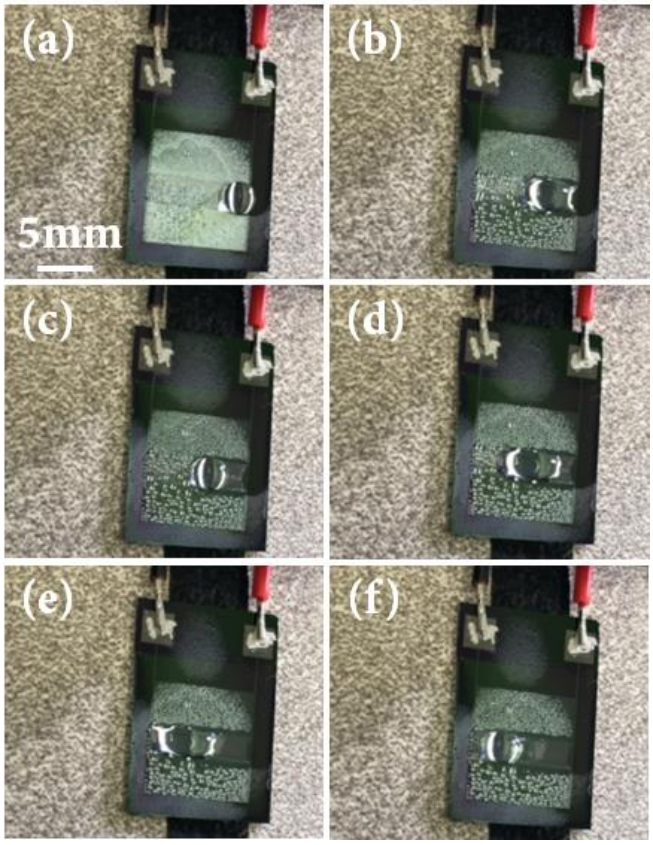

Figure 4.6. (a)-(f) sequential images of surface fog removal using a 10 μL droplet.

4.6 CONCLUSION

In this chapter, we presented the design, fabrication, and characterization of droplet transport with L-DEP on an ARC track. The system demonstrated the robust capability to transport a broad range of droplet sizes and to manipulate the droplet independently of resonance frequencies for different volumes. The setup required an electromagnetic relay to modulate the high input voltages but no additional complex control circuitry. We predicted that the droplet could be moved at a speed of 7.25 mm/s based on the droplet response time during expansion and recession. We also presented the capability to remove surface fog with our design, which has proven difficult to accomplish with an EWOD system.

Chapter 5. DROPLET DELIVERY AND NEBULIZATION SYSTEM USING SURFACE ACOUSTIC WAVE FOR MASS SPECTROMETRY

5.1 INTRODUCTION

Within the field of proteomics, there is a general interest in developing platforms that simplify the sample preparation process, to reduce the volume of fluid analytes used to prepare peptides and proteins for analysis by available mass spectrometry (MS) as well as to eliminate sample contamination. It is equally important that these platforms are compatible with the current commercially available MS due to the widespread use of MS in proteomics. However, integrating both fluid analyte manipulation and aerosolization capabilities for MS remains a challenge.

Digital microfluidics enables liquid manipulation in discrete droplet formats and provides a lab-on-a-chip (LOAC) platform. The LOAC platform provides flexible and complex droplet manipulations, including creating, cutting, moving, merging and mixing droplets [120, 181, 224, 225]. There are multiple techniques available for digital microfluidics including heat [226-228], optical methods [229, 230], magnetic fields [8], mechanical vibrations [124, 148], electrowetting-on-dielectric (EWOD) [187, 202, 231], liquid dielectrophoresis (L-DEP) [232], and acoustic fields [233]. In order to interface LOAC platforms with MS, analyte ionization techniques are required. Two popular approaches, namely electrospray ionization (ESI) [234] and matrix assisted laser desorption ionization (MALDI) [235, 236], are widely used. The ESI process uses a high electrical potential across a capillary that ejects a stream of positively charged drops. During the path of flight, the charged droplets break into charged ions due to solvent evaporation and Coulombic fission. Notably, ESI effectively handles a large detectable mass range [237] with impressive sensitivity. To produce ions by MALDI, typically a specific matrix solution is first mixed with the

sample and allowed to co-crystallize on a metal plate. The pulsed laser ablation on the metal surface creates ionized analyte molecules for MS analysis. MALDI provides a rapid, sensitive, and low-cost method and can examine multiple samples at the same time. Integrated digital microfluidic platforms and aerosolization techniques have also been demonstrated with parallel sample processing capability [238] and improved detection signal intensity [173].

However, nonideal scenarios may occur in both aerosolization methods because of the nature of the analyte or the solvent. For ESI, a high voltage potential must be applied to the liquid analytes during the ionization process. The accessories in the ESI system, such as channels, nozzles, and capillaries, are easily fouled by the liquid analytes. For MALDI, matrix ions can interfere with low mass-to-charge ratio (*m/z*) analyte ions. In this chapter, we present the development of an aerosolization interface by adopting surface acoustic wave nebulization (SAWN). SAW technology has been widely adopted in various commercial devices such as tactile displays [239, 240], radio frequency filters [241, 242], microfluidic systems [243-245], chemical sensors [246], and optomechanical systems [247, 248]. The SAWN platform creates ions from bulk liquid analytes directly in an ambient environment at atmospheric pressure. SAWN can operate in progressive wave mode (Fig. 5.1 (a)) and standing wave mode (Fig. 5.1 (b)). Demonstrated in Fig. 5.1 (c), when the SAW comes into contact with a liquid medium along its path, the leaky SAW is launched into the liquid, with the refraction angle θ_R. Typically, the vibration frequency is high (10 MHz) but the excitation power is relatively low [249]. SAWN does not require high voltage and as a result provides advantages for labile molecule analysis [250, 251]. Moreover, there is no interference with low *m/z* analyte ions on the SAWN platform which unlike MALDI uses no matrix that can interfere [252].

In general, there are challenges to 1) automatically deliver a droplet on the SAWN platform for mechanical clearance from stationary dispensing; 2) make nebulization droplet location consistent for each individual droplet and from droplet to droplet; and 3) seamlessly nebulize the analytes in solvent on chip into the gaseous phase. Integration of droplet manipulation functions to precisely deliver, position, mix and merge analytes are desirable for a potentially automated SAWN platform with mass spectrometer [253]. Here, we present use of a droplet directional manipulation approach to combine anisotropic ratchet conveyors (ARC) with the SAWN platform [172, 219]. By creating ARC patterns on a SAWN surface, we can control the directional movement of the droplet and confine the droplet position during the nebulization process. Additionally, while not shown here samples could be mixed on chip allowing some basic chemistry (*e.g.* hydrogen-deuterium exchange [254]) to take place prior to nebulization. Mass spectrometry results using a SAWN source are presented under different input resonance frequencies, which demonstrates a controllable nebulization rate by altering the input frequencies.

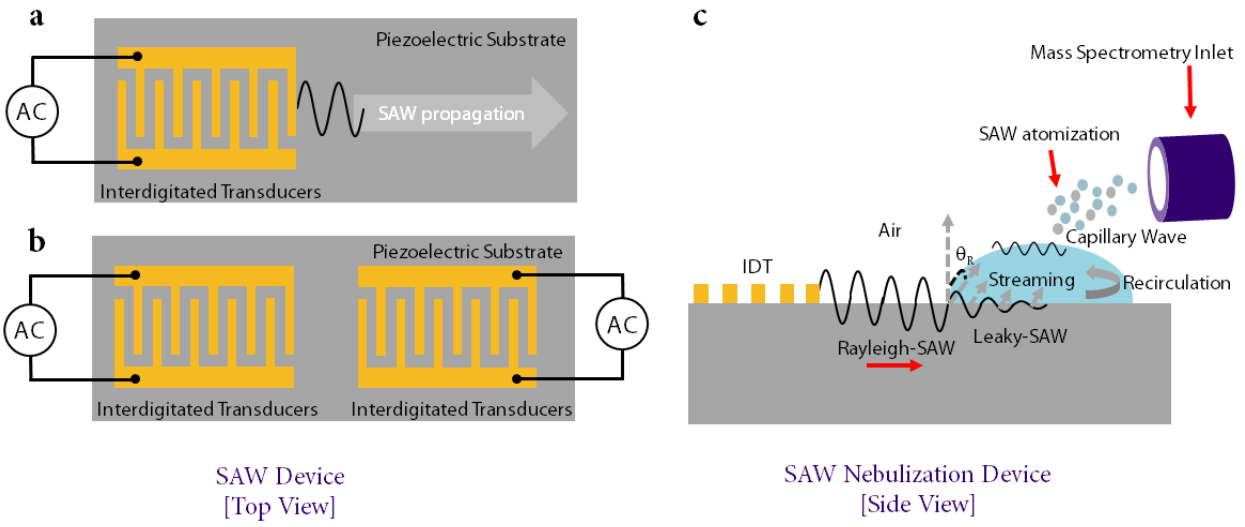

Figure 5.1. SAWN device configuration. (a) Progressive wave mode. (b) Standing wave mode (c) Droplet atomization and delivery into mass spectrometry.

5.2 System Design

The design of the standing wave SAWN device with ARC patterning is shown in Fig. 5.2. The total width of the active interdigitated electrodes (IDE) region (W_{IDE}) is 10 mm. Considering the propagation speed of SAW is 3960 m/s at the excitation frequency of 9.56 MHz, the linewidth (I_E) and the gap between the adjacent edges (I_G) of the metal electrodes are designed to be 103.6 μm. To generate and optimize standing waves, the distance between the two excitation electrodes (L) needs to be designed as $(n+0.5)\lambda$ by the superposition of progressive waves generated by the top and bottom IDEs [255], where n is an integer and λ is the wavelength. In our design, λ = 414.4 μm and n = 15, giving a distance of L = 6.2 mm [252, 256, 257]. The distance between the excitation electrode and the reflection electrode (d_R) is designed to be $\lambda/8$ = 51.8 μm. The number of excitation electrode pairs (N_O) is 20 and the number of the reflector electrodes (N_R) is 32. There are two input channels on the SAWN chip so that the SAWN chip can be operated with both progressive mode and standing wave mode. The input power can be adjusted accordingly through the commercial driving power supply.

Fig. 5.2 (b) and (c) show two typical designs of the ARC patterns on the SAWN chip surface. The droplet can be transported in parallel with the SAW transport direction or at an angle. In Fig. 5.2 (c), the two side ARC tracks have a 45° angle compared to the center ARC track. Hydrophilic curved rungs (trimethylsilanol, TMS) were patterned on a hydrophobic Cytop coating. As for the ARC patterns, the rung period pitch (P) is 50 μm, the hydrophilic line width (w) is 10 μm, and the ARC track width (W_{ARC}) is 500 μm. We designed a hydrophilic circle at the center of the chip for droplet merging or nebulization operation. The diameter of the central hydrophilic circle (D) is 1000 μm.

A droplet on the SAW platform with hydrophobic coating can go through periodic distortion due to SAW acoustic pressure [258]. As modulated, the water droplet wets the ratchet patterns along the rungs, creating an air-water-solid three-phase contact line (TPL) along its outer edge. We denoted the portion of the water droplet edge that aligns with the rung curvature, which has a mostly continuous TPL, as the leading edge of the droplet, while the other portion, which has only intermittent TPLs across different rungs, is called the trailing edge of the droplet. The leading edge of the droplet provides a higher pinning force than the trailing edge as the water droplet expands and recesses on the hydrophobic-hydrophilic boundary of the ARC patterns. This asymmetry in pinning forces causes water droplets to move toward the direction of the rung curvature [218].

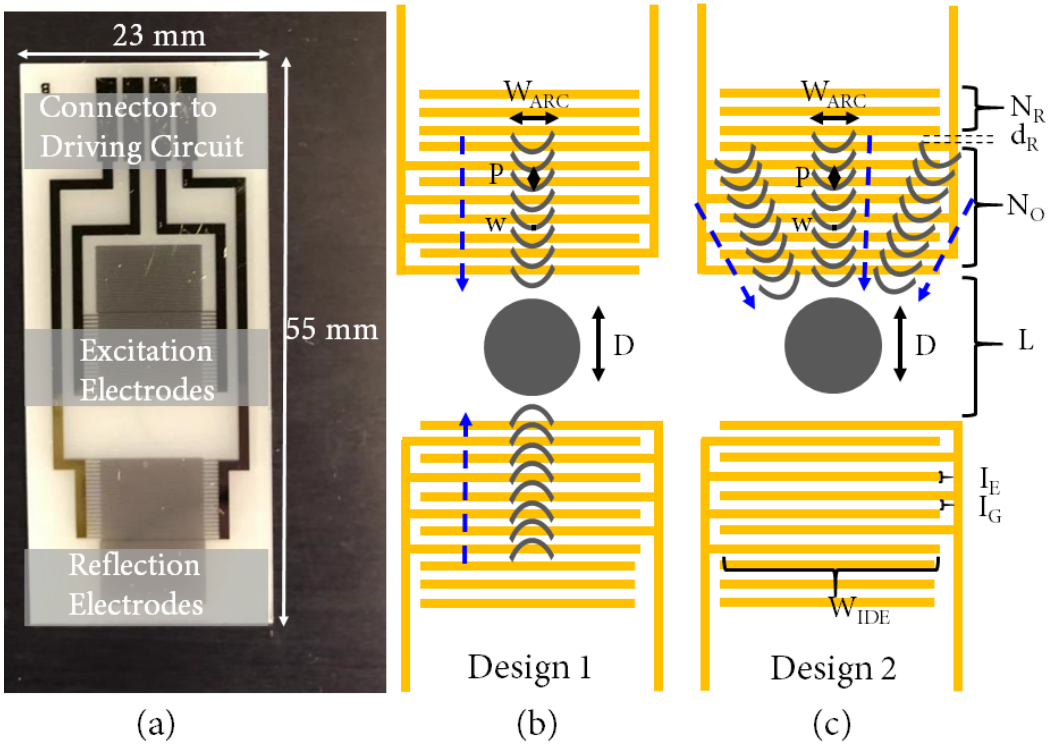

Figure 5.2. SAWN platform setup with ARC. (a) Top view of the SAWN chip after dicing. (b) and (c) SAWN platform setup with ARC. Two designs of the ARC patterns for droplet movement control. Dotted blue arrows indicate the droplet movement direction. The grey arc-shaped rungs and center circle patterns are hydrophilic regions, treated with TMS. The other regions of the SAWN chip are covered with Cytop.

5.3 FABRICATION PROCESS

The fabrication process is shown in Fig. 5.3. To fabricate the SAWN device, we used a 3-inch single side polished 128° YX-cut $LiNbO_3$ substrate. The wafer was first cleaned to remove any contaminants or dust that could affect the spun layer of the resist. IDEs were patterned on the polished side by a standard lithography process. Cr and Au layer electrodes were deposited via an e-beam evaporator and the substrate was soaked in acetone for photoresist lift-off. The wafer was cut into individual SAWN chips before further testing.

To create Cytop-TMS patterns on the SAWN surface, we utilized Parylene C as a stencil mask [218]. Direct spin coating of photoresist could not form a uniform layer on top of the hydrophobic Cytop surface. Diluted Cytop (Asashi Glass Co. Ltd) solution (Cytop : CT solv180 = 1:3) was spin-coated and baked at 180 °C for 1 hour with a final thickness of ~70 nm. Then a 2.5 μm Parylene C film was evaporated on the Cytop using a commercial parylene coater (PDS 2010, Specialty Coating Systems, Inc.) under vacuum. 6 μm photoresist (AZ9260, MicroChemicals GmbH) was spin coated on Parylene C and directly exposed with a Heidelberg-MicroPG-101 mask writer (Heidelberg Instruments Mikrotechnik GmbH). The photoresist was developed with AZ400K photoresist developer (AZ400K : DI water = 1:4) for 3 min. Then the exposed Parylene C regions were etched with O_2 plasma using a reactive ion etching process (Vision 320 RIE Mark II, Advance Vacuum, Inc). Both the patterned Parylene C and the Cytop underneath were etched with this process. The Parylene C mask was carefully peeled off from the substrate with tweezers. A spin-on TMS layer (MP-P20, ShinEtsu MicroSi, Inc.) was deposited on the Cytop openings followed by baking on a hotplate for 2 min.

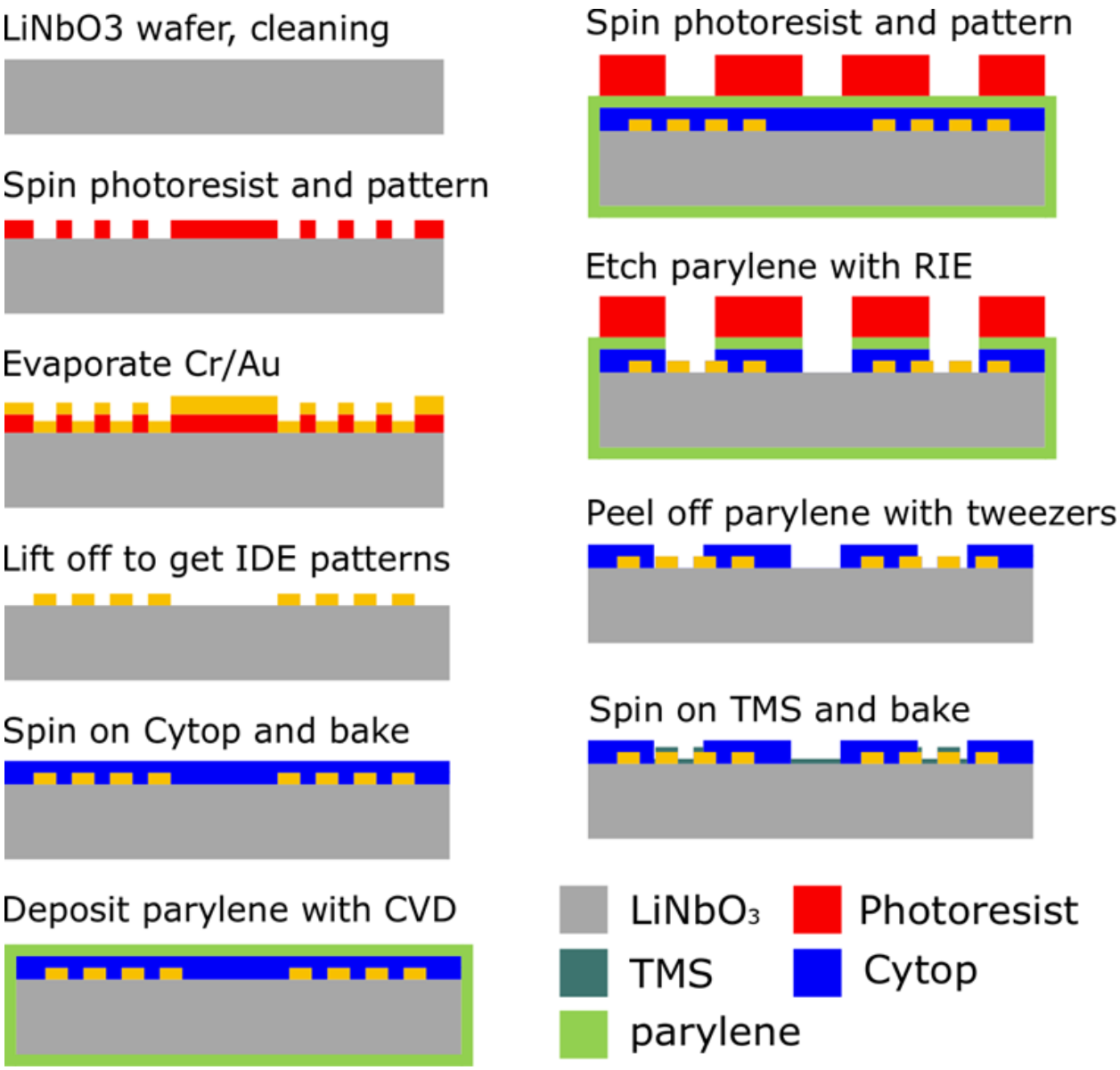

Figure 5.3. The fabrication process of the SAWN platform with ARC patterns. Parylene C is used as the stencil mask without degrading the Cytop hydrophobicity after being peeled off.

5.4 Experimental Setup

The experimental setup is shown in Fig. 5.4. Both progressive wave surface acoustic wave nebulization (PW-SAWN) and standing wave surface acoustic wave nebulization (SW-SAWN) modes can be generated by a commercial power supply (Deurion LLC), outputting a SAW wave

at 9.56 MHz. A water droplet was pipetted, and the droplet silhouette was monitored by a high-speed camera (FASTCAM Mini UX100, Photron Inc.) with a sampling rate of 1000 fps. The droplet position and contact angle change with time were analyzed with our MATLAB/Python custom code. The droplet static contact angle was analyzed with ImageJ software. The droplet sliding angle was characterized by a custom-made tilting stage. The inclination angle was measured with a triple-axis accelerometer (MMA8451, Adafruit, Inc.). The size of the tiny drops after nebulization was measured by an aerodynamic particle sizer spectrometer (APS Model 3321, TSI Incorporated). The aerosol flow was set to 1 L/min and the sheath flow was 4 L/min.

The mass spectrometry (MS) experiments were performed on a SYNAPT G2-Si high definition mass spectrometer (Waters Corp.). The SW-SAWN mode chip was mounted on a custom-made chip holder and placed close to the G2 MS inlet. The droplets on the SAWN chip surface containing dissolved analytes were nebulized into a plume of aerosolized drops as the SAW reached the liquid. The drops were sampled by SYNAPT's atmospheric pressure ionization (API) interface. Frequencies higher than the fundamental frequency were tested to nebulize the droplets. The nebulization frequencies were first selected based on the S-parameter measurements by the vector network analyser (8753D, Agilent Inc.). Then the frequency generator (N5181a, Agilent Inc.) was connected to two broadband (2 MHz – 700 MHz) RF power amplifiers on each channel of the SAWN chip.

We used MS standard Angiotensin II (ProteoMass, Sigma-Aldrich) dissolved in 0.1% acetic acid in water for the MS measurement. Different concentrations (1 μM and 100 nM) of the analyte solution were tested.

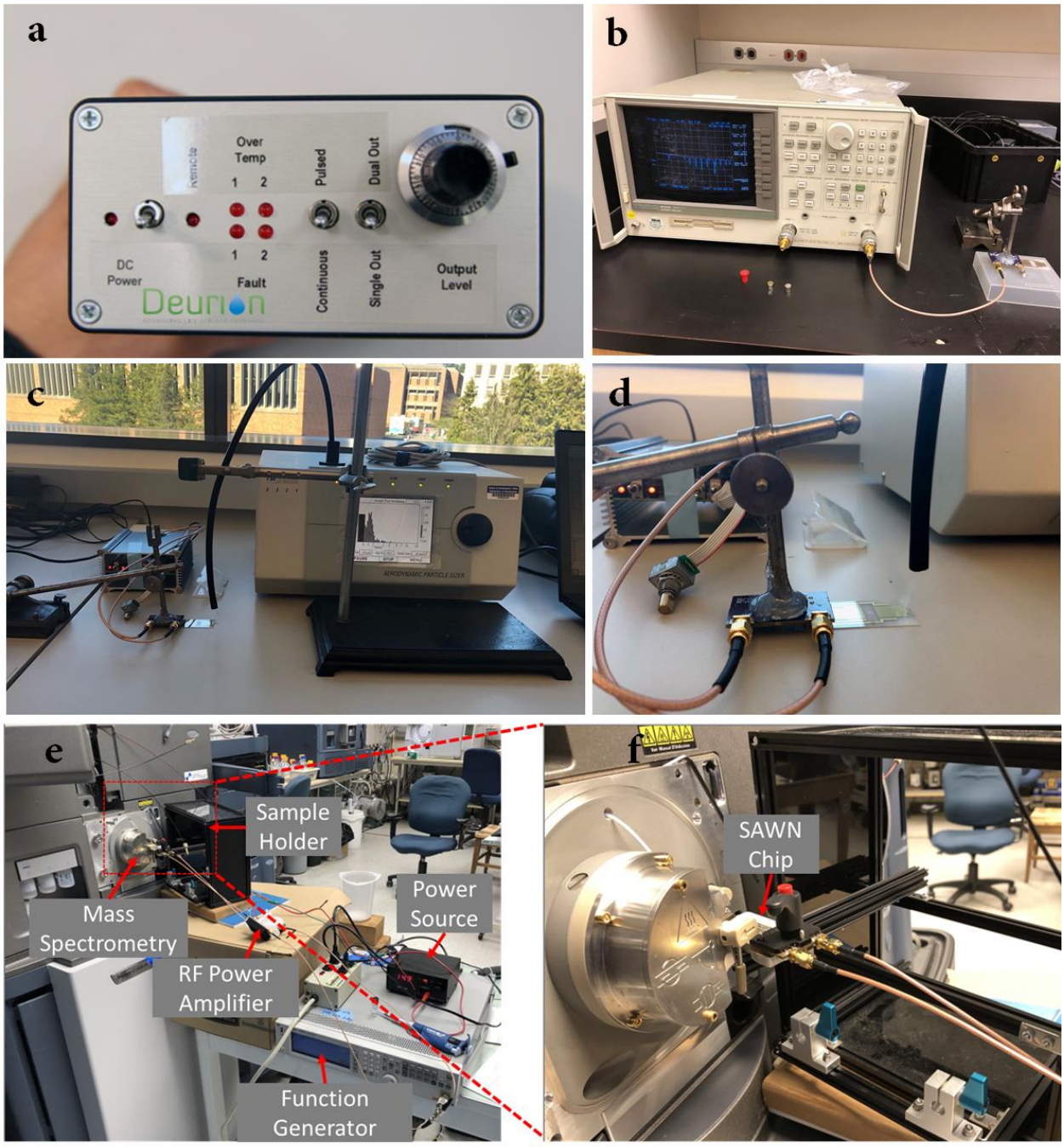

Figure 5.4. (a) Deurion SAWN power supply. (b) S parameter measurement setup. (c) Droplet size distribution measurement with aerodynamic particle sizer spectrometer. (d) Droplet nebulization and size distribution measurement.

5.5 CHARACTERIZATION RESULTS

5.5.1 *Droplet Transport Characterization*

The ARC tracks were successfully patterned on the Cytop coated $LiNbO_3$ substrate (Fig. 5.5 (a)) and IDE electrodes (Fig. 5.5 (b)). We characterized the Cytop surface properties by comparing the static contact angle (CA) and sliding angle (SA) of the as-deposited Cytop surface and the Cytop surface after patterning with Parylene C. 10 μL water droplets were used to characterize CA and 15 μL droplets were used for SA. Each analysis result was generated from 3 water droplets at different substrate locations.

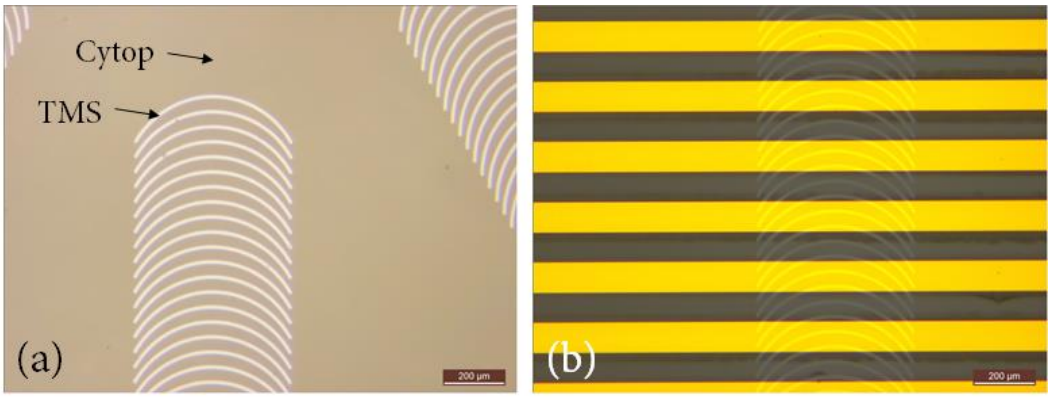

Figure 5.5. Finished ARC patterns on top of the (a) $LiNbO_3$ substrate surface and (b) Cr/Au metal electrodes region.

We operated the SAWN chip in standing wave mode for the droplet delivery and the nebulization characterizations. Compared with PW-SAWN, SW-SAWN provides a gain of 10^2-fold to 10^3-fold in ion intensity for peptides with smaller nebulized drop size [250, 259]. When the SAW power was turned on, the droplet was first distorted by the acoustic pressure and elongated vertically. Then the droplet restored its shape and wetted the surface. The distortion and restoration of the droplet were periodic, monitored by the high-speed camera. The leading and

trailing edge of the droplet then periodically wetted and dewetted along the ARC patterns to create an anisotropic pinning force. As shown in Fig. 5.6 (a), a 3 μL droplet was transported at about 9 W input power. The leading edge expanded at 0.60 mm ± 0.09 mm and recessed at 0.26 mm ± 0.13 mm during each oscillation cycle, while the trailing edge expanded at 0.31 mm ± 0.11 mm and recessed at 0.65 mm ± 0.14 mm. The droplet transported at an average speed of 20 mm/s. The periodicity of the droplet behavior was observed at ~16 ms (63 Hz) by analyzing the position change of the leading and trailing edge over time. The droplet ended up at the hydrophilic circle patterned on the center location of the SAWN chip and would nebulize if we increased the actuation power. Droplet silhouettes during a single oscillation cycle are shown in Fig. 5.6 (b). Fig. 5.6 (c) demonstrates the droplet merging and mixing function on the ARC designs shown in Fig. 5.2 (c). The operation was performed in an open environment without enclosed channels or top covers and without the need for complex control circuitry. Two colored droplets were pipetted on two ARC tracks and modulated by the SAW at the same time. The droplets moved to the central hydrophilic circle regions, where they were mixed with high-frequency SAW vibrations.

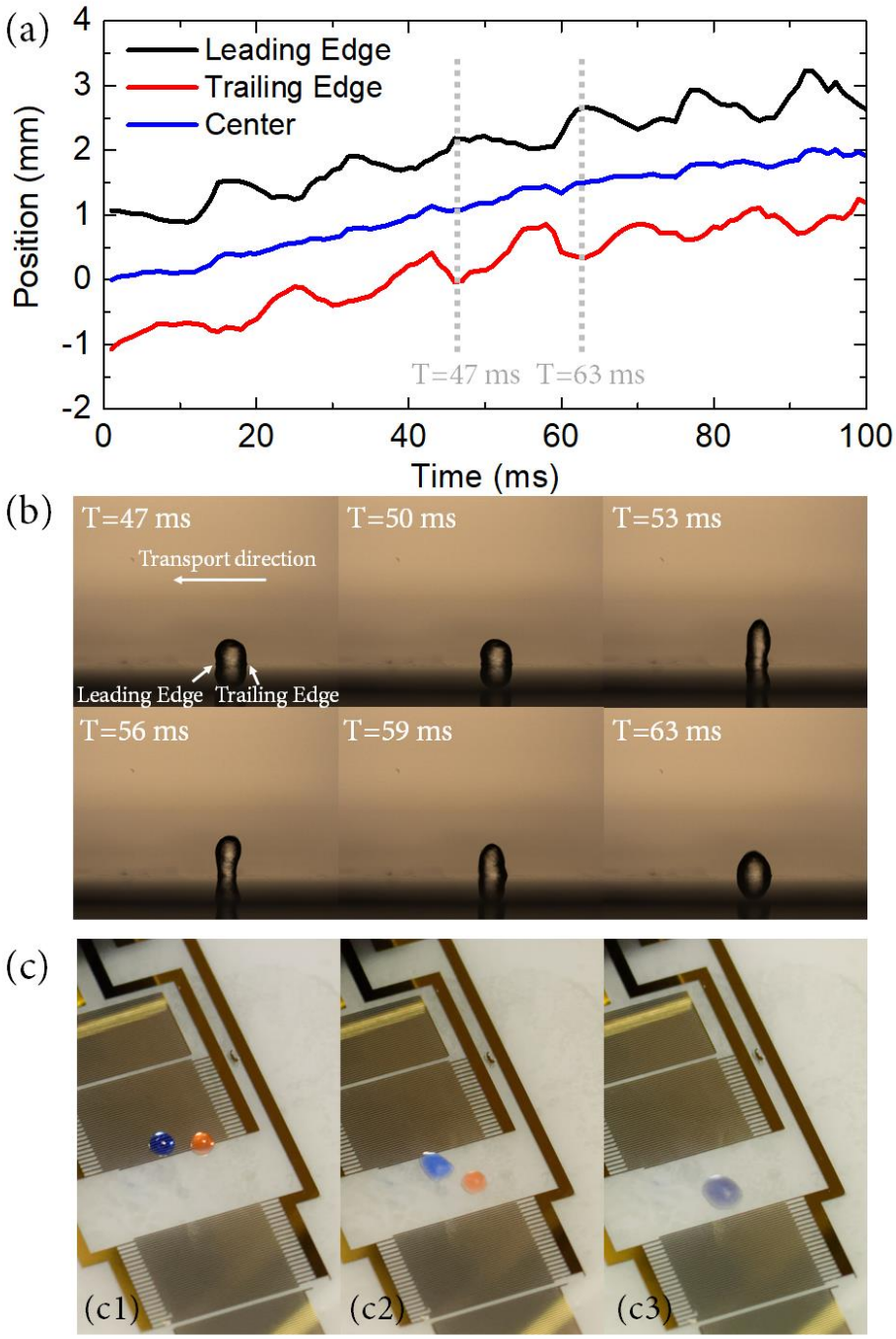

Figure 5.6. (a) Droplet edge position change with time, modulated by the SAWN power. The average transport speed can be estimated from the center position change over 100 ms sampling time. (b) High-speed camera capture of droplet silhouettes. (c) Droplets moving and merging operation on SAWN platform with ARC tracks. (c1) Placement of colored droplets (blue and orange) on the two ARC tracks. (c2) Droplets moving along ARC actuated by SAW. (c3) Droplets stopping, merging, and mixing at the central hydrophilic nebulization region.

To describe the periodic oscillation of the droplet more precisely under the SAW field, we tracked the droplet width and height change with time. As shown in Fig. 5.7 (a), the droplet started as a semi-spherical shape on the SAWN chip surface (step I). It then started to elongate vertically (step II) and reach the maximum distortion in height (step III). Then the droplet recessed (step IV) and expanded slightly along the horizontal direction, wider than the original droplet width before the droplet completely restored its initial hemispherical shape to complete the cyclical distortion (step I). We denoted the droplet initial width as w_{drop0} and the droplet initial height as h_{drop0}. The normalized droplet width and height changes with time compared to the initial value are shown in Fig. 5.7 (b). We found that the cyclical distortion frequency was related to the droplet size, demonstrated in Fig. 5.7 (c). As the droplet volume decreased, the droplet cycled through the distortion phase and restoration phase faster. We tested the minimum required power to transport the droplet by slowly increasing the input power until a droplet movement was observed and recorded the average droplet movement speed at this input power, shown in Fig. 5.7 (d). The minimum power required to initiate droplet movement decreased as the droplet size increased. All the droplets tested (0.5 – 4 μL) were able to overcome the surface friction or contact angle hysteresis and were transported by SAW within the available power supply rating. The droplet transport speed was characterized by the input power of 15 W.

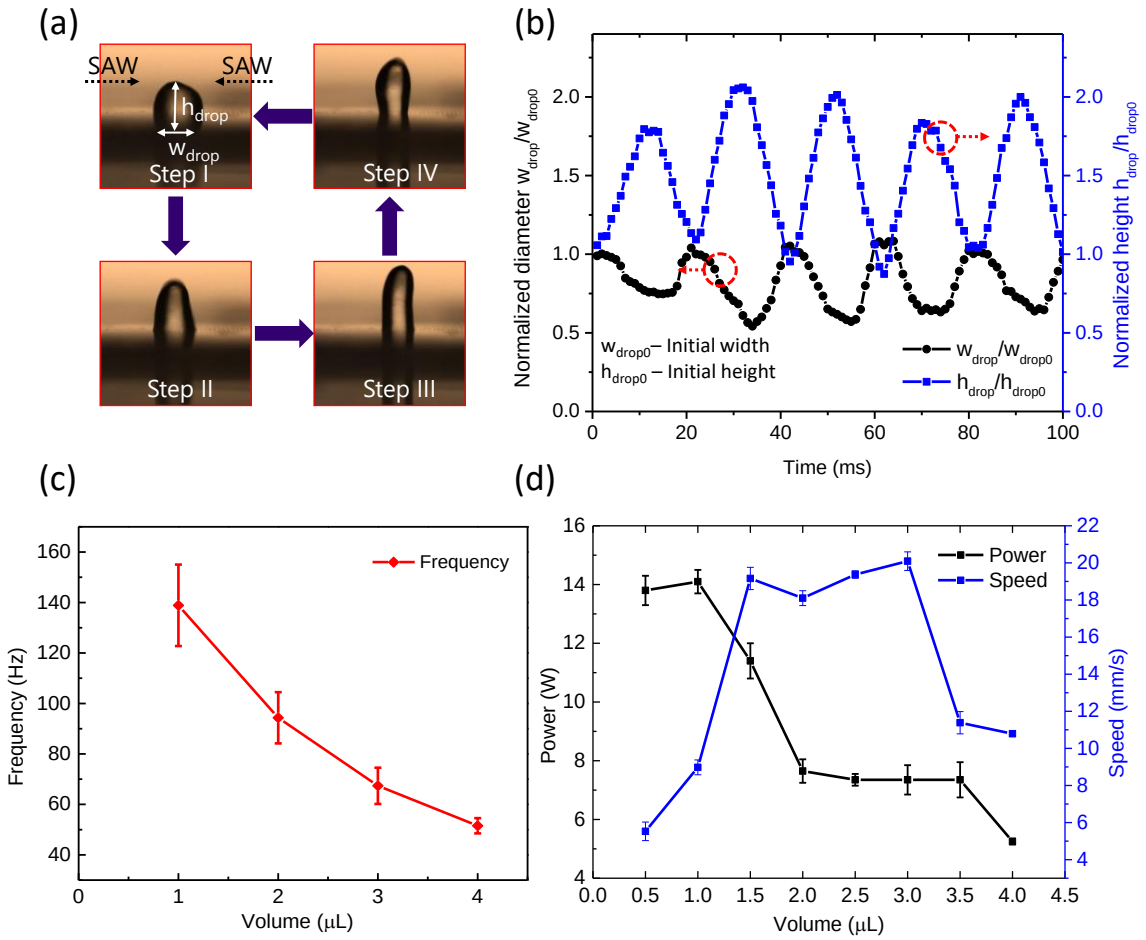

Figure 5.7. (a) Steps of the periodical droplet distortion under SAW actuation. (b) Normalized droplet width and height change with time as the droplet moved on the ARC track. The droplet size in this plot was 3 μL. (c) Characterized periodical distortion frequencies for different volumes of the droplet. Data is shown ± one standard deviation for n = 3. (d) Minimum power required to transport the droplet sitting on the ARC track by SAW and the droplet transport speed with the same input SAWN power. The droplet volumes ranged from 0.5 to 4 μL. Data is shown ± one standard deviation for n = 3.

5.5.2 *Droplet Nebulization Characterization*

We further conducted the SAWN chip nebulization tests without the ARC coatings. Fig. 5.8 (a) demonstrates a successful nebulization process as the SAWN chip converted the bulk water droplet on top to a plume of fine drops. When the SAW met a liquid medium along its path, the

leakage of the SAW from the substrate into the droplet caused internal liquid streaming and free capillary waves on the droplet surface [260]. When the power was high enough, the capillary waves at the droplet surface caused droplet pinch-offs [261]. Thus, a mist of aerosolized droplets overcame the capillary adhesion and jetted. The height of the aerosolized droplets plume could grow higher than 30 cm, providing a wide operating range when interfacing with the MS inlet. Besides the fundamental resonance frequency, we also tested the SAWN chip to nebulize at higher harmonic frequencies. The tested frequencies were picked from the S11 measurement results, where a dip in the S11 curve demonstrated a strong coupling between the input AC voltage and mechanical SAW propagation. The nebulization capabilities at the fundamental resonance frequency and the higher-order resonance frequencies are shown in Fig. 5.8 (b). It is interesting to note that the droplet cannot be nebulized or had an extremely weak nebulization process at the harmonics of the fundamental resonance frequency (19.8944 MHz and 30.4147 MHz). At higher frequencies (>38.2 MHz), the droplet could not be nebulized even though there was a strong dip in the signal from the S11 curve, which could have been caused by the phase mismatch and the energy loss at the connectors.

We further characterized the nebulization time under ambient air environment (27 °C and 40% RH). For each of the measurements 2 μL water droplets were pipetted on the same spot of the SAWN chip. For consistency in the nebulization process, we waited for 2 min between each measurement to let the chip return to ambient room temperature. As shown in Fig. 5.8 (c), different nebulization rates can be observed under different frequency nodes, which provided a tuning capability when a slower nebulization rate was required. We then characterized the size distribution of the tiny nebulized drops with an aerodynamic particle sizer spectrometer, shown in Fig. 5.8 (d)-(f). In general, the SAWN chip was capable of nebulizing the water droplet into a

plume of extremely fine tiny drops. At 9.5603 MHz, finer drops were generated with a peak diameter at ~1.5 μm, while at both 23.1587 MHz and 26.9651 MHz, the aerosolized drops had similar peaks at ~3.5 μm.

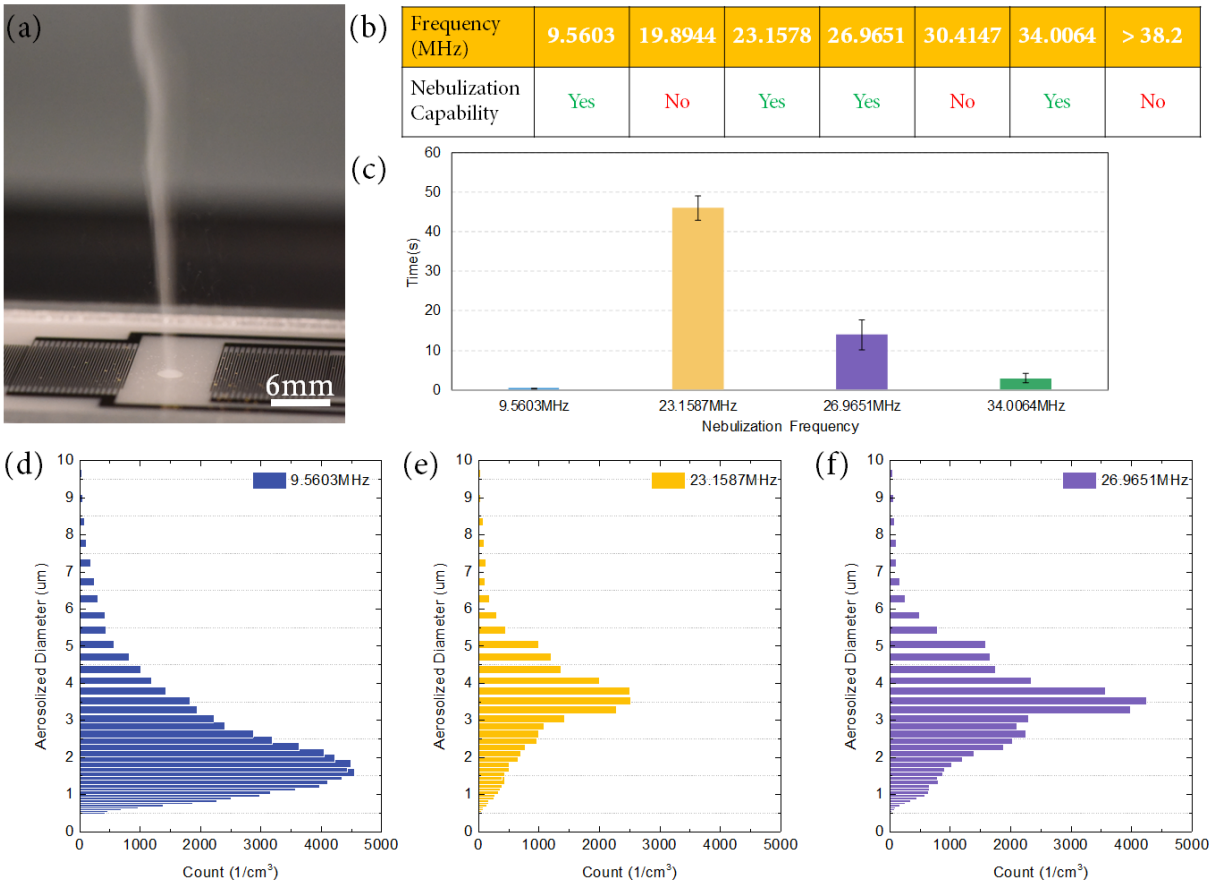

Figure 5.8 (a) Droplet nebulization on the SAWN chip surface at the fundamental resonance frequency. (b) Table of the SAWN chip nebulization capability under different input frequencies with the same input power. (c) Average time to completely nebulize a 2 μL water droplet. Data is shown ± one standard deviation for n = 5. (d)-(f) Aerosolized drops diameter distribution plot under selected SAWN frequencies by the aerodynamic particle sizer spectrometer. The bars demonstrate the aerosolized drop counts at each count median diameter (CMD) channel width. The measurement range was from 0.5 μm to 10 μm. A short inlet tube was selected and attached to the instrument to reduce the loss of aerosolized drops during the transport into the detection chamber and thus to improve the signal to noise ratio.

5.5.3 *Mass Spectrometry Measurement Results*

We then performed MS measurements with a standard test solution of Angiotensin II (*m*/*z* = 1046) in water with 0.1% formic acid. 1 μM and 100 nM of solutions were prepared. Fig. 5.9 shows examples of MS results at different nebulization frequencies. (a1), (b1) and (c1) show the single Angiotensin II nebulized ion current trace as a function of time. For different input frequencies, the MS results showed different ion intensities within varied time length. For example, the nebulization detection ended abruptly at 9.5603 MHz, but the MS detection process lasted for tens of seconds at 23.1578 MHz, proving that the nebulization rate could be controlled by the nebulization frequencies. From (a2), (b2) and (c2), signature mass spectrums were generated successfully among all the frequencies with good signal to noise ratio. The SAWN generated the majority of $[M+2H]^{2+}$ ions. $[M+H]^{+}$ ions were also detected by the MS. Depending on the nebulization frequencies, the intensity varied around 20%~35% compared with a base peak at $[M+2H]^{2+}$.

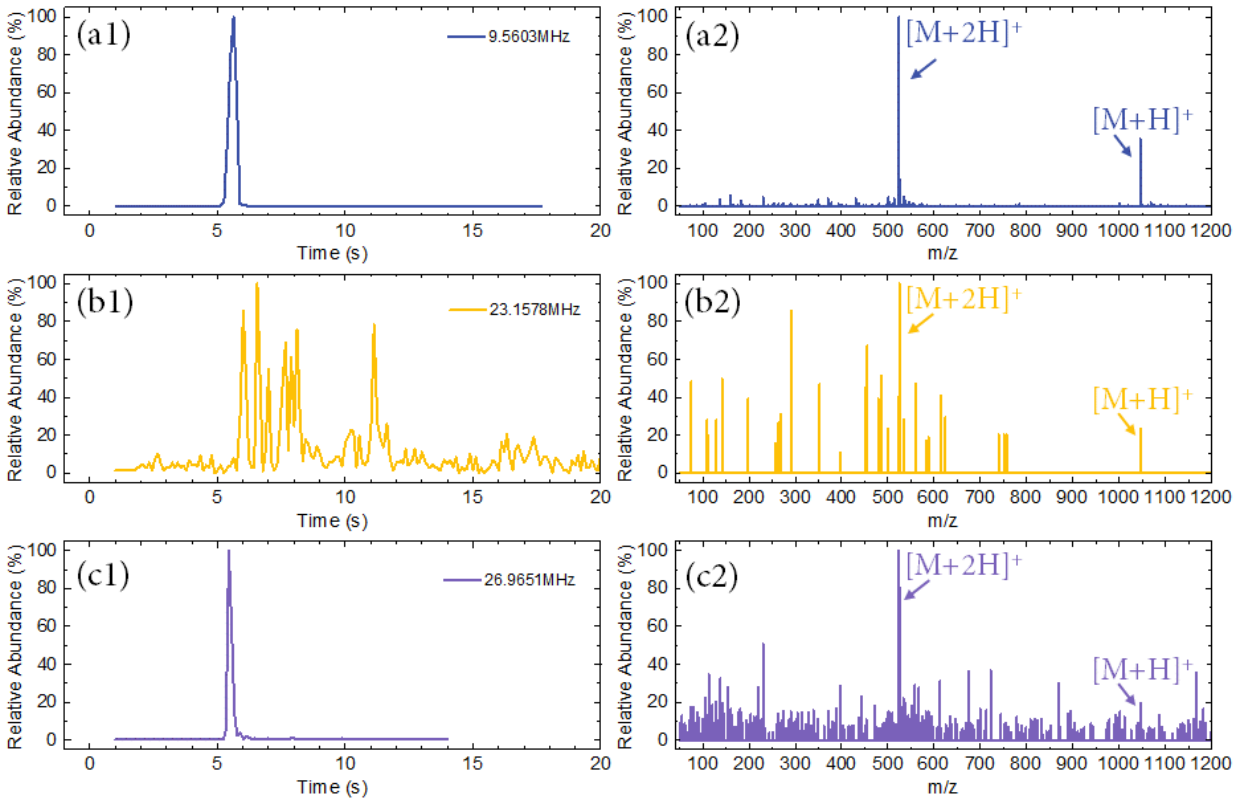

Figure 5.9. (a1), (b1) and (c1) show the Angiotensin relative ion current versus time detected by the MS. The maximum ion current abundance counts were measured 4.2×10^7 for (a1), 1.0×10^3 for (b1) and 3.0×10^5 for (c1). (a2), (b2) and (c2) show the detailed Angiotensin precursor ion mass spectra selected from the relative ion current. The highest relative ion abundance result was selected at the corresponding nebulization frequencies.

5.6 Simulation Results

5.6.1 *Piezoelectric Constitutive Equations and Coefficients*

Piezoelectricity is the ability of the materials to become electrically polarized when strained. From a microscopic point of view, within the crystal unit cell, the charged atoms will produce a net electric dipole due to the displacement by the external force. In certain crystal lattice structures, the combined crystal charge within all the unit cells will produce a macroscopic net electric polarization and surface charge. A reverse piezoelectric effect also exists when an electric field is

applied. Piezoelectricity is a cross-coupling between mechanical and electrical stress. The describing piezoelectric constitutive equations can be written in two ways: the strain-charge form or the stress-charge form [262]. Different material property matrixes are required for each of the equation formats.

The strain-charge form can be written as:

$$\vec{S} = \overrightarrow{s_E} \cdot \vec{T} + \vec{d}^T \cdot \vec{E} \tag{5-1}$$

$$\vec{D} = \vec{d} \cdot \vec{T} + \vec{\varepsilon} \cdot \vec{E} \tag{5-2}$$

where $\vec{S}$ is the strain (m/m), $\vec{T}$ is the stress (N/m^2), $\vec{D}$ is the electric displacement (C/m^2), $\vec{E}$ is the electrical field (V/m), s_E is the elastic compliance coefficient (m^2/N), $\vec{d}$ is the piezoelectric stress coefficient (C/N) and ε is dielectric constant (F/m).

The stress-charge form can be written as:

$$\vec{T} = \overrightarrow{c_E} \cdot \vec{S} - \vec{e}^T \cdot \vec{E} \tag{5-3}$$

$$\vec{D} = \vec{e} \cdot \vec{S} + \vec{\varepsilon} \cdot \vec{E} \tag{5-4}$$

where $\overrightarrow{c_E}$ is the elastic stiffness coefficient (Pa) and $\vec{e}$ is the piezoelectric coefficient (C/m^2).

The strain-charge form is useful for analyzing actuators and the stress-charge form is useful to analyze vibration and waves [263]. We use the stress-charge form for our simulation. For our substrate material $LiNbO_3$, the matrix used can be expressed as:

Elastic stiffness matrix:

$$\overrightarrow{c_{EIJ}} = \begin{bmatrix} c_{E11} & c_{E12} & c_{E13} & c_{E14} & 0 & 0 \\ c_{E12} & c_{E11} & c_{E13} & -c_{E14} & 0 & 0 \\ c_{E13} & c_{E13} & c_{E33} & 0 & 0 & 0 \\ c_{E14} & -c_{E14} & 0 & c_{E44} & 0 & 0 \\ 0 & 0 & 0 & 0 & c_{E44} & c_{E14} \\ 0 & 0 & 0 & 0 & c_{E14} & c_{E66} = \dfrac{c_{E11} - c_{E12}}{2} \end{bmatrix}$$

Piezoelectric matrix:

$$\overrightarrow{e_{ij}} = \begin{bmatrix} 0 & 0 & 0 & 0 & e_{15} & -e_{22} \\ -e_{22} & e_{22} & 0 & e_{15} & 0 & 0 \\ e_{31} & e_{31} & e_{33} & 0 & 0 & 0 \end{bmatrix}$$

Dielectric matrix:

$$\overrightarrow{\varepsilon_{ij}} = \begin{bmatrix} \varepsilon_{11} & 0 & 0 \\ 0 & \varepsilon_{11} & 0 \\ 0 & 0 & \varepsilon_{33} \end{bmatrix}$$

The coefficient of $LiNbO_3$ used for the simulation is from the reference [264], shown in the table below:

Table 5.1 Elastic Stiffness Coefficient (GPa)

C_{11}	C_{12}	C_{13}	C_{14}	C_{33}	C_{44}
199	53.8	71.4	7.85	237.2	60.1

Table 5.2 Piezoelectric Coefficient (C/m^2)

e_{15}	e_{22}	e_{31}	e_{33}
3.65	2.39	0.31	1.72

Table 5.3 Dielectric Constant (pF/m^2)

ε_{11}	ε_{33}
398.9	232.2

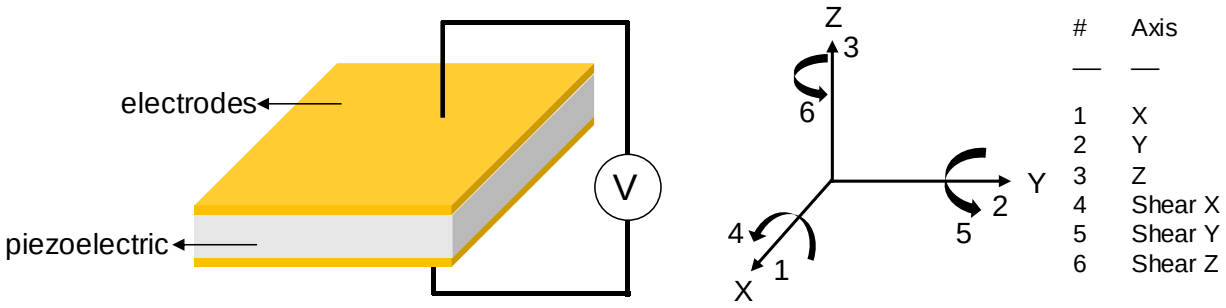

Figure 5.10. Schematic of the piezoelectric materials and axes notations. Numbers are used rather than letters. 1, 2, 3 corresponds to the X, Y, Z axis, respectively. 4, 5, 6 corresponds to the shear direction perpendicular to X, Y, Z axis [265].

5.6.2 *Crystal Cuts and Tensor Constants Transformation*

As a simulation basis, the XY plane is the device surface plane and the SAW is propagating along the X-axis. The Z-axis is perpendicular to the XY plane and the SAW propagating direction. The XYZ orientation follows the right-hand rule. In the absence of a user-defined coordinate system, the piezo crystal axis coincides with the global X_g, Y_g, and Z_g system (shown in the COMSOL Desktop geometry window). In practical applications, the $LiNbO_3$ is supplied in thin wafers with crystal cut at a particular angle concerning the crystallographic axes. Due to the anisotropy of the material properties, it is important to consider the relative rotation between the global coordinate system and the crystal cut surface while inputting the elastic stiffness coefficient matrix, piezoelectric coefficient matrix, and dielectric coefficient matrix values into the simulation model.

The details of the crystal cuts and COMSOL configuration have been discussed in detail in references [266] and [267, 268]. In commercially available $LiNbO_3$ products, notations like "X-cut" or "YX 128°" are often used. According to IEEE1978 standards, a virtual reference rectangular slice through the crystal is used to define the final orientation of the cut surface. The crystal axes are denoted as X, Y, and Z, and the reference rectangular plate is defined as having dimensions of length (l), width (w), and thickness (t). We use l, w, t to denote the orthogonal coordinate axes in the reference rectangular plate. An example of the rotational notation is demonstrated in the following [269]:

$$(\mathrm{YXlwt})\phi/\theta/\psi$$

The notation means that the initial reference rectangular plate thickness t is along the Y-axis and the length l is along the X-axis, respectively. The first rotation ϕ is about the l axis, the second rotation θ is about the w axis and the third rotation ψ is about the t axis. If the angle value is

positive, then the rotation about the axes is in a right-handed convention. An example of AT-cut quartz crystal is shown in Fig. 5.11 below.

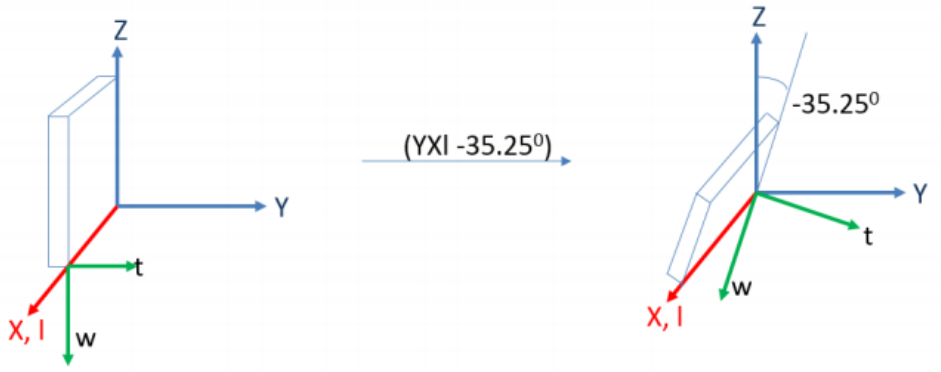

Figure 5.11. Definition of the AT-cut of quartz within the IEEE 1978 standard [270].

In the previous commercially available product notations, "X-cut" means the virtual rectangular reference plate is perpendicular to X-axis, and "YX 128°" means the reference plate is first perpendicular to the Y-axis and then rotated around the X-axis by 128°. In our simulation, we adopt full crystal cut notation according to IEEE1978 standards. The LiNbO3 substrate is (XYl)128° cut. The rotation sequence is demonstrated in Fig. 5.12. It is also important to mention that the final global axes (X_g, Y_g, and Z_g) in the COMSOL simulation match with the l, w, and t axes of the reference plate after the cut.

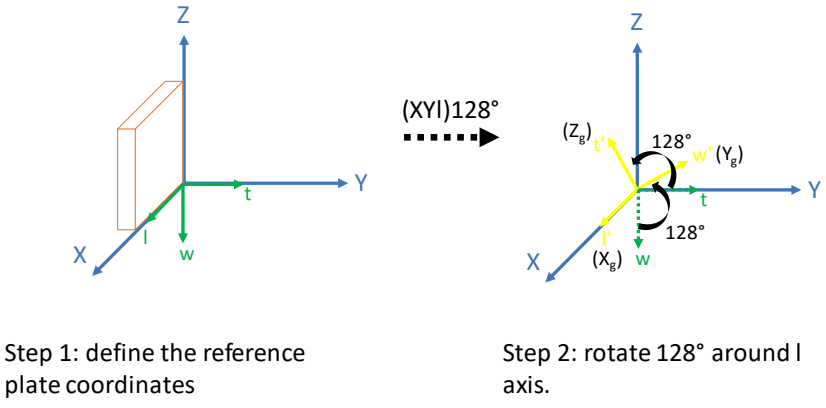

Figure 5.12. Rotation of $LiNbO_3$ reference plate coordinates after cuts.

In the next step, we need to consider how the material properties matrix will change in terms of the relative rotations between the crystal coordinates (X, Y, and Z) and global coordinates (X_g, Y_g, and Z_g). To match these two coordinates, crystal coordinates need to be rotated according to Euler angles, which is different from the crystal cuts notations. Euler angle is typically denoted as α, β, and γ and follows the Z-X-Z convention. This means (shown in Fig. 5.13) the X-Y-Z frame rotates three times: first rotation is about Z-axis by an angle α. Then second rotation is about the new X'-axis by an angle β. The third rotation is about the newest Z''-axis by an angle γ. Using this convention, we can derive that the Euler angle required for the (XYl)128° cut $LiNbO_3$ substrate is (0°,38°,0°). The crystal coordinates X-Y-Z will be coplanar with the global coordinates X_g-Y_g-Z_g in Fig. 5.12. The calculated Euler angle also matches with the values in the [271].

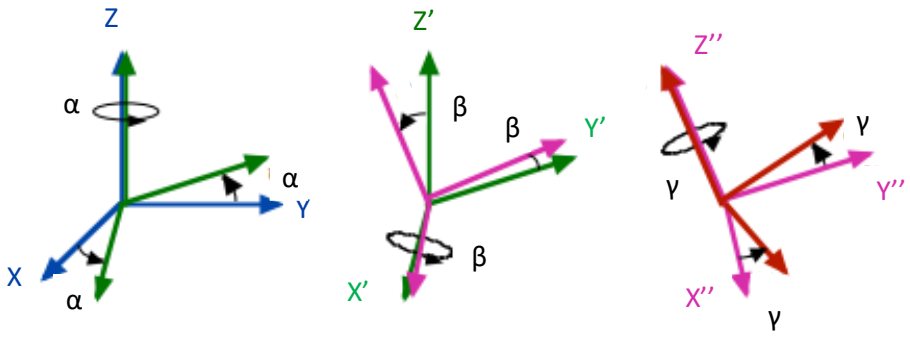

Figure 5.13. Euler angle notation

By knowing the Euler angle of the rotated crystal, we then calculate the new piezoelectric material property matrixes using the methods in [272]. Two rotational matrices $\vec{V}$ and $\vec{Q}$ were introduced as:

$$\vec{V} = \begin{bmatrix} \cos\gamma\cos\alpha - \cos\beta\sin\alpha\sin\gamma & \cos\gamma\sin\beta + \cos\beta\cos\alpha\sin\gamma & \sin\gamma\sin\beta \\ -\sin\gamma\cos\beta - \cos\beta\sin\alpha\cos\gamma & -\sin\gamma\sin\alpha + \cos\beta\cos\alpha\cos\gamma & \cos\gamma\sin\beta \\ \sin\beta\sin\gamma & -\sin\beta\cos\alpha & \cos\beta \end{bmatrix}$$

$$= \begin{bmatrix} a_1 & b_1 & c_1 \\ a_2 & b_2 & c_2 \\ a_3 & b_3 & c_3 \end{bmatrix}$$

$$\vec{Q} = \begin{bmatrix} a_1^2 & b_1^2 & c_1^2 & 2b_1c_1 & 2c_1a_1 & 2a_1b_1 \\ a_2^2 & b_2^2 & c_2^2 & 2b_2c_2 & 2c_2a_2 & 2a_2b_2 \\ a_3^2 & b_3^2 & c_3^2 & 2b_3c_3 & 2c_3a_3 & 2a_3b_3 \\ a_2a_3 & b_2b_3 & c_2c_3 & b_2c_3 + b_3c_2 & c_2a_3 + c_3a_2 & a_2b_3 + a_3b_2 \\ a_3a_1 & b_3b_1 & c_3c_1 & b_1c_3 + b_3c_1 & c_1a_3 + c_3a_1 & a_1b_3 + a_3b_1 \\ a_1a_2 & b_1b_2 & c_1c_2 & b_1c_2 + b_2c_1 & c_1a_2 + c_2a_1 & a_1b_2 + a_2b_1 \end{bmatrix}$$

Then the new set of material constant matrices ($\overrightarrow{c_E'}$, $\overrightarrow{e'}$ and $\overrightarrow{\epsilon'}$) after the rotation of its original crystal coordinates (X, Y, and Z) can be calculated as:

$$\overrightarrow{c_E'} = \vec{Q}\overrightarrow{c_E}\overrightarrow{Q^t} \tag{5-5}$$

$$\overrightarrow{e'} = \vec{V}\vec{e}\overrightarrow{Q^t} \tag{5-6}$$

$$\overrightarrow{\epsilon'} = \vec{V}\vec{\varepsilon}\overrightarrow{V^t} \tag{5-7}$$

By inserting the Euler angle (0°,38°,0°), the material constant matrices used in the simulation are shown below. The Python program used for calculation is attached in the Appendix.

Elastic stiffness matrix (GPa):

$$\overrightarrow{c_{EIJ}} = \begin{bmatrix} 199 & 68.1 & 57.1 & 10.4 & 0 & 0 \\ 68.1 & 191.5 & 85.7 & 8.7 & 0 & 0 \\ 57.1 & 85.7 & 216.0 & 8.0 & 0 & 0 \\ 10.4 & 8.7 & 8.0 & 74.4 & 0 & 0 \\ 0 & 0 & 0 & 0 & 57.2 & -4.2 \\ 0 & 0 & 0 & 0 & -4.2 & 75.5 \end{bmatrix}$$

Piezoelectric matrix (C/m^2):

$$\overrightarrow{e_{IJ}} = \begin{bmatrix} 0 & 0 & 0 & 0 & 3.7 & -2.5 \\ -2.5 & 2.5 & 0 & 3.7 & 0 & 0 \\ 0.2 & 0.2 & 1.3 & 0 & 0 & 0 \end{bmatrix}$$

Dielectric matrix (pF/m^2):

$$\overrightarrow{\varepsilon_{ij}} = \begin{bmatrix} 44.3 & 0 & 0 \\ 0 & 38.0 & -8.1 \\ 0 & -8.1 & 34.0 \end{bmatrix}$$

5.6.3 *COMSOL Simulation Setup*

We use the COMSOL Piezoelectric Devices module and Eigenfrequency Study function. The Eigenfrequency study is used to compute the eigenmodes and eigenfrequencies of a linear or linearized model. In acoustics, the eigenfrequencies correspond to the resonant frequencies and the eigenmodes correspond to the normalized acoustic field at the eigenfrequencies. For the boundary conditions (shown in Fig. 5.14), both mechanical and electrical conditions needed to be applied. The simulation cell thickness needs to be large enough to prevent any reflections from the lower boundary. Periodic boundary conditions are applied to the left and right vertical boundaries of the simulation cell for both mechanical and electrical simulation setup.

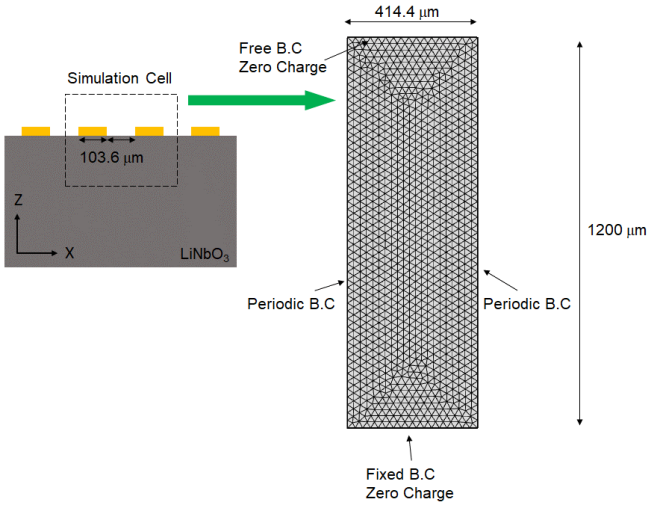

Figure 5.14. Simulation cell dimension and boundary condition setup after meshing. The 2D simulation is configured on the XZ plane. The SAW propagating direction is along the X-axis.

5.6.4 *Simulation Results*

The S11 measurement results and the simulation results are shown in Fig. 5.15. The estimated SAW propagating speed is 3960 m/s, meaning the first resonance frequency of the device is at 9.55 MHz. The S11 measurement showed a dip at around 9.52 MHz, meaning a better coupling of the electrical signal into the mechanical surface waves at the resonance frequency. The simulation results showed both longitudinal and transverse wave modes of the SAW wave.

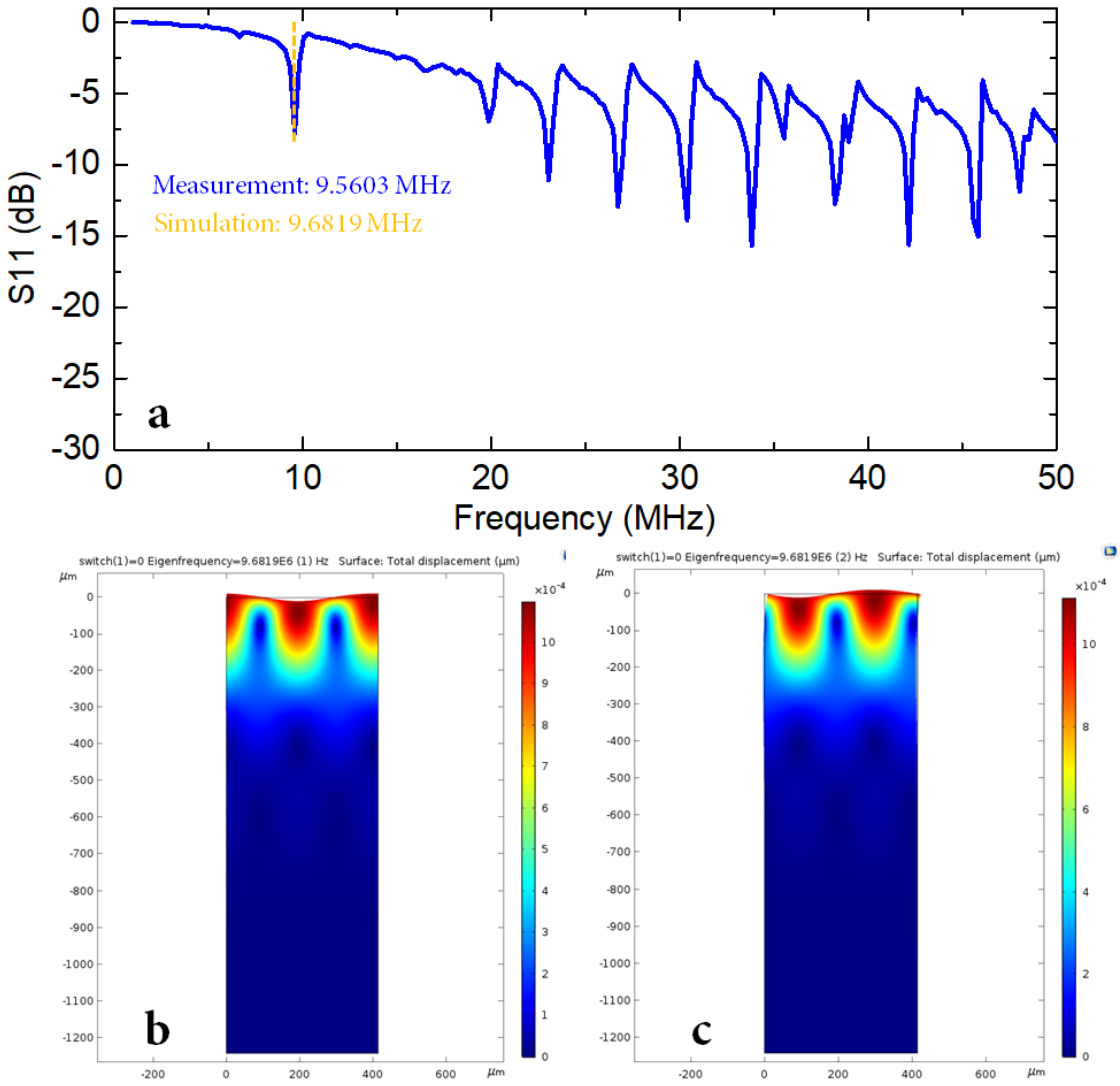

Figure 5.15. (a) S11 experimental measurement results. The frequency span is between 300 kHz and 30 MHz. (b) and (c) are simulation results of SAW modes at eigenfrequency, which are longitudinal mode and transverse mode, respectively.

5.7 CONCLUSION

In this chapter, we present an integrated SAWN chip to perform droplet transport, merging, mixing, and nebulization with ARCs and SW-SAWN. The innovations include: 1) only two input ports were required to realize multiple lab-on-chip functions without complex control circuitry as compared with other technologies like EWOD; 2) the droplet could be manipulated on top of the SAWN chip in an open environment, without the need of an enclosed flow channel or top cover; 3) hydrophilic patterns were successfully created on the hydrophobic thin film with the aid of a Parylene C stencil mask; 4) nebulization was controlled at multiple resonance frequency nodes with the same IDE spacing design. We characterized the change of the droplet transport leading and trailing edge positions with time, self-resonance frequency transport speed, and minimum power requirement, and we performed MS measurements at different nebulization frequencies. The results demonstrated that our SAWN platform has great potential to serve as an integrated lab-on-chip platform for proteomics.

Chapter 6. SUMMARY OF DOCTORAL RESEARCH AND RECOMMENDATIONS FOR FUTURE WORK

Throughout this thesis, we have explored several droplet manipulation approaches with the aid of anisotropic ratchet conveyors (ARCs), aiming to create active self-cleaning surfaces and lab-on-chip systems. We started with developing the theoretical groundwork of the anisotropic force acting on a droplet on the ARC tracks. We utilized the theoretical model as a design guide for different applications and droplet size requirements. To create the ARC pattern, we developed suitable microfabrication processes, including using Parylene C stencil mask methods that avoid the degradation of the hydrophobic material surface properties.

After building the theoretical fundamentals, fabrication approaches, and test bench setups, we first developed an active self-cleaning surface system using ARCs and orthogonal vibrations. Water droplet transport characteristics, including anisotropic driving force, droplet resonance mode, cleaning mechanisms, and system power consumption, were studied with the help of a high-speed camera and custom-made test benches. The droplet can be transported on the ARC surface at a speed of 27 mm/s and can clean a variety of dust particles, either water-soluble or insoluble. The optical transmission was measured to show that Cytop can improve transmittance by 2.5~3.5% over the entire visible wavelength range. Real-time demonstrations of droplet transport and surface cleaning were performed, in which the solar modules achieved a 23 percentage-point gain after cleaning.

Secondly, we built microfluidic devices on an open surface in air using electrowetting-on-dielectric (EWOD) with anisotropic ratchet conveyors (ARCs). While the traditional EWOD platform requires the control of multiple electrodes to transport the droplet, our system utilizes

only two controlling electrodes. We demonstrate that 15 μL water droplets are transported at a speed of 13 mm/s under 60 V_{peak} sinusoid AC signal at 50 Hz. Droplet transport at 20 Hz is also presented, demonstrating that the system can operate within a range of frequencies. Compared with vibration systems, the EWOD system enables all-terrain droplet actuation (ATDA) capabilities with reduced input power requirements.

Thirdly, we explore the droplet super-spreading and directional transport device using anisotropic ratchet conveyors (ARCs) and liquid dielectrophoresis (L-DEP) to clear the fogging of surfaces. By modulating the L-DEP force with an electromagnetic relay, the droplet can be directionally transported on the ARC-patterned surface independently of the droplet self-resonance frequency. The system works with a broad range of droplet volumes between 2 μL and 20 μL. The droplet can be transported with the presence of a moisture layer on the surface, which is superior to systems that move the droplet by relying on the solid-liquid interfacial tension difference (like, *e.g.*, in an electro-wetting-on-dielectric (EWOD) system) since the moisture could block the solid-liquid interface and degrade the system ability to transport the droplet. This design also enables droplet manipulation in an open space configuration without a top cover plate, leading to a broad range of applications including self-cleaning surfaces and fog removal.

Lastly, we present a piezoelectric transducer for standing wave surface acoustic wave nebulization (SW-SAWN). The transducer atomizes the nonvolatile analytes of a bulk fluid in the ambient air and the aerosolized drops are sampled by mass spectrometry (MS) for detection. Furthermore, we integrate anisotropic ratchet conveyors (ARCs) on the SAWN transducer surfaces to automate the sample preparation and droplet delivery process. MS measurements with the SAWN chip are performed under different input frequencies. The SAWN transducer can provide

a controllable nebulization rate by varying the input nebulization frequency while maintaining a reasonable signal to noise ratio for the MS detection.

We proved that ARCs are a robust system that can be adapted to various digital microfluidic platforms. The obstacles and challenges for self-cleaning surfaces currently involve coating durability and high cost in terms of scaling and mass production. The fine micro or nanostructures often cannot withstand the harsh outdoor environment for an extended period while the polymeric coating or surface infusion fluid will age and decay over time under solar radiation. The practical lifetime for a self-cleaning surface or system might only last from months to 1 or 2 years but the requirement is usually in the 10–20-year range, especially for applications in outdoor environments, for example in desert regions to reduce dust accumulation, or underwater to prevent biofouling on a ship hull. We need to strive for the creation of self-cleaning coatings for surfaces or systems with multiple merits including low cost, good scalability, durability, transparency, and antireflection. Similar challenges also influence the application of ARCs to lab-on-chip systems. It is also desirable to capture the condensation from air on the surface to generate droplets instead of dispensing from a reservoir or manual pipetting. As for the droplet condensation collection, we will explore the influence of IDE line width and gap size on the droplet manipulation and experiment with different ARC designs to transport and collect smaller droplets with less than 100 μm diameters. Our goal is to be able to perform self-cleaning and lab-on-chip tasks using water collected from condensation without the need for a dedicated water supply.

BIBLIOGRAPHY

[1] A. Nakajima, K. Hashimoto, T. Watanabe, K. Takai, G. Yamauchi, and A. Fujishima, "Transparent superhydrophobic thin films with self-cleaning properties," *Langmuir*, vol. 16, no. 17, pp. 7044-7047, 2000.

[2] Y. Paz, Z. Luo, L. Rabenberg, and A. Heller, "Photooxidative self-cleaning transparent titanium dioxide films on glass," *Journal of Materials Research*, vol. 10, no. 11, pp. 2842-2848, 1995.

[3] B. Bhushan and Y. C. Jung, "Natural and biomimetic artificial surfaces for superhydrophobicity, self-cleaning, low adhesion, and drag reduction," *Progress in Materials Science*, vol. 56, no. 1, pp. 1-108, 2011.

[4] R. Blossey, "Self-cleaning surfaces—virtual realities," *Nature materials*, vol. 2, no. 5, p. 301, 2003.

[5] P. Comanns *et al.*, "Directional, passive liquid transport: the Texas horned lizard as a model for a biomimetic 'liquid diode'," *Journal of the Royal Society Interface*, vol. 12, no. 109, p. 20150415, 2015.

[6] P. Comanns, F. J. Esser, P. H. Kappel, W. Baumgartner, J. Shaw, and P. C. Withers, "Adsorption and movement of water by skin of the Australian thorny devil (Agamidae: Moloch horridus)," *Royal Society open science*, vol. 4, no. 9, p. 170591, 2017.

[7] S. Nishimoto and B. Bhushan, "Bioinspired self-cleaning surfaces with superhydrophobicity, superoleophobicity, and superhydrophilicity," *Rsc Advances*, vol. 3, no. 3, pp. 671-690, 2013.

[8] K. S. Khalil, S. R. Mahmoudi, N. Abu-Dheir, and K. K. Varanasi, "Active surfaces: Ferrofluid-impregnated surfaces for active manipulation of droplets," *Applied physics letters*, vol. 105, no. 4, p. 041604, 2014.

[9] Y. Yuan and T. R. Lee, "Contact angle and wetting properties," in *Surface science techniques*: Springer, 2013, pp. 3-34.

[10] T. Young, "III. An essay on the cohesion of fluids," *Philosophical transactions of the royal society of London*, vol. 95, pp. 65-87, 1805.

[11] K.-Y. Law, "Definitions for hydrophilicity, hydrophobicity, and superhydrophobicity: getting the basics right," ed: ACS Publications, 2014.

[12] T. Nishino, M. Meguro, K. Nakamae, M. Matsushita, and Y. Ueda, "The lowest surface free energy based on− CF3 alignment," *Langmuir*, vol. 15, no. 13, pp. 4321-4323, 1999.

[13] R. W. Smithwick III and J. A. Boulet, "Vibrations of microscopic mercury droplets on glass," *Journal of colloid and interface science*, vol. 130, no. 2, pp. 588-596, 1989.

[14] J. S. Carr, "Studies of contact angles on oxidized copper minerals," 1948.

[15] D. Furlong and S. Hartland, "Wall effect in the determination of surface tension using a Wilhelmy plate," *Journal of Colloid and Interface Science*, vol. 71, no. 2, pp. 301-315, 1979.

[16] P. Weiss, "Wetting, spreading and adhesion, JF Padday, ed., academic, London, 1978, 498 pp. Price: $48.90," *Journal of Polymer Science: Polymer Letters Edition*, vol. 17, no. 7, pp. 463-464, 1979.

[17] A. Marmur, "Equilibrium contact angles: theory and measurement," *Colloids and Surfaces A: Physicochemical and Engineering Aspects,* vol. 116, no. 1-2, pp. 55-61, 1996.

[18] F. Restagno, C. Poulard, C. Cohen, L. Vagharchakian, and L. Léger, "Contact angle and contact angle hysteresis measurements using the capillary bridge technique," *Langmuir,* vol. 25, no. 18, pp. 11188-11196, 2009.

[19] L. Vagharchakian, F. Restagno, and L. Léger, "Capillary bridge formation and breakage: A test to characterize antiadhesive surfaces," *The Journal of Physical Chemistry B,* vol. 113, no. 12, pp. 3769-3775, 2008.

[20] M. G. Cabezas, A. Bateni, J. M. Montanero, and A. W. Neumann, "Determination of surface tension and contact angle from the shapes of axisymmetric fluid interfaces without use of apex coordinates," *Langmuir,* vol. 22, no. 24, pp. 10053-10060, 2006.

[21] P. Cheng, D. Li, L. Boruvka, Y. Rotenberg, and A. Neumann, "Automation of axisymmetric drop shape analysis for measurements of interfacial tensions and contact angles," *Colloids and Surfaces,* vol. 43, no. 2, pp. 151-167, 1990.

[22] O. Del Rıo and A. Neumann, "Axisymmetric drop shape analysis: computational methods for the measurement of interfacial properties from the shape and dimensions of pendant and sessile drops," *Journal of colloid and interface science,* vol. 196, no. 2, pp. 136-147, 1997.

[23] E. Moy *et al.*, "Measurement of contact angles from the maximum diameter of non-wetting drops by means of a modified axisymmetric drop shape analysis," *Colloids and surfaces,* vol. 58, no. 3, pp. 215-227, 1991.

[24] F. Skinner, Y. Rotenberg, and A. Neumann, "Contact angle measurements from the contact diameter of sessile drops by means of a modified axisymmetric drop shape analysis," *Journal of colloid and interface science,* vol. 130, no. 1, pp. 25-34, 1989.

[25] M. Cabezas, A. Bateni, J. Montanero, and A. Neumann, "A new method of image processing in the analysis of axisymmetric drop shapes," *Colloids and Surfaces A: Physicochemical and Engineering Aspects,* vol. 255, no. 1-3, pp. 193-200, 2005.

[26] M. Schmitt and F. Heib, "High-precision drop shape analysis on inclining flat surfaces: introduction and comparison of this special method with commercial contact angle analysis," *The Journal of chemical physics,* vol. 139, no. 13, p. 134201, 2013.

[27] F. Heib and M. Schmitt, "Statistical contact angle analyses with the high-precision drop shape analysis (HPDSA) approach: Basic principles and applications," *Coatings,* vol. 6, no. 4, p. 57, 2016.

[28] B. Bhushan and M. Nosonovsky, "The rose petal effect and the modes of superhydrophobicity," *Philosophical Transactions of the Royal Society of London A: Mathematical, Physical and Engineering Sciences,* vol. 368, no. 1929, pp. 4713-4728, 2010.

[29] Y. I. Frenkel, "On the behavior of liquid drops on a solid surface. 1. The sliding of drops on an inclined surface," *arXiv preprint physics/0503051,* 2005.

[30] R. Ford and C. Furmidge, "Studies at phase interfaces: II. The stabilization of water-in-oil emulsions using oil-soluble emulsifiers," *Journal of Colloid and Interface Science,* vol. 22, no. 4, pp. 331-341, 1966.

[31] S. T. Larsen, N. K. Andersen, E. Søgaard, and R. Taboryski, "Structure irregularity impedes drop roll-off at superhydrophobic surfaces," *Langmuir,* vol. 30, no. 17, pp. 5041-5045, 2014.

[32] D. Brutin, *Droplet wetting and evaporation: from pure to complex fluids*. Academic Press, 2015.
[33] R. N. Wenzel, "Resistance of solid surfaces to wetting by water," *Industrial & Engineering Chemistry,* vol. 28, no. 8, pp. 988-994, 1936.
[34] A. Cassie and S. Baxter, "Wettability of porous surfaces," *Transactions of the Faraday society,* vol. 40, pp. 546-551, 1944.
[35] J. Bico, U. Thiele, and D. Quéré, "Wetting of textured surfaces," *Colloids and Surfaces A: Physicochemical and Engineering Aspects,* vol. 206, no. 1-3, pp. 41-46, 2002.
[36] J. Bico, C. Marzolin, and D. Quéré, "Pearl drops," *EPL (Europhysics Letters),* vol. 47, no. 2, p. 220, 1999.
[37] C. Extrand, "Contact angles and hysteresis on surfaces with chemically heterogeneous islands," *Langmuir,* vol. 19, no. 9, pp. 3793-3796, 2003.
[38] L. Gao and T. J. McCarthy, "How Wenzel and Cassie were wrong," *Langmuir,* vol. 23, no. 7, pp. 3762-3765, 2007.
[39] M. Miwa, A. Nakajima, A. Fujishima, K. Hashimoto, and T. Watanabe, "Effects of the surface roughness on sliding angles of water droplets on superhydrophobic surfaces," *Langmuir,* vol. 16, no. 13, pp. 5754-5760, 2000.
[40] N. Okulova, P. Johansen, L. Christensen, and R. Taboryski, "Effect of Structure Hierarchy for Superhydrophobic Polymer Surfaces Studied by Droplet Evaporation," *Nanomaterials,* vol. 8, no. 10, p. 831, 2018.
[41] L. Feng *et al.*, "Petal effect: a superhydrophobic state with high adhesive force," *Langmuir,* vol. 24, no. 8, pp. 4114-4119, 2008.
[42] S. Wang and L. Jiang, "Definition of superhydrophobic states," *Advanced Materials,* vol. 19, no. 21, pp. 3423-3424, 2007.
[43] L. Gao and T. J. McCarthy, "The “lotus effect” explained: two reasons why two length scales of topography are important," *Langmuir,* vol. 22, no. 7, pp. 2966-2967, 2006.
[44] M. Yu, S. Chen, B. Zhang, D. Qiu, and S. Cui, "Why a lotus-like superhydrophobic surface is self-cleaning? An explanation from surface force measurements and analysis," *Langmuir,* vol. 30, no. 45, pp. 13615-13621, 2014.
[45] S. Pechook *et al.*, "Bioinspired passive anti-biofouling surfaces preventing biofilm formation," *Journal of Materials Chemistry B,* vol. 3, no. 7, pp. 1371-1378, 2015.
[46] W. Barthlott and C. Neinhuis, "Purity of the sacred lotus, or escape from contamination in biological surfaces," *Planta,* vol. 202, no. 1, pp. 1-8, 1997.
[47] D. Quéré, "Non-sticking drops," *Reports on Progress in Physics,* vol. 68, no. 11, p. 2495, 2005.
[48] P. Roach, N. J. Shirtcliffe, and M. I. Newton, "Progess in superhydrophobic surface development," *Soft matter,* vol. 4, no. 2, pp. 224-240, 2008.
[49] X. Zhang, F. Shi, J. Niu, Y. Jiang, and Z. Wang, "Superhydrophobic surfaces: from structural control to functional application," *Journal of Materials Chemistry,* vol. 18, no. 6, pp. 621-633, 2008.
[50] N. A. Patankar, "On the modeling of hydrophobic contact angles on rough surfaces," *Langmuir,* vol. 19, no. 4, pp. 1249-1253, 2003.
[51] N. A. Patankar, "Transition between superhydrophobic states on rough surfaces," *Langmuir,* vol. 20, no. 17, pp. 7097-7102, 2004.
[52] L. Zhu, Y. Xiu, J. Xu, P. A. Tamirisa, D. W. Hess, and C.-P. Wong, "Superhydrophobicity on two-tier rough surfaces fabricated by controlled growth of

aligned carbon nanotube arrays coated with fluorocarbon," *Langmuir*, vol. 21, no. 24, pp. 11208-11212, 2005.

[53] R. Fürstner, W. Barthlott, C. Neinhuis, and P. Walzel, "Wetting and self-cleaning properties of artificial superhydrophobic surfaces," *Langmuir*, vol. 21, no. 3, pp. 956-961, 2005.

[54] K. Koch, B. Bhushan, Y. C. Jung, and W. Barthlott, "Fabrication of artificial Lotus leaves and significance of hierarchical structure for superhydrophobicity and low adhesion," *Soft Matter*, vol. 5, no. 7, pp. 1386-1393, 2009.

[55] M. Toma, G. Loget, and R. M. Corn, "Flexible teflon nanocone array surfaces with tunable superhydrophobicity for self-cleaning and aqueous droplet patterning," *ACS applied materials & interfaces*, vol. 6, no. 14, pp. 11110-11117, 2014.

[56] H. Y. Erbil, A. L. Demirel, Y. Avcı, and O. Mert, "Transformation of a simple plastic into a superhydrophobic surface," *Science*, vol. 299, no. 5611, pp. 1377-1380, 2003.

[57] K. K. Lau *et al.*, "Superhydrophobic carbon nanotube forests," *Nano letters*, vol. 3, no. 12, pp. 1701-1705, 2003.

[58] Y. Lu, S. Sathasivam, J. Song, C. R. Crick, C. J. Carmalt, and I. P. Parkin, "Robust self-cleaning surfaces that function when exposed to either air or oil," *Science*, vol. 347, no. 6226, pp. 1132-1135, 2015.

[59] K. M. Wisdom, J. A. Watson, X. Qu, F. Liu, G. S. Watson, and C.-H. Chen, "Self-cleaning of superhydrophobic surfaces by self-propelled jumping condensate," *Proceedings of the National Academy of Sciences*, p. 201210770, 2013.

[60] J. B. Boreyko and C.-H. Chen, "Self-propelled dropwise condensate on superhydrophobic surfaces," *Physical review letters*, vol. 103, no. 18, p. 184501, 2009.

[61] N. Miljkovic *et al.*, "Jumping-droplet-enhanced condensation on scalable superhydrophobic nanostructured surfaces," *Nano letters*, vol. 13, no. 1, pp. 179-187, 2012.

[62] A. Tuteja *et al.*, "Designing superoleophobic surfaces," *Science*, vol. 318, no. 5856, pp. 1618-1622, 2007.

[63] A. Lafuma and D. Quéré, "Superhydrophobic states," *Nature materials*, vol. 2, no. 7, p. 457, 2003.

[64] S. Shibuichi, T. Yamamoto, T. Onda, and K. Tsujii, "Super water-and oil-repellent surfaces resulting from fractal structure," *Journal of Colloid and Interface Science*, vol. 208, no. 1, pp. 287-294, 1998.

[65] S. R. Coulson, I. Woodward, J. Badyal, S. A. Brewer, and C. Willis, "Super-repellent composite fluoropolymer surfaces," *The Journal of Physical Chemistry B*, vol. 104, no. 37, pp. 8836-8840, 2000.

[66] R. Helbig, J. Nickerl, C. Neinhuis, and C. Werner, "Smart skin patterns protect springtails," *PloS one*, vol. 6, no. 9, p. e25105, 2011.

[67] T. Liu and C.-J. Kim, "Turning a surface superrepellent even to completely wetting liquids," 2014.

[68] H.-J. Butt, C. Semprebon, P. Papadopoulos, D. Vollmer, M. Brinkmann, and M. Ciccotti, "Design principles for superamphiphobic surfaces," *Soft Matter*, vol. 9, no. 2, pp. 418-428, 2013.

[69] B. Zhang and X. Zhang, "Elucidating nonwetting of re-entrant surfaces with impinging droplets," *Langmuir*, vol. 31, no. 34, pp. 9448-9457, 2015.

[70] M. Nosonovsky, "Multiscale roughness and stability of superhydrophobic biomimetic interfaces," *Langmuir,* vol. 23, no. 6, pp. 3157-3161, 2007.
[71] A. Tuteja, W. Choi, J. M. Mabry, G. H. McKinley, and R. E. Cohen, "Robust omniphobic surfaces," *Proceedings of the National Academy of Sciences,* vol. 105, no. 47, pp. 18200-18205, 2008.
[72] X. Chen, J. A. Weibel, and S. V. Garimella, "Water and ethanol droplet wetting transition during evaporation on omniphobic surfaces," *Scientific reports,* vol. 5, p. 17110, 2015.
[73] A. Ahuja *et al.*, "Nanonails: A simple geometrical approach to electrically tunable superlyophobic surfaces," *Langmuir,* vol. 24, no. 1, pp. 9-14, 2008.
[74] F. Schreiber, "Structure and growth of self-assembling monolayers," *Progress in surface science,* vol. 65, no. 5-8, pp. 151-257, 2000.
[75] S. Gan, P. Yang, and W. Yang, "Photoactivation of Alkyl C− H and silanization: A simple and general route to prepare high-density primary amines on inert polymer surfaces for protein immobilization," *Biomacromolecules,* vol. 10, no. 5, pp. 1238-1243, 2009.
[76] E. Bormashenko, R. Grynyov, G. Chaniel, H. Taitelbaum, and Y. Bormashenko, "Robust technique allowing manufacturing superoleophobic surfaces," *Applied Surface Science,* vol. 270, pp. 98-103, 2013.
[77] S. Nagappan and C.-S. Ha, "Superhydrophobic and self-cleaning natural leaf powder/poly (methylhydroxysiloxane) hybrid micro-nanocomposites," *Macromolecular Research,* vol. 22, no. 8, pp. 843-852, 2014.
[78] X. Lu *et al.*, "Front‐End‐of‐Line Integration of Graphene Oxide for Graphene‐Based Electrical Platforms," *Advanced Materials Technologies,* vol. 3, no. 4, p. 1700318, 2018.
[79] X. Deng, L. Mammen, H.-J. Butt, and D. Vollmer, "Candle soot as a template for a transparent robust superamphiphobic coating," *Science,* vol. 335, no. 6064, pp. 67-70, 2012.
[80] X. Deng *et al.*, "Solvent‐Free Synthesis of Microparticles on Superamphiphobic Surfaces," *Angewandte Chemie International Edition,* vol. 52, no. 43, pp. 11286-11289, 2013.
[81] B. Gupta, J. Hilborn, C. Hollenstein, C. Plummer, R. Houriet, and N. Xanthopoulos, "Surface modification of polyester films by RF plasma," *Journal of Applied Polymer Science,* vol. 78, no. 5, pp. 1083-1091, 2000.
[82] G. W. Bates, J. Boyer, J. C. Hegenauer, and P. Saltman, "Facilitation of iron absorption by ferric fructose," *The American journal of clinical nutrition,* vol. 25, no. 10, pp. 983-986, 1972.
[83] R. Wang *et al.*, "Light-induced amphiphilic surfaces," *Nature,* vol. 388, no. 6641, p. 431, 1997.
[84] M. Piispanen and L. Hupa, "Comparison of self-cleaning properties of three titania coatings on float glass," *Applied Surface Science,* vol. 258, no. 3, pp. 1126-1131, 2011.
[85] M. A. M. L. de Jesus, J. T. da Silva Neto, G. Timò, P. R. P. Paiva, M. S. S. Dantas, and A. de Mello Ferreira, "Superhydrophilic self-cleaning surfaces based on TiO 2 and TiO 2/SiO 2 composite films for photovoltaic module cover glass," *Applied Adhesion Science,* vol. 3, no. 1, p. 5, 2015.

[86] B. Kraeutler and A. J. Bard, "Photoelectrosynthesis of ethane from acetate ion at an n-type titanium dioxide electrode. The photo-Kolbe reaction," *Journal of the American Chemical Society,* vol. 99, no. 23, pp. 7729-7731, 1977.

[87] M. R. Hoffmann, S. T. Martin, W. Choi, and D. W. Bahnemann, "Environmental applications of semiconductor photocatalysis," *Chemical reviews,* vol. 95, no. 1, pp. 69-96, 1995.

[88] M. Vautier, C. Guillard, and J.-M. Herrmann, "Photocatalytic degradation of dyes in water: case study of indigo and of indigo carmine," *Journal of Catalysis,* vol. 201, no. 1, pp. 46-59, 2001.

[89] I. Dolamic and T. Bürgi, "Photocatalysis of dicarboxylic acids over TiO2: An in situ ATR-IR study," *Journal of Catalysis,* vol. 248, no. 2, pp. 268-276, 2007.

[90] D. Yang, X. Ni, W. Chen, and Z. Weng, "The observation of photo-Kolbe reaction as a novel pathway to initiate photocatalytic polymerization over oxide semiconductor nanoparticles," *Journal of Photochemistry and Photobiology A: Chemistry,* vol. 195, no. 2-3, pp. 323-329, 2008.

[91] M. Schmitt, "ZnO Nanoparticle Induced Photo‐Kolbe Reaction, Fragment Stabilization and Effect on Photopolymerization Monitored by Raman–UV‐Vis Measurements," *Macromolecular Chemistry and Physics,* vol. 213, no. 18, pp. 1953-1962, 2012.

[92] M. Schmitt, "Synthesis and testing of ZnO nanoparticles for photo-initiation: experimental observation of two different non-migration initiators for bulk polymerization," *Nanoscale,* vol. 7, no. 21, pp. 9532-9544, 2015.

[93] K. Meilert, D. Laub, and J. Kiwi, "Photocatalytic self-cleaning of modified cotton textiles by TiO2 clusters attached by chemical spacers," *Journal of molecular catalysis A: chemical,* vol. 237, no. 1-2, pp. 101-108, 2005.

[94] R. A. Damodar, S.-J. You, and H.-H. Chou, "Study the self cleaning, antibacterial and photocatalytic properties of TiO2 entrapped PVDF membranes," *Journal of hazardous materials,* vol. 172, no. 2-3, pp. 1321-1328, 2009.

[95] M. B. Hugenschmidt, L. Gamble, and C. T. Campbell, "The interaction of H2O with a TiO2 (110) surface," *Surface Science,* vol. 302, no. 3, pp. 329-340, 1994.

[96] T.-S. Wong *et al.*, "Bioinspired self-repairing slippery surfaces with pressure-stable omniphobicity," *Nature,* vol. 477, no. 7365, p. 443, 2011.

[97] H. F. Bohn and W. Federle, "Insect aquaplaning: Nepenthes pitcher plants capture prey with the peristome, a fully wettable water-lubricated anisotropic surface," *Proceedings of the National Academy of Sciences,* vol. 101, no. 39, pp. 14138-14143, 2004.

[98] P. Kim, T.-S. Wong, J. Alvarenga, M. J. Kreder, W. E. Adorno-Martinez, and J. Aizenberg, "Liquid-infused nanostructured surfaces with extreme anti-ice and anti-frost performance," *ACS nano,* vol. 6, no. 8, pp. 6569-6577, 2012.

[99] P. W. Wilson *et al.*, "Inhibition of ice nucleation by slippery liquid-infused porous surfaces (SLIPS)," *Physical Chemistry Chemical Physics,* vol. 15, no. 2, pp. 581-585, 2013.

[100] C. Urata, G. J. Dunderdale, M. W. England, and A. Hozumi, "Self-lubricating organogels (SLUGs) with exceptional syneresis-induced anti-sticking properties against viscous emulsions and ices," *Journal of Materials Chemistry A,* vol. 3, no. 24, pp. 12626-12630, 2015.

[101] P. Irajizad, M. Hasnain, N. Farokhnia, S. M. Sajadi, and H. Ghasemi, "Magnetic slippery extreme icephobic surfaces," *Nature communications,* vol. 7, p. 13395, 2016.

[102] M. S. Khalil-Abad and M. E. Yazdanshenas, "Superhydrophobic antibacterial cotton textiles," *Journal of colloid and interface science,* vol. 351, no. 1, pp. 293-298, 2010.
[103] C. R. Crick, S. Ismail, J. Pratten, and I. P. Parkin, "An investigation into bacterial attachment to an elastomeric superhydrophobic surface prepared via aerosol assisted deposition," *Thin Solid Films,* vol. 519, no. 11, pp. 3722-3727, 2011.
[104] P. Mahalakshmi, S. Vanithakumari, J. Gopal, U. K. Mudali, and B. Raj, "Enhancing corrosion and biofouling resistance through superhydrophobic surface modification," *Current science,* pp. 1328-1336, 2011.
[105] B. J. Privett *et al.*, "Antibacterial fluorinated silica colloid superhydrophobic surfaces," *Langmuir,* vol. 27, no. 15, pp. 9597-9601, 2011.
[106] M. Moreno-Couranjou, R. Mauchauffé, S. Bonot, C. Detrembleur, and P. Choquet, "Anti-biofouling and antibacterial surfaces via a multicomponent coating deposited from an up-scalable atmospheric-pressure plasma-assisted CVD process," *Journal of Materials Chemistry B,* vol. 6, no. 4, pp. 614-623, 2018.
[107] K. Sun *et al.*, "Anti-biofouling superhydrophobic surface fabricated by picosecond laser texturing of stainless steel," *Applied Surface Science,* vol. 436, pp. 263-267, 2018.
[108] G. B. Hwang, K. Page, A. Patir, S. P. Nair, E. Allan, and I. P. Parkin, "The Anti-Biofouling Properties of Superhydrophobic Surfaces are Short-Lived," *ACS nano,* 2018.
[109] A. K. Epstein, T.-S. Wong, R. A. Belisle, E. M. Boggs, and J. Aizenberg, "Liquid-infused structured surfaces with exceptional anti-biofouling performance," *Proceedings of the National Academy of Sciences,* vol. 109, no. 33, pp. 13182-13187, 2012.
[110] J. Yin, M. L. Mei, Q. Li, R. Xia, Z. Zhang, and C. H. Chu, "Self-cleaning and antibiofouling enamel surface by slippery liquid-infused technique," *Scientific reports,* vol. 6, p. 25924, 2016.
[111] D. C. Leslie *et al.*, "A bioinspired omniphobic surface coating on medical devices prevents thrombosis and biofouling," *Nature biotechnology,* vol. 32, no. 11, p. 1134, 2014.
[112] M. Badv, I. H. Jaffer, J. I. Weitz, and T. F. Didar, "An omniphobic lubricant-infused coating produced by chemical vapor deposition of hydrophobic organosilanes attenuates clotting on catheter surfaces," *Scientific reports,* vol. 7, no. 1, p. 11639, 2017.
[113] A. Hosseini *et al.*, "Conductive Electrochemically Active Lubricant‐Infused Nanostructured Surfaces Attenuate Coagulation and Enable Friction‐Less Droplet Manipulation," *Advanced Materials Interfaces,* vol. 5, no. 18, p. 1800617, 2018.
[114] M. Badv, S. M. Imani, J. I. Weitz, and T. F. Didar, "Lubricant-infused surfaces with built-in functional biomolecules exhibit simultaneous repellency and tunable cell adhesion," *ACS nano,* vol. 12, no. 11, pp. 10890-10902, 2018.
[115] Z. Dong *et al.*, "Superoleophobic Slippery Lubricant‐Infused Surfaces: Combining Two Extremes in the Same Surface," *Advanced Materials,* vol. 30, no. 45, p. 1803890, 2018.
[116] H. R. Holmes and K. F. Böhringer, "Transporting droplets through surface anisotropy," *Microsystems & Nanoengineering,* vol. 1, p. 15022, 2015.
[117] M. K. Chaudhury and G. M. Whitesides, "How to make water run uphill," *Science,* vol. 256, no. 5063, pp. 1539-1541, 1992.
[118] D. E. Kataoka and S. M. Troian, "Patterning liquid flow on the microscopic scale," *Nature,* vol. 402, no. 6763, p. 794, 1999.
[119] M. G. Pollack, A. D. Shenderov, and R. Fair, "Electrowetting-based actuation of droplets for integrated microfluidics," *Lab on a Chip,* vol. 2, no. 2, pp. 96-101, 2002.

[120] S. K. Cho, H. Moon, and C.-J. Kim, "Creating, transporting, cutting, and merging liquid droplets by electrowetting-based actuation for digital microfluidic circuits," *Journal of Microelectromechanical systems,* vol. 12, no. 1, pp. 70-80, 2003.
[121] S.-Y. Park, M. A. Teitell, and E. P. Chiou, "Single-sided continuous optoelectrowetting (SCOEW) for droplet manipulation with light patterns," *Lab on a Chip,* vol. 10, no. 13, pp. 1655-1661, 2010.
[122] M. K. Tan, J. R. Friend, and L. Y. Yeo, "Microparticle collection and concentration via a miniature surface acoustic wave device," *Lab on a Chip,* vol. 7, no. 5, pp. 618-625, 2007.
[123] A. Shastry, M. J. Case, and K. F. Böhringer, "Directing droplets using microstructured surfaces," *Langmuir,* vol. 22, no. 14, pp. 6161-6167, 2006.
[124] T. A. Duncombe, J. F. Parsons, and K. F. Böhringer, "Directed drop transport rectified from orthogonal vibrations via a flat wetting barrier ratchet," *Langmuir,* vol. 28, no. 38, pp. 13765-13770, 2012.
[125] E. A. Latip *et al.*, "Protein droplet actuation on superhydrophobic surfaces: a new approach toward anti-biofouling electrowetting systems," *RSC Advances,* vol. 7, no. 78, pp. 49633-49648, 2017.
[126] M. Jönsson-Niedziółka *et al.*, "EWOD driven cleaning of bioparticles on hydrophobic and superhydrophobic surfaces," *Lab on a Chip,* vol. 11, no. 3, pp. 490-496, 2011.
[127] Y. Zhao and S. K. Cho, "Microparticle sampling by electrowetting-actuated droplet sweeping," *Lab on a Chip,* vol. 6, no. 1, pp. 137-144, 2006.
[128] H. Geng and S. K. Cho, "Anti-biofouling droplet manipulation by slippery liquid infused porous surface (SLIPS) integrated with electrowetting and liquid-dielectrophoresis," in *Micro Electro Mechanical Systems (MEMS), 2018 IEEE*, 2018, pp. 261-264: IEEE.
[129] K. Y. Lee, J. Hong, and S. K. Chung, "Smart self-cleaning lens cover for miniature cameras of automobiles," *Sensors and Actuators B: Chemical,* vol. 239, pp. 754-758, 2017.
[130] S. Masuda, M. Washizu, and I. Kawabata, "Movement of blood cells in liquid by nonuniform traveling field," *IEEE transactions on Industry Applications,* vol. 24, no. 2, pp. 217-222, 1988.
[131] R. Sharma, C. A. Wyatt, J. Zhang, C. I. Calle, N. Mardesich, and M. K. Mazumder, "Experimental evaluation and analysis of electrodynamic screen as dust mitigation technology for future Mars missions," *IEEE Transactions on Industry Applications,* vol. 45, no. 2, pp. 591-596, 2009.
[132] A. Biris *et al.*, "Electrodynamic removal of contaminant particles and its applications," in *Industry Applications Conference, 2004. 39th IAS Annual Meeting. Conference Record of the 2004 IEEE*, 2004, vol. 2, pp. 1283-1286: IEEE.
[133] R. Sharma, C. Wyatt, J. Zhang, M. Mazumder, C. Calle, and N. Mardesich, "Performance Analysis of Electrodynamic Self-cleaning Transparent Films for its Applications to Mars and Lunar Missions," in *Industry Applications Conference, 2007. 42nd IAS Annual Meeting. Conference Record of the 2007 IEEE*, 2007, pp. 434-437: IEEE.
[134] M. Mazumder *et al.*, "Characterization of electrodynamic screen performance for dust removal from solar panels and solar hydrogen generators," *IEEE Transactions on industry applications,* vol. 49, no. 4, pp. 1793-1800, 2013.
[135] M. N. Horenstein, M. Mazumder, and R. C. Sumner Jr, "Predicting particle trajectories on an electrodynamic screen–theory and experiment," *Journal of Electrostatics,* vol. 71, no. 3, pp. 185-188, 2013.

[136] B. Guo and W. Javed, "Efficiency of Electrodynamic Dust Shield at Dust Loading Levels Relevant to Solar Energy Applications," *IEEE Journal of Photovoltaics,* vol. 8, no. 1, pp. 196-202, 2018.
[137] B. Guo, W. Javed, C. Pett, C.-Y. Wu, and J. R. Scheffe, "Electrodynamic dust shield performance under simulated operating conditions for solar energy applications," *Solar Energy Materials and Solar Cells,* vol. 185, pp. 80-85, 2018.
[138] K. Autumn *et al.*, "Adhesive force of a single gecko foot-hair," *Nature,* vol. 405, no. 6787, p. 681, 2000.
[139] K. Autumn *et al.*, "Evidence for van der Waals adhesion in gecko setae," *Proceedings of the National Academy of Sciences,* vol. 99, no. 19, pp. 12252-12256, 2002.
[140] A. Y. Stark, N. A. Wucinich, E. L. Paoloni, P. H. Niewiarowski, and A. Dhinojwala, "Self-drying: a gecko's innate ability to remove water from wet toe pads," *Plos One,* vol. 9, no. 7, p. e101885, 2014.
[141] W. R. Hansen and K. Autumn, "Evidence for self-cleaning in gecko setae," *Proceedings of the National Academy of Sciences,* vol. 102, no. 2, pp. 385-389, 2005.
[142] S. Sethi, L. Ge, L. Ci, P. M. Ajayan, and A. Dhinojwala, "Gecko-inspired carbon nanotube-based self-cleaning adhesives," *Nano letters,* vol. 8, no. 3, pp. 822-825, 2008.
[143] J. Lee and R. S. Fearing, "Contact self-cleaning of synthetic gecko adhesive from polymer microfibers," *Langmuir,* vol. 24, no. 19, pp. 10587-10591, 2008.
[144] A. Sayyah, M. N. Horenstein, and M. K. Mazumder, "Energy yield loss caused by dust deposition on photovoltaic panels," *Solar Energy,* vol. 107, pp. 576-604, 2014.
[145] A. Einhorn *et al.*, "Evaluation of Soiling and Potential Mitigation Approaches on Photovoltaic Glass," *IEEE Journal of Photovoltaics,* vol. 9, no. 1, pp. 233-239, 2018.
[146] L. L. Kazmerski *et al.*, "Fundamental studies of adhesion of dust to PV module surfaces: Chemical and physical relationships at the microscale," *IEEE Journal of Photovoltaics,* vol. 6, no. 3, pp. 719-729, 2016.
[147] B. Aïssa, R. J. Isaifan, V. E. Madhavan, and A. A. Abdallah, "Structural and physical properties of the dust particles in Qatar and their influence on the PV panel performance," *Scientific reports,* vol. 6, p. 31467, 2016.
[148] T. A. Duncombe, E. Y. Erdem, A. Shastry, R. Baskaran, and K. F. Böhringer, "Controlling liquid drops with texture ratchets," *Advanced Materials,* vol. 24, no. 12, pp. 1545-1550, 2012.
[149] S. Makohliso, L. Giovangrandi, D. Leonard, H. Mathieu, M. Ilegems, and P. Aebischer, "Application of Teflon-AF® thin films for bio-patterning of neural cell adhesion," *Biosensors and Bioelectronics,* vol. 13, no. 11, pp. 1227-1235, 1998.
[150] C.-C. Cho, R. Wallace, and L. Files-Sesler, "Patterning and etching of amorphous Teflon films," *Journal of electronic materials,* vol. 23, no. 8, pp. 827-830, 1994.
[151] C. P. Tan, B. R. Cipriany, D. M. Lin, and H. G. Craighead, "Nanoscale resolution, multicomponent biomolecular arrays generated by aligned printing with parylene peel-off," *Nano letters,* vol. 10, no. 2, pp. 719-725, 2010.
[152] I. Sanzari, M. Callisti, A. De Grazia, D. J. Evans, T. Polcar, and T. Prodromakis, "Parylene C topographic micropattern as a template for patterning PDMS and Polyacrylamide hydrogel," *Scientific reports,* vol. 7, no. 1, p. 5764, 2017.
[153] Available: https://www.analog.com/media/ru/technical-documentation/application-notes/AN-1057.pdf

[154] H. Zhang, Q. Yan, Q. Xu, C. Xiao, and X. Liang, "A sacrificial layer strategy for photolithography on highly hydrophobic surface and its application for electrowetting devices," *Scientific reports,* vol. 7, no. 1, p. 3983, 2017.
[155] H. R. Holmes, A. E. Gomez, and K. F. Böhringer, "Enabling Droplet Functionality on Anisotropic Ratchet Conveyors," *Micromachines,* vol. 8, no. 12, p. 363, 2017.
[156] M. Assmus, S. Jack, K. A. Weiss, and M. Koehl, "Measurement and simulation of vibrations of PV‐modules induced by dynamic mechanical loads," *Progress in Photovoltaics: Research and Applications,* vol. 19, no. 6, pp. 688-694, 2011.
[157] X. Noblin, A. Buguin, and F. Brochard-Wyart, "Vibrated sessile drops: Transition between pinned and mobile contact line oscillations," *The European Physical Journal E,* vol. 14, no. 4, pp. 395-404, 2004.
[158] J. S. Sharp, D. J. Farmer, and J. Kelly, "Contact angle dependence of the resonant frequency of sessile water droplets," *Langmuir,* vol. 27, no. 15, pp. 9367-9371, 2011.
[159] S. Mettu and M. Chaudhury, "Vibration spectroscopy of a sessile drop and its contact line," *Langmuir,* vol. 28, no. 39, pp. 14100-14106, 2012.
[160] L. D. Landau and E. M. Lifshitz, "Fluid mechanics," p. 245, 1987.
[161] R. H. Temperton, "Resonant vibrations of microlitre liquid drops," University of Nottingham, 2013.
[162] Y. Dong, H. R. Holmes, and K. F. J. L. Böhringer, "Converting vertical vibration of anisotropic ratchet conveyors into horizontal droplet motion," vol. 33, no. 40, pp. 10745-10752, 2017.
[163] H. Georgi, *The physics of waves*. Prentice Hall Englewood Cliffs, NJ, 1993.
[164] G. F. Lang and D. Snyder, "Understanding the physics of electrodynamic shaker performance," *Sound and Vibration,* vol. 35, no. 10, pp. 24-33, 2001.
[165] P. Sharma, M. Flury, and J. Zhou, "Detachment of colloids from a solid surface by a moving air–water interface," *Journal of colloid and interface science,* vol. 326, no. 1, pp. 143-150, 2008.
[166] R. J. Isaifan, D. Johnson, L. Ackermann, B. Figgis, and M. Ayoub, "Evaluation of the adhesion forces between dust particles and photovoltaic module surfaces," *Solar Energy Materials and Solar Cells,* vol. 191, pp. 413-421, 2019.
[167] H. Kim and H.-C. Lim, "Mode pattern of internal flow in a water droplet on a vibrating hydrophobic surface," *The Journal of Physical Chemistry B,* vol. 119, no. 22, pp. 6740-6746, 2015.
[168] Y.-Y. Quan, L.-Z. Zhang, R.-H. Qi, and R.-R. Cai, "Self-cleaning of surfaces: the role of surface wettability and dust types," *Scientific reports,* vol. 6, p. 38239, 2016.
[169] M. J. Jebrail *et al.*, "A digital microfluidic method for dried blood spot analysis," *Lab on a Chip,* vol. 11, no. 19, pp. 3218-3224, 2011.
[170] F. Ahmadi, K. Samlali, P. Q. Vo, and S. C. Shih, "An integrated droplet-digital microfluidic system for on-demand droplet creation, mixing, incubation, and sorting," *Lab on a Chip,* vol. 19, no. 3, pp. 524-535, 2019.
[171] R. Sista *et al.*, "Development of a digital microfluidic platform for point of care testing," *Lab on a Chip,* vol. 8, no. 12, pp. 2091-2104, 2008.
[172] D. Sun and K. F. Böhringer, "Self-Cleaning: From Bio-Inspired Surface Modification to MEMS/Microfluidics System Integration," *Micromachines,* vol. 10, no. 2, p. 101, 2019.

[173] O. Kudina, B. Eral, and F. Mugele, "e-MALDI: an electrowetting-enhanced drop drying method for MALDI mass spectrometry," *Analytical chemistry,* vol. 88, no. 9, pp. 4669-4675, 2016.
[174] C.-P. Chiu *et al.*, "Liquid lenses and driving mechanisms: a review," *Journal of Adhesion Science and Technology,* vol. 26, no. 12-17, pp. 1773-1788, 2012.
[175] J. Heikenfeld *et al.*, "Electrofluidic displays using Young–Laplace transposition of brilliant pigment dispersions," *Nature Photonics,* vol. 3, no. 5, p. 292, 2009.
[176] K. N. Nampoothiri, M. S. Seshasayee, V. Srinivasan, M. Bobji, and P. Sen, "Direct heating of aqueous droplets using high frequency voltage signals on an EWOD platform," *Sensors and Actuators B: Chemical,* vol. 273, pp. 862-872, 2018.
[177] C. Gao *et al.*, "Droplets Manipulated on Photothermal Organogel Surfaces," *Advanced Functional Materials,* vol. 28, no. 35, p. 1803072, 2018.
[178] C. Palma and R. D. Deegan, "Droplet Translation Actuated by Photoelectrowetting," *Langmuir,* vol. 34, no. 10, pp. 3177-3185, 2018.
[179] S. C. Hernandez *et al.*, "Chemical gradients on graphene to drive droplet motion," *Acs Nano,* vol. 7, no. 6, pp. 4746-4755, 2013.
[180] S. Daniel, M. K. Chaudhury, and P.-G. De Gennes, "Vibration-actuated drop motion on surfaces for batch microfluidic processes," *Langmuir,* vol. 21, no. 9, pp. 4240-4248, 2005.
[181] H. Geng, J. Feng, L. M. Stabryla, and S. K. Cho, "Dielectrowetting manipulation for digital microfluidics: Creating, transporting, splitting, and merging of droplets," *Lab on a Chip,* vol. 17, no. 6, pp. 1060-1068, 2017.
[182] K. L. Van Grinsven, A. Ousati Ashtiani, and H. Jiang, "Fabrication and Actuation of an Electrowetting Droplet Array on a Flexible Substrate," *Micromachines,* vol. 8, no. 11, p. 334, 2017.
[183] S.-K. Fan, H. Yang, T.-T. Wang, and W. Hsu, "Asymmetric electrowetting—Moving droplets by a square wave," *Lab on a Chip,* vol. 7, no. 10, pp. 1330-1335, 2007.
[184] J.-H. Kim *et al.*, "Electrowetting on the dielectric (EWOD) properties of teflon-coated electrosprayed silica layers in air and oil media and the influence of electric leakage," *Journal of Materials Chemistry C,* 2018.
[185] N. B. Crane, A. A. Volinsky, P. Mishra, A. Rajgadkar, and M. Khodayari, "Bidirectional electrowetting actuation with voltage polarity dependence," *Applied Physics Letters,* vol. 96, no. 10, p. 104103, 2010.
[186] C. Li and H. Jiang, "Fabrication and characterization of flexible electrowetting on dielectrics (EWOD) microlens," *Micromachines,* vol. 5, no. 3, pp. 432-441, 2014.
[187] D. Chatterjee, B. Hetayothin, A. R. Wheeler, D. J. King, and R. L. Garrell, "Droplet-based microfluidics with nonaqueous solvents and solutions," *Lab on a Chip,* vol. 6, no. 2, pp. 199-206, 2006.
[188] U.-C. Yi and C.-J. Kim, "Characterization of electrowetting actuation on addressable single-side coplanar electrodes," *Journal of Micromechanics and Microengineering,* vol. 16, no. 10, p. 2053, 2006.
[189] J. Sondag-Huethorst and L. Fokkink, "Electrical double layers on thiol-modified polycrystalline gold electrodes," *Journal of Electroanalytical Chemistry,* vol. 367, no. 1-2, pp. 49-57, 1994.
[190] L. G. Fokkink and J. Ralston, "Contact angles on charged substrates," *Colloids and surfaces,* vol. 36, no. 1, pp. 69-76, 1989.

[191] W. J. Welters and L. G. Fokkink, "Fast electrically switchable capillary effects," *Langmuir,* vol. 14, no. 7, pp. 1535-1538, 1998.
[192] J. Berthier and K. A. Brakke, *The physics of microdroplets*. John Wiley & Sons, pp. 298, 2012.
[193] H. Ren, R. B. Fair, M. G. Pollack, and E. J. Shaughnessy, "Dynamics of electro-wetting droplet transport," *Sensors and actuators B: chemical,* vol. 87, no. 1, pp. 201-206, 2002.
[194] J. Lee and C.-J. Kim, "Surface-tension-driven microactuation based on continuous electrowetting," *Journal of Microelectromechanical Systems,* vol. 9, no. 2, pp. 171-180, 2000.
[195] C. W. Nelson, C. M. Lynch, and N. B. Crane, "Continuous electrowetting via electrochemical diodes," *Lab on a Chip,* vol. 11, no. 13, pp. 2149-2152, 2011.
[196] Q. Ni, D. E. Capecci, M. Schlafly, and N. B. Crane, "Robust bidirectional continuous electrowetting based on metal–semiconductor (M–S) diodes," *Microfluidics and Nanofluidics,* vol. 20, no. 8, p. 122, 2016.
[197] Q. Ni, D. E. Capecci, and N. B. Crane, "Open-loop electrowetting actuation with micro-stepping," *Sensors and Actuators A: Physical,* vol. 247, pp. 579-586, 2016.
[198] P. Sen and C.-J. C. Kim, "Capillary spreading dynamics of electrowetted sessile droplets in air," *Langmuir,* vol. 25, no. 8, pp. 4302-4305, 2009.
[199] C.-C. Cho, D. Smith, and J. Anderson, "Low dielectric-constant insulators for electronics applications," *Materials chemistry and physics,* vol. 42, no. 2, pp. 91-95, 1995.
[200] H. Zhang, Q. Yan, Q. Xu, C. Xiao, and X. Liang, "A sacrificial layer strategy for photolithography on highly hydrophobic surface and its application for electrowetting devices," *Scientific reports,* vol. 7, no. 1, pp. 1-7, 2017.
[201] E. Baird, P. Young, and K. Mohseni, "Electrostatic force calculation for an EWOD-actuated droplet," *Microfluidics and Nanofluidics,* vol. 3, no. 6, pp. 635-644, 2007.
[202] M. Abdelgawad, S. L. Freire, H. Yang, and A. R. Wheeler, "All-terrain droplet actuation," *Lab on a Chip,* vol. 8, no. 5, pp. 672-677, 2008.
[203] S. Datta, A. Das, and P. Das, "Uphill movement of sessile droplets by electrostatic actuation," *Langmuir,* vol. 31, no. 37, pp. 10190-10197, 2015.
[204] S.-K. Fan, H. Yang, and W. Hsu, "Droplet-on-a-wristband: Chip-to-chip digital microfluidic interfaces between replaceable and flexible electrowetting modules," *Lab on a Chip,* vol. 11, no. 2, pp. 343-347, 2011.
[205] K. Zhang, Z. Li, M. Maxey, S. Chen, and G. E. Karniadakis, "Self-cleaning of hydrophobic rough surfaces by coalescence-induced wetting transition," *Langmuir,* vol. 35, no. 6, pp. 2431-2442, 2019.
[206] T. Heckenthaler, S. Sadhujan, Y. Morgenstern, P. Natarajan, M. Bashouti, and Y. Kaufman, "Self-Cleaning Mechanism: Why Nanotexture and Hydrophobicity Matter," *Langmuir,* vol. 35, no. 48, pp. 15526-15534, 2019.
[207] N. Miljkovic, D. J. Preston, R. Enright, and E. N. Wang, "Electrostatic charging of jumping droplets," *Nature Communications,* vol. 4, no. 1, pp. 1-9, 2013.
[208] N. Miljkovic *et al.*, "Jumping-droplet-enhanced condensation on scalable superhydrophobic nanostructured surfaces," *Nano letters,* vol. 13, no. 1, pp. 179-187, 2013.
[209] C. Walker, E. Mitridis, T. Kreiner, H. Eghlidi, T. M. Schutzius, and D. Poulikakos, "Transparent metasurfaces counteracting fogging by harnessing sunlight," *Nano letters,* vol. 19, no. 3, pp. 1595-1604, 2019.

[210] H. Bai, L. Wang, J. Ju, R. Sun, Y. Zheng, and L. Jiang, "Efficient water collection on integrative bioinspired surfaces with star‐shaped wettability patterns," *Advanced Materials,* vol. 26, no. 29, pp. 5025-5030, 2014.
[211] D. Song and B. Bhushan, "Optimization of bioinspired triangular patterns for water condensation and transport," *Philosophical Transactions of the Royal Society A,* vol. 377, no. 2150, p. 20190127, 2019.
[212] R. Yan *et al.*, "Enhanced water capture induced with electrowetting-on-dielectric (EWOD) approach," *Applied Physics Letters,* vol. 113, no. 20, p. 204101, 2018.
[213] G. McHale, C. Brown, and N. Sampara, "Voltage-induced spreading and superspreading of liquids," *Nature communications,* vol. 4, no. 1, pp. 1-7, 2013.
[214] G. McHale, C. Brown, M. Newton, G. Wells, and N. Sampara, "Dielectrowetting driven spreading of droplets," *Physical review letters,* vol. 107, no. 18, p. 186101, 2011.
[215] R. Ahmed, D. Hsu, C. Bailey, and T. Jones, "Dispensing picoliter droplets using dielectrophoretic (DEP) microactuation," *Microscale Thermophysical Engineering,* vol. 8, no. 3, pp. 271-283, 2004.
[216] A. M. Edwards, C. V. Brown, M. I. Newton, and G. McHale, "Dielectrowetting: The past, present and future," *Current opinion in colloid & interface science,* vol. 36, pp. 28-36, 2018.
[217] T. B. Jones, J. D. Fowler, Y. S. Chang, and C.-J. Kim, "Frequency-based relationship of electrowetting and dielectrophoretic liquid microactuation," *Langmuir,* vol. 19, no. 18, pp. 7646-7651, 2003.
[218] D. Sun and K. F. Böhringer, "EWOD-aided droplet transport on texture ratchets," *Applied Physics Letters,* vol. 116, no. 9, p. 093702, 2020.
[219] D. Sun and K. F. Böhringer, "Photovoltaic module active self-cleaning surface using anisotropic ratchet conveyors fabricated with parylene-C stencil," in *Journal of Physics: Conference Series*, 2018, vol. 1052, no. 1, p. 012014: IOP Publishing.
[220] D. Sun and K. F. Böhringer, "Self-cleaning surfaces using anisotropic ratchet conveyors," in *2017 19th International Conference on Solid-State Sensors, Actuators and Microsystems (TRANSDUCERS)*, 2017, pp. 1773-1776: IEEE.
[221] T. B. Jones, K.-L. Wang, and D.-J. Yao, "Frequency-dependent electromechanics of aqueous liquids: electrowetting and dielectrophoresis," *Langmuir,* vol. 20, no. 7, pp. 2813-2818, 2004.
[222] C.-H. Chen, S.-L. Tsai, M.-K. Chen, and L.-S. Jang, "Effects of gap height, applied frequency, and fluid conductivity on minimum actuation voltage of electrowetting-on-dielectric and liquid dielectrophoresis," *Sensors and Actuators B: Chemical,* vol. 159, no. 1, pp. 321-327, 2011.
[223] A. Quinn, R. Sedev, and J. Ralston, "Contact angle saturation in electrowetting," *The journal of physical chemistry B,* vol. 109, no. 13, pp. 6268-6275, 2005.
[224] P. Paik, V. K. Pamula, and R. B. Fair, "Rapid droplet mixers for digital microfluidic systems," *Lab on a Chip,* vol. 3, no. 4, pp. 253-259, 2003.
[225] D. Foresti, M. Nabavi, M. Klingauf, A. Ferrari, and D. Poulikakos, "Acoustophoretic contactless transport and handling of matter in air," *Proceedings of the National Academy of Sciences,* vol. 110, no. 31, pp. 12549-12554, 2013.
[226] A. A. Darhuber, J. P. Valentino, S. M. Troian, and S. Wagner, "Thermocapillary actuation of droplets on chemically patterned surfaces by programmable microheater arrays," *Journal of Microelectromechanical Systems,* vol. 12, no. 6, pp. 873-879, 2003.

[227] J. Brzoska, F. Brochard-Wyart, and F. Rondelez, "Motions of droplets on hydrophobic model surfaces induced by thermal gradients," *Langmuir,* vol. 9, no. 8, pp. 2220-2224, 1993.
[228] H. Linke *et al.*, "Self-propelled Leidenfrost droplets," *Physical review letters,* vol. 96, no. 15, p. 154502, 2006.
[229] C. N. Baroud, M. R. de Saint Vincent, and J.-P. Delville, "An optical toolbox for total control of droplet microfluidics," *Lab on a Chip,* vol. 7, no. 8, pp. 1029-1033, 2007.
[230] P.-Y. Chiou, Z. Chang, and M. C. Wu, "Droplet manipulation with light on optoelectrowetting device," *Journal of Microelectromechanical Systems,* vol. 17, no. 1, pp. 133-138, 2008.
[231] A. Takei, K. Matsumoto, and I. Shomoyama, "Capillary motor driven by electrowetting," *Lab on a Chip,* vol. 10, no. 14, pp. 1781-1786, 2010.
[232] T. Jones, "Liquid dielectrophoresis on the microscale," *Journal of Electrostatics,* vol. 51, pp. 290-299, 2001.
[233] J. Shi, D. Ahmed, X. Mao, S.-C. S. Lin, A. Lawit, and T. J. Huang, "Acoustic tweezers: patterning cells and microparticles using standing surface acoustic waves (SSAW)," *Lab on a Chip,* vol. 9, no. 20, pp. 2890-2895, 2009.
[234] Z. Takats, J. M. Wiseman, B. Gologan, and R. G. Cooks, "Mass spectrometry sampling under ambient conditions with desorption electrospray ionization," *Science,* vol. 306, no. 5695, pp. 471-473, 2004.
[235] Y. Li, X. Wang, and R. K. Ernst, "A rapid one‐step method for the characterization of membrane lipid remodeling in Francisella using matrix‐assisted laser desorption ionization time‐of‐flight tandem mass spectrometry," *Rapid Communications in Mass Spectrometry,* vol. 25, no. 18, pp. 2641-2648, 2011.
[236] S. A. Shaffer, M. D. Harvey, D. R. Goodlett, and R. K. Ernst, "Structural heterogeneity and environmentally regulated remodeling of Francisella tularensis subspecies novicida lipid A characterized by tandem mass spectrometry," *Journal of the American Society for Mass Spectrometry,* vol. 18, no. 6, pp. 1080-1092, 2007.
[237] E. C. Yi, H. Lee, R. Aebersold, and D. R. Goodlett, "A microcapillary trap cartridge‐microcapillary high‐performance liquid chromatography electrospray ionization emitter device capable of peptide tandem mass spectrometry at the attomole level on an ion trap mass spectrometer with automated routine operation," *Rapid communications in mass spectrometry,* vol. 17, no. 18, pp. 2093-2098, 2003.
[238] H. Moon, A. R. Wheeler, R. L. Garrell, and J. A. Loo, "An integrated digital microfluidic chip for multiplexed proteomic sample preparation and analysis by MALDI-MS," *Lab on a Chip,* vol. 6, no. 9, pp. 1213-1219, 2006.
[239] T. Nara, M. Takasaki, T. Maeda, T. Higuchi, S. Ando, and S. Tachi, "Surface acoustic wave tactile display," *IEEE Computer Graphics and Applications,* vol. 21, no. 6, pp. 56-63, 2001.
[240] M. Takasaki, T. Nara, S. Tachi, and T. Higuchi, "A tactile display using surface acoustic wave," in *Proceedings 9th IEEE International Workshop on Robot and Human Interactive Communication. IEEE RO-MAN 2000 (Cat. No. 00TH8499)*, 2000, pp. 364-367: IEEE.
[241] D. P. Morgan, "Surface-wave devices for signal processing," *Studies in electrical and electronic engineering,* vol. 19, 1985.

[242] P. Sharma and K. Sreenivas, "Highly sensitive ultraviolet detector based on ZnO/LiNbO 3 hybrid surface acoustic wave filter," *Applied physics letters,* vol. 83, no. 17, pp. 3617-3619, 2003.
[243] R. J. Shilton *et al.*, "Rapid and controllable digital microfluidic heating by surface acoustic waves," *Advanced Functional Materials,* vol. 25, no. 37, pp. 5895-5901, 2015.
[244] T. Franke, A. R. Abate, D. A. Weitz, and A. Wixforth, "Surface acoustic wave (SAW) directed droplet flow in microfluidics for PDMS devices," *Lab on a Chip,* vol. 9, no. 18, pp. 2625-2627, 2009.
[245] J. H. Jung, G. Destgeer, B. Ha, J. Park, and H. J. Sung, "On-demand droplet splitting using surface acoustic waves," *Lab on a Chip,* vol. 16, no. 17, pp. 3235-3243, 2016.
[246] K. M. Kabir, Y. M. Sabri, G. I. Matthews, L. A. Jones, S. J. Ippolito, and S. K. Bhargava, "Selective detection of elemental mercury vapor using a surface acoustic wave (SAW) sensor," *Analyst,* vol. 140, no. 16, pp. 5508-5517, 2015.
[247] S. A. Tadesse and M. Li, "Sub-optical wavelength acoustic wave modulation of integrated photonic resonators at microwave frequencies," *Nature communications,* vol. 5, p. 5402, 2014.
[248] D. Munk *et al.*, "Surface acoustic wave photonic devices in silicon on insulator," *Nature communications,* vol. 10, no. 1, pp. 1-9, 2019.
[249] M. Kurosawa, T. Watanabe, A. Futami, and T. Higuchi, "Surface acoustic wave atomizer," *Sensors and Actuators-A-Physical Sensors,* vol. 50, no. 1, pp. 69-74, 1995.
[250] Y. Huang *et al.*, "Surface acoustic wave nebulization device with dual interdigitated transducers improves SAWN-MS performance," *Journal of Mass Spectrometry,* vol. 51, no. 6, pp. 424-429, 2016.
[251] L. Pintabona, A. Astefanei, G. L. Corthals, and A. C. van Asten, "Utilizing Surface Acoustic Wave Nebulization (SAWN) for the Rapid and Sensitive Ambient Ionization Mass Spectrometric Analysis of Organic Explosives," *Journal of The American Society for Mass Spectrometry,* vol. 30, no. 12, pp. 2655-2669, 2019.
[252] S. R. Heron, R. Wilson, S. A. Shaffer, D. R. Goodlett, and J. M. Cooper, "Surface Acoustic Wave Nebulization of Peptides As a Microfluidic Interface for Mass Spectrometry," *Analytical Chemistry,* vol. 82, no. 10, pp. 3985-3989, 2010/05/15 2010.
[253] J. Ho, M. K. Tan, D. B. Go, L. Y. Yeo, J. R. Friend, and H.-C. Chang, "based microfluidic surface acoustic wave sample delivery and ionization source for rapid and sensitive ambient mass spectrometry," *Analytical chemistry,* vol. 83, no. 9, pp. 3260-3266, 2011.
[254] L. Monkkonen *et al.*, "Screen-printed digital microfluidics combined with surface acoustic wave nebulization for hydrogen-deuterium exchange measurements," *Journal of Chromatography A,* vol. 1439, pp. 161-166, 2016.
[255] J. Ju, Y. Yamagata, H. Ohmori, and T. Higuchi, "Standing wave type surface acoustic wave atomizer," *Sensors and actuators a: physical,* vol. 147, no. 2, pp. 570-575, 2008.
[256] S. H. Yoon *et al.*, "Rapid lipid a structure determination via surface acoustic wave nebulization and hierarchical tandem mass spectrometry algorithm," *Rapid Communications in Mass Spectrometry,* vol. 30, no. 23, pp. 2555-2560, 2016.
[257] Y. Huang *et al.*, "Surface acoustic wave nebulization device with dual interdigitated transducers improves SAWN‐MS performance," *Journal of Mass Spectrometry,* vol. 51, no. 6, pp. 424-429, 2016.

[258] D. Beyssen, L. Le Brizoual, O. Elmazria, and P. Alnot, "Microfluidic device based on surface acoustic wave," *Sensors and Actuators B: Chemical*, vol. 118, no. 1-2, pp. 380-385, 2006.
[259] J. Ju, Y. Yamagata, H. Ohmori, and T. Higuchi, "Standing wave type surface acoustic wave atomizer," (in English), *Sensors and Actuators a-Physical*, vol. 147, no. 2, pp. 570-575, Oct 3 2008.
[260] A. Qi, L. Y. Yeo, and J. R. Friend, "Interfacial destabilization and atomization driven by surface acoustic waves," *Physics of Fluids*, vol. 20, no. 7, p. 074103, 2008.
[261] S. Kooij, A. Astefanei, G. L. Corthals, and D. Bonn, "Size distributions of droplets produced by ultrasonic nebulizers," *Scientific reports*, vol. 9, no. 1, pp. 1-8, 2019.
[262] J. Ransley. *Piezoelectric Materials: Understanding the Standards*. Available: https://www.comsol.com/blogs/piezoelectric-materials-understanding-standards/
[263] S. D. Senturia, *Microsystem design*. Springer Science & Business Media, 2007.
[264] K.-K. Wong, *Properties of lithium niobate* (no. 28). IET, 2002.
[265] S. R. Moheimani and A. J. Fleming, *Piezoelectric transducers for vibration control and damping*. Springer Science & Business Media, 2006.
[266] S. M. Ben Khelil and A. Lozzi, "Nano-SAW devices for RFID and sensing applications: study of lithium niobate behavior," 2015.
[267] S. Datta. (2014). *Piezoelectric Materials: Crystal Orientation and Poling Direction*. Available: https://www.comsol.com/blogs/piezoelectric-materials-crystal-orientation-poling-direction/
[268] J. Ransley, "Piezoelectric Materials: Applying the Standards," 2016.
[269] "Scope," *IEEE Transactions on Sonics and Ultrasonics*, vol. 31, no. 2, pp. i-i, 1984.
[270] *Thickness Shear Mode Quartz Oscillator*. Available: https://www.comsol.com/model/download/648381/models.mems.thickness_shear_quartz_oscillator.pdf
[271] D. Morgan, *Surface acoustic wave filters: With applications to electronic communications and signal processing*. Academic Press, 2010.
[272] A. Fahmy and E. Adler, "Computer-program description. Transformation of tensor constants of anisotropic materials due to rotations of the co-ordinate axes," in *Proceedings of the Institution of Electrical Engineers*, 1975, vol. 122, no. 5, pp. 591-592: IET.

APPENDIX A

Python image processing program to characterize the droplet transportation with the aid of high-speed camera:

```
import os
import numpy as np
import matplotlib.pyplot as plt
from mpl_toolkits.mplot3d import Axes3D
import cv2
import imutils

directory = 'C:\\Users\\dxs53\\OneDrive\\Desktop\\Image
Processing\\DropletVibration\\50Hz200mV'
os.chdir(directory)

centroid_coordinates = []
left_point_coordinates = []
right_point_coordinates = []
left_point_coordinates_1 = [] #store the upper 5 pixel line for tangential estimation
right_point_coordinates_1 = []
left_angle_array = [] #store the left and right contact angle
right_angle_array = []

start_image = 1 #start image number
stop_image = 250 #stop image number
num_image = stop_image-start_image+1

for i in range(start_image,stop_image,1):
    if i<10:
        image=cv2.imread('Test00000'+str(i)+'.jpg')
    elif i>=10 and i<100:
        image = cv2.imread('Test0000' + str(i) + '.jpg')
    elif i>100 and i<1000:
        image = cv2.imread('Test000' + str(i) + '.jpg')
    print ('image number:',i)
    ##########resize image#############
    #print('The size of the image is:', image.shape)  # image.shape[0] = height
(row), image.shape[1] = width (col)
    scale_factor = 70
    width = int(scale_factor * image.shape[1] / 100)
    height = int(scale_factor * image.shape[0] / 100)
    dim = (width, height)
    image_resize = cv2.resize(image, dim, interpolation=cv2.INTER_AREA)
    #print(print('The size of the resized image is:', image_resize.shape))

    ######convert to gray image and blur ######
    image_gray = cv2.cvtColor(image_resize, cv2.COLOR_BGR2GRAY)
    image_blur = cv2.GaussianBlur(image_gray, (5, 5), 0)
    image_thresh = cv2.threshold(image_blur, 60, 255, cv2.THRESH_BINARY)[1]
    image_fill = image_thresh.copy()
    cv2.imshow('thresh_B_W',image_resize) #use color image to determine the substrate
    #cv2.imshow('thresh_B_W', image_thresh)

    #####remove the bottom black part of the image for contour process##############
```

```
    for row in range(0, image_thresh.shape[0] - 1, 1):
        if image_thresh[row, image_thresh.shape[1] - 1] == 0:
            break
    image_thresh[row - 10:image_thresh.shape[0], :] = 255
    col_seed = 0  # record the seed point row and col position/
    row_seed = 0

    col_middle = 0

    image_edge_rough = cv2.Canny(image_thresh, 100, 200)
    indices = np.where(image_edge_rough != [0])
    coordinates = np.dstack((indices[0], indices[1]))
    # cv2.imshow('edge_rough',image_edge_rough)
    # print ((coordinates[0].shape))
    # print (type(indices[1]))
    # print (np.amax(indices[1]))
    # print (np.amin(indices[1]))
    col_middle = int((np.amax(indices[1]) + np.amin(indices[1])) / 2)

    # find the transition from black to white
    for row in range(1, image_thresh.shape[0] - 1, 1):
        if image_fill[row, col_middle] == 255 and image_fill[row - 1, col_middle] ==
0:
            col_seed = col_middle
            row_seed = row
            break

    # print (row_seed)
    # print (col_seed)
    cv2.floodFill(image_fill, None, (col_seed, row_seed), 0)
    #cv2.imshow('fill', image_fill)

    #######image cut by manually select the droplet contact location###########
    subx = 0  # define the x y position of the substrate by clicking on the image
    suby = 0

    def click_event(event, x, y, flags, param):  # x is the col (width) and y is the
row (height)
        if event == cv2.EVENT_LBUTTONDBLCLK:
            #print('the coordinate of the left double click is', x, 'and ', y)
            image_fill[y:, :] = 255
            cv2.imshow('fill', cv2.bitwise_not(image_fill))
            ############ find contours in the processed
image##############################
            cnts = cv2.findContours(cv2.bitwise_not(image_fill), cv2.RETR_EXTERNAL,
                                    cv2.CHAIN_APPROX_NONE)  # contour requires white
regions in black background
            cnts = imutils.grab_contours(cnts)
            # print (cnts)
            ############ find centroid value in teh processed
image###################################
            M = cv2.moments(cnts[0])
            cX = int(M["m10"] / M["m00"])
            cY = int(M["m01"] / M["m00"])
            centroid_coordinates.append([cX,cY]) #cX is the col (width), cY is the
```

```
row (height)

            cv2.drawContours(image_resize, [cnts[0]], -1, (0, 255, 0), 2)
            cv2.circle(image_resize, (cX, cY), 7, (255, 255, 255), -1)
            cv2.putText(image_resize, "center", (cX - 20, cY - 20),
cv2.FONT_HERSHEY_SIMPLEX, 0.5, (255, 255, 255), 2)

            cv2.imshow("image_centroid", image_resize)
            ############ find left and right edge point in the
image#############################
            contour_row_array = []
            subs_row_array = []
            subs_col_array = []
            for i in cnts[0]:
                contour_row_array.append(i[0][1])
            #print (type(contour_row_array))
            max_row = max(contour_row_array)
            max_indicies=[index for index,value in enumerate(contour_row_array) if
value == max_row]
            #print (max_row)
            #print (max_indicies)
            for i in max_indicies:
                subs_row_array.append(cnts[0][i][0][1])
                subs_col_array.append(cnts[0][i][0][0])
            #print (subs_col_array)
            left_index = subs_col_array.index(min(subs_col_array))
            right_index = subs_col_array.index(max(subs_col_array))
            #print (left_index)
            left_col = subs_col_array[left_index]
            left_row = subs_row_array[left_index]
            right_col = subs_col_array[right_index]
            right_row = subs_row_array[right_index]

            left_point_coordinates.append([left_col, left_row])  # left_col is the
col (width), left_row is the row (height)
            right_point_coordinates.append([right_col, right_row])  # right_col is
the col (width), right_row is the row (height)

            cv2.circle(image_resize, (left_col, left_row), 7, (255, 255, 255), -1)
            cv2.circle(image_resize, (right_col, right_row), 7, (255, 255, 255), -1)
            cv2.imshow("image_centroid", image_resize)

            ############ find left and right edge angle in the
image#############################
            contour_row_array = []
            subs_row_array_1 =[]
            subs_col_array_1 = []
            subs_left_angle = []
            subs_right_angle = []
            for i in cnts[0]:
                contour_row_array.append(i[0][1])
            # print (type(contour_row_array))
            max_row = max(contour_row_array)
            max_indicies_1 = [index for index, value in enumerate(contour_row_array)
if value == max_row-10] #find point at upper 5 pixel to approximate tangent line
```

```
            for i in max_indicies_1:
                subs_row_array_1.append(cnts[0][i][0][1])
                subs_col_array_1.append(cnts[0][i][0][0])
            # print (subs_col_array)
            left_index_1 = subs_col_array_1.index(min(subs_col_array_1))
            right_index_1 = subs_col_array_1.index(max(subs_col_array_1))
            # print (left_index)
            left_col_1 = subs_col_array_1[left_index_1]
            left_row_1 = subs_row_array_1[left_index_1]
            right_col_1 = subs_col_array_1[right_index_1]
            right_row_1 = subs_row_array_1[right_index_1]

            vleft_1 = np.array([right_col-left_col,right_row-left_row])
            vleft_2 = np.array([left_col_1-left_col,left_row_1-left_row])
            vright_1 = np.array([left_col-right_col,left_row-right_row])
            vright_2 = np.array([right_col_1-right_col,right_row_1-right_row])

           # print (vleft_1,' ',vleft_2,' ',vright_1,' ',vright_2)

            left_angle =
np.math.atan2(np.linalg.det([vleft_1,vleft_2]),np.dot(vleft_1,vleft_2))
            left_angle_array.append(abs(np.degrees(left_angle)))
            right_angle = np.math.atan2(np.linalg.det([vright_1, vright_2]),
np.dot(vright_1, vright_2))
            right_angle_array.append(abs(np.degrees(right_angle)))
            #print (abs(np.degrees(left_angle)),' ',abs(np.degrees(right_angle)))

            left_point_coordinates_1.append(
                [left_col_1, left_row_1])  # left_col is the col (width), left_row is
the row (height)
            right_point_coordinates_1.append(
                [right_col_1, right_row_1])  # right_col is the col (width),
right_row is the row (height)

            cv2.circle(image_resize, (left_col_1, left_row_1), 7, (255, 255, 255), -
1)
            cv2.circle(image_resize, (right_col_1, right_row_1), 7, (255, 255, 255),
-1)
            cv2.imshow("image_centroid", image_resize)

            #cv2.waitKey(0)
            cv2.destroyAllWindows()

    cv2.setMouseCallback('thresh_B_W', click_event)
    cv2.waitKey(0)

print (centroid_coordinates)
#print (left_point_coordinates)
#print (right_point_coordinates)
print (right_angle_array)
#print (left_angle_array)

#store the data and make plots
centroid_coordinates_x = []
```

```
centroid_coordinates_y = []
left_point_coordinates_x = []
left_point_coordinates_y = []
right_point_coordinates_x =[]
right_point_coordinates_y=[]
substrate_position = []

#seperate the x(col) and y(row) value for storage
for i in centroid_coordinates:
    centroid_coordinates_x.append(i[0])
    centroid_coordinates_y.append(i[1])
for i in left_point_coordinates:
    left_point_coordinates_x.append(i[0])
    left_point_coordinates_y.append(i[1])
    substrate_position.append(i[1])
for i in right_point_coordinates:
    right_point_coordinates_x.append(i[0])
    right_point_coordinates_y.append(i[1])
#save all the data in txt for further analysis
outputname = 'results.csv'
myfile = open(outputname,'w')
myfile.write('centroid_coordinates_x,'+str(centroid_coordinates_x)+'\n')
myfile.write('centroid_coordinates_y,'+str(centroid_coordinates_y)+'\n')

myfile.write('left_coordinates_x,'+str(left_point_coordinates_x)+'\n')
myfile.write('left_coordinates_y,'+str(left_point_coordinates_y)+'\n')

myfile.write('right_coordinates_x,'+str(right_point_coordinates_x)+'\n')
myfile.write('right_coordinates_y,'+str(right_point_coordinates_y)+'\n')

myfile.write('left_angle,'+str(left_angle_array)+'\n')
myfile.write('right_angle,'+str(right_angle_array)+'\n')

myfile.close()

#make plots
time = range(1,num_image,1)
fig,[[ax1,ax2],[ax3,ax4]] = plt.subplots(nrows=2,ncols=2)
#plot position change vs. time
ax1.plot(time,left_point_coordinates_x,'r-',label = 'left')
ax1.plot(time,right_point_coordinates_x,'b-',label='right')
ax1.plot(time,centroid_coordinates_x,'g-',label='centroid')
ax1.set_title('position change vs. time')
ax1.set_xlabel('time (ms)')
ax1.set_ylabel('position (pixel)')
ax1.legend()

#plot substrate position
ax2.plot(time,substrate_position,'r-')
ax2.set_xlabel('time (ms)')
ax2.set_ylabel('substrate position (pixel)')

#plot angle vs time
ax3.plot(time,left_angle_array,'r-')
ax3.plot(time,right_angle_array,'b-')
```

```
ax3.set_title('angle vs time')
ax3.set_xlabel ('time (ms)')
ax3.set_ylabel ('angle (deg)')

#plot centroid position trace
ax4.plot(centroid_coordinates_x,centroid_coordinates_y,'r-')
ax4.set_title('centroid position on the image')
#ax4.set_xlim(0,image_resize.shape[0])
#ax4.set_ylim(0,image_resize.shape[1])

plt.tight_layout()
plt.show()
```

APPENDIX B

Due to the ARC design, the leading edge will pin along a hydrophobic rung while advancing ($\theta_{b,adv} = \theta_{phob,adv}$) and along a hydrophilic rung while receding ($\theta_{b,rec} = \theta_{phil,rec}$). Combining equation (2-2) to (2-5), the force asymmetry yields the following results:

$$F_{asym,adv} = F_{lead,adv} + F_{trail,adv} = d\gamma_{LG}\Big(\big(\chi_{lead,phob} + \chi_{trail,phob}\big)\cos\theta_{phob,adv} + \big(\chi_{lead,phil} + \chi_{trail,phil}\big)\cos\theta_{phil,adv} + \big(\chi_{lead,b} + \chi_{trail,b}\big)\cos\theta_{b,adv}\Big) = d\gamma_{LG}\Big(\big(\chi_{lead,phob} + \chi_{trail,phob}\big)\cos\theta_{phob,adv} + \big(1 - \chi_{lead,phob} - \chi_{lead,b} - 1 - \chi_{trail,phob} - \chi_{trail,b}\big)\cos\theta_{phil,adv} + \big(\chi_{lead,b} + \chi_{trail,b}\big)\cos\theta_{b,adv}\Big) = d\gamma_{LG}\big(\chi_{lead,phob} + \chi_{trail,phob}\big)\big(\cos\theta_{phob,adv} - \cos\theta_{phil,adv}\big) + \big(\chi_{lead,b} + \chi_{trail,b}\big)\big(\cos\theta_{b,adv} - \cos\theta_{phil,adv}\big) = d\gamma_{LG}\big(\chi_{lead,phob} + \chi_{trail,phob}\big)\big(\cos\theta_{phob,adv} - \cos\theta_{phil,adv}\big) + \big(\chi_{lead,b} + \chi_{trail,b}\big)\big(\cos\theta_{phob,adv} - \cos\theta_{phil,adv}\big) = d\gamma_{LG}\big(\chi_{lead,phob} + \chi_{trail,phob} + \chi_{lead,b} + \chi_{trail,b}\big)\big(\cos\theta_{phob,adv} - \cos\theta_{phil,adv}\big) = d\gamma_{LG}\big(1 - \chi_{lead,phil} - 1 - \chi_{trail,phil}\big)\big(\cos\theta_{phob,adv} - \cos\theta_{phil,adv}\big) = d\gamma_{LG}\big(\chi_{lead,phil} + \chi_{trail,phil}\big)\big(\cos\theta_{phil,adv} - \cos\theta_{phob,adv}\big) \approx d\gamma_{LG}\chi_{trail,phil}\big(\cos\theta_{phil,adv} - \cos\theta_{phob,adv}\big)$$

The factors d, γ_{LG}, and $\big(\cos\theta_{phil,adv} - \cos\theta_{phob,adv}\big)$ are positive, while $\chi_{trail,phil}$ is negative. To minimize the backwards force while the droplet expands and the contact line advances, the trailing edge should make as little contact with hydrophilic material as possible.

$$F_{asym,rec} = F_{lead,rec} + F_{trail,rec} = d\gamma_{LG}\Big(\big(\chi_{lead,phob} + \chi_{trail,phob}\big)\cos\theta_{phob,rec} + \big(\chi_{lead,phil} + \chi_{trail,phil}\big)\cos\theta_{phil,rec} + \big(\chi_{lead,b} + \chi_{trail,b}\big)\cos\theta_{b,rec}\Big) = d\gamma_{LG}\Big(\big(\chi_{lead,phob} + \chi_{trail,phob}\big)\cos\theta_{phob,rec} + \big(1 - \chi_{lead,phob} - \chi_{lead,b} - 1 - \chi_{trail,phob} -$$

$\chi_{trail,phob}\big)\cos\theta_{phil,rec} + \big(\chi_{lead,b} + \chi_{trail,b}\big)\cos\theta_{b,rec}\Big) = d\gamma_{LG}\Big(\big(\chi_{lead,phob} + \chi_{trail,phob}\big)\big(\cos\theta_{phob,rec} - \cos\theta_{phil,rec}\big) + \big(\chi_{lead,b} + \chi_{trail,b}\big)\big(\cos\theta_{b,rec} - \cos\theta_{phil,rec}\big)\Big) = d\gamma_{LG}\Big(\big(\chi_{lead,phob} + \chi_{trail,phob}\big)\big(\cos\theta_{phob,rec} - \cos\theta_{phil,rec}\big) + \big(\chi_{lead,b} + \chi_{trail,b}\big)\big(\cos\theta_{phil,rec} - \cos\theta_{phil,rec}\big)\Big) = d\gamma_{LG}\big(\chi_{lead,phob} + \chi_{trail,phob}\big)\big(\cos\theta_{phob,rec} - \cos\theta_{phil,rec}\big) \approx -d\gamma_{LG}\chi_{trail,phob}\big(\cos\theta_{phil,rec} - \cos\theta_{phob,rec}\big)$

The factors d, γ_{LG}, and $\big(\cos\theta_{phil,rec} - \cos\theta_{phob,rec}\big)$ are positive, while $\chi_{trail,phob}$ is negative. To maximize the forward force while the droplet contracts and the contact line recedes, the trailing edge should make as much contact with hydrophobic material as possible.

Finally, force anisotropy can be calculated as follows:

$F_{an} = F_{asym,adv} + F_{asym,rec} = d\gamma_{LG}\Big(\big(\chi_{lead,phil} + \chi_{trail,phil}\big)\big(\cos\theta_{phil,adv} - \cos\theta_{phob,adv}\big) - \big(\chi_{lead,phob} + \chi_{trail,phob}\big)\big(\cos\theta_{phil,rec} - \cos\theta_{phob,rec}\big)\Big) \approx d\gamma_{LG}\Big(\chi_{trail,phil}\big(\cos\theta_{phil,adv} - \cos\theta_{phob,adv}\big) - \chi_{trail,phob}\big(\cos\theta_{phil,rec} - \cos\theta_{phob,rec}\big)\Big)$

If there is no contact angle hysteresis then $F_{an} = d\gamma_{LG}\big(\chi_{trail,phil} - \chi_{trail,phob}\big)\big(\cos\theta_{phil} - \cos\theta_{phob}\big)$. As stated above, to maximize the forward force $\chi_{trail,phil}$ should be as small as possible and $\chi_{trail,phob}$ should be as large as possible. Besides, the forward force increases with a larger difference between the hydrophilic and hydrophobic contact angles.

In practice, this means that the hydrophilic rungs should be as thin as possible, and they should have a curvature that fits the leading edge of the droplet. The two materials should be selected with highly hydrophobic and hydrophilic properties, respectively.

VITA

Di Sun is a Ph.D. candidate at the Electrical and Computer Engineering department and Institute for Nano-Engineered Systems at the University of Washington. He received his B. Eng. degree in the Department of Electrical Engineering and Automation from the Xi'an Jiaotong University, Xi'an, Shaanxi, China in 2011. He received his Master of Science degree from the Department of Electrical Engineering and Computer Science at Case Western Reserve University, Cleveland, OH, the USA in 2014. He has been working on his Ph.D. degree at Prof. Karl F. Böhringer's MEMS Lab in the Department of Electrical and Computer Engineering at the University of Washington, Seattle, WA, the USA since 2014. He has research experience in MEMS/microfluidics for self-cleaning surfaces and lab-on-chip applications, implantable MEMS packaging, and soft electronics for human-computer interactions.

He had multiple internship experiences including Failure Analysis Engineer at Pixtronix (Andover, MA), Process Engineer at Lam Research (Tualatin, OR), Process Engineer at Fluke (Everett, WA), Research Engineer at Microsoft (Redmond, WA) and Process Integration Engineer at OmniVision (Santa Clara, CA). He will be joining Microsoft's HoloLens Group (Redmond, WA) as an Optical Engineer.

Mr. Sun serves as the student fellow for the Clean Energy Institute (CEI) at the University of Washington. He also serves as the student Torrance Tech Due Diligence Analyst for E8 Angels (Seattle, WA).